



Australia's National  
Science Agency

# Large Signal Stability Enhancement in IBR-Dominated Grids

## Topic 1 – Inverter Design – Stage 4

Ms. Hansi Wijayalath  
Dr. Mohammad Hasan Ravanji  
Mr. Huy Duong  
Dr. Elnaz Firouzmand  
Dr. Mehdi Ghazavi Dozein  
Dr. David J. Hill  
Dr. Behrooz Bahrani

20 May 2025

Commonwealth Scientific and Industrial Research Organisation



**MONASH**  
University

## **Copyright**

© Commonwealth Scientific and Industrial Research Organisation 20XX. To the extent permitted by law, all rights are reserved and no part of this publication covered by copyright may be reproduced or copied in any form or by any means except with the written permission of CSIRO.

## **Important disclaimer**

CSIRO advises that the information contained in this publication comprises general statements based on scientific research. The reader is advised and needs to be aware that such information may be incomplete or unable to be used in any specific situation. No reliance or actions must therefore be made on that information without seeking prior expert professional, scientific and technical advice. To the extent permitted by law, CSIRO (including its employees and consultants) excludes all liability to any person for any consequences, including but not limited to all losses, damages, costs, expenses and any other compensation, arising directly or indirectly from using this publication (in part or in whole) and any information or material contained in it.

CSIRO is committed to providing web accessible content wherever possible. If you are having difficulties with accessing this document please contact [csiro.au/contact](https://www.csiro.au/contact).

# Contents

<b>Executive Summary</b>	<b>9</b>
<b>1 Introduction</b>	<b>11</b>
1.1. Background and Research Objectives	11
1.1.1. Building on Stage 3: Advancing Stability Assessments and Tools in Stage 4	12
1.2. Research Relevance to Australia	12
<b>2. Research Completed</b>	<b>14</b>
2.1. Task 1: Enhancing the Large-Signal Stability Analysis Tool	15
2.1.1. Methodology	15
2.1.2. Investigation of the West Murray Zone	19
2.1.3. Critical Learnings and Insights	24
2.2. Task 2: Sensitivity Analysis of GFMI Stability with Respect to Parameter Variation and Fault Profile	25
2.2.1. Comprehensive Literature Review on Large Signal Stability Analysis and Critical Clearing Time Calculation Methods	25
2.2.2. Impact Assessment of Inverter Parameters on Stability	31
2.2.3. Development of A Novel CCT Calculation Methodology	35
2.2.4. Impact of Prioritised Current Limiters on the Transient Stability	46
2.2.5. Critical Learnings and Insights	52
2.3. Task 3: Large Signal Stability Analysis of Multi IBR System	53
2.3.1. Expand the Developed Large-Signal Stability Analysis to Include Systems with Multiple IBRs	53
2.3.2. Use the Developed Method As a Tool and Calculate the CCT of the System	55
2.3.3. Effectiveness Evaluation of the Proposed Methodology	57
2.3.4. Critical Learnings and Insights	60
2.4. Task 4: Development of Tuning and Design Guidelines for IBRs	61
2.4.1. Development of Practical Tuning and Design Guidelines for Grid-forming IBRs	61
2.4.2. AEMO Guidance on Grid-Forming BESS Integration in the NEM	61
2.4.3. Specific Requirements for GFM BESS According to NER Schedule 5.2	61
2.4.4. UNIFI Consortium Specific Requirements for GFM Resources (Ver. 2)	63
2.4.5. Design and Tuning Guidelines for GFM BESS	64
2.4.6. Developed PSCAD Simulation File	71
2.4.7. Critical Learnings and Insights	72
<b>3. Conclusions</b>	<b>73</b>
<b>4. Recommendation Research Priorities</b>	<b>74</b>
<b>Appendix A</b>	<b>76</b>
Parameters Used for the 3-Cluster Model	76
<b>Appendix B</b>	<b>77</b>
Parameters Used for the PSCAD Models	77
CCT and CCA for the Tested Control Parameters of GFM	77
<b>Appendix C</b>	<b>80</b>

Parameters Used for the 5-Bus System .....	80
<b>Appendix D .....</b>	<b>81</b>
User Guide for Running the Developed Tool with Excel-Based Input .....	81
Tool Structure .....	81
Data Preparation in Excel File.....	82
Running the Code .....	86
Interpreting the Results.....	86
Final Notes Regarding Modifications .....	87
Supporting Multiple Networks .....	88
<b>Appendix E.....</b>	<b>89</b>
Voltage Controller Tuning Methodology .....	89
<b>Appendix F.....</b>	<b>92</b>
PSCAD Simulation File for Implementation of Tuning Guidelines .....	92
Simulation Setup .....	92
General Description of The Model .....	92
Model at Its Highest Level .....	92
Inside the BATTERY Model .....	95
<b>Shortened Forms.....</b>	<b>99</b>
<b>References .....</b>	<b>101</b>

## Figures

Figure 1: Generalised representation of a multi-cluster multi-IBR network.....	15
Figure 2: Network diagram of the 3-cluster 7-IBR mesh network .....	18
Figure 3: WMZ and system strength levels [3],[4] .....	19
Figure 4: WMZ with new registered IBR (Green) [5] .....	22
Figure 5: Simplified diagram of a GFMI .....	25
Figure 6: Power-angle curve.....	25
Figure 7: Power-angle curve of a stable case .....	26
Figure 8: Power-angle curve of an unstable case.....	26
Figure 9: Phase portrait of the droop-controlled GFMI [8] .....	27
Figure 10: Phase portrait of the synchronous machine-based controlled GFMI [9] .....	27
Figure 11: Post-fault condition within the DOA -Stable case .....	28
Figure 12: Post-fault condition outside the DOA -Unstable case .....	29
Figure 13: Single-line diagram of a three-phase grid-connected inverter with a grid-forming control.....	31
Figure 14: Performance of the GFMI under three-phase fault at the grid: (Top) SCR=2, (Bottom) SCR=4. (a), (d) PCC active power. (b), (e) Internal frequency signal of the GFMI. (c), (f) Power angle of the GFMI (relative to the infinite bus) .....	32
Figure 15: Time-domain results for three-phase fault up to CCT of each controller for base case (a), (b), (c) frequencies. (d), (e), (f) power angle.....	34
Figure 16: Computer program flow chart for CCT calculation .....	36
Figure 17: Region of attraction with stable case: VSG .....	37
Figure 18: Phase portrait dynamic of stable case: VSG.....	37
Figure 19: Region of attraction with unstable case: VSG .....	38
Figure 20: Phase portrait of the dynamics of the unstable case: VSG .....	38
Figure 21: Energy function value variation during the fault: VSG .....	38
Figure 22: Time domain results for the VSG with a three-phase fault at the grid .....	39
Figure 23: Region of attraction variation with inertia coefficient .....	40
Figure 24: Region of attraction variation with damping coefficient: VSG.....	41
Figure 25: Region of attraction variation with SCR .....	42
Figure 26: Phase portrait dynamics of the stable case: droop.....	43
Figure 27: Region of attraction with the stable case: droop.....	43
Figure 28: Time domain results for the droop with a three-phase fault at the grid .....	44
Figure 29: Region of attraction variation with damping coefficient: droop .....	45
Figure 30: The region of each operation mode: normal mode and current-limited mode .....	47
Figure 31: The region of each operation mode: normal mode and current-limited mode .....	49
Figure 32: The estimated ROA is shown by the red closed curve, which provides the estimated CCT of 0.52s .....	49
Figure 33: The exact CCT from PSCAD is 0.56s .....	49
Figure 34: The nonlinear relationship between $I_m$ and CCT .....	51
Figure 35: n-1 inverter system with slack bus .....	54

Figure 36: Five-bus system with three inverters .....	56
Figure 37: Energy function value variation during the fault.....	57
Figure 38: General block diagram of the control system for a GFM BESS .....	65
Apx Figure D. 1: The organisation of the project folder .....	81
Apx Figure D. 2: Sample of “Config” sheet .....	83
Apx Figure D. 3: Sample of “GFM_IBRs” sheet.....	83
Apx Figure D. 4: Sample of “GFL_IBRs” sheet .....	84
Apx Figure D. 5: Sample of “Network” sheet .....	84
Apx Figure D. 6: Sample of “Zc” sheet.....	85
Apx Figure D. 7: Sample of “Initial” sheet .....	85
Apx Figure D. 8: Sample of “V_ranges” sheet .....	86
Apx Figure F. 1: SMIB system featuring a BESS connected to the grid through an RL transmission line.....	93
Apx Figure F. 2: The grid SCR and X/R ratio can be adjusted using the corresponding sliders. Additionally, the grid voltage, frequency, and phase angle can be modified in real time during the simulation using their respective sliders.....	93
Apx Figure F. 3: Various faults can be applied using the corresponding slider, and the fault initiation and clearing times can also be set here .....	93
Apx Figure F. 4: The user can set BESS commands using these sliders.....	94
Apx Figure F. 5: Dialogue boxes for BESS parameter settings.....	95
Apx Figure F. 6: Inside the BESS block .....	95
Apx Figure F. 7: Internal circuit of the BATTERY block .....	96
Apx Figure F. 8: Internal architecture of the Power Plant Controller.....	97
Apx Figure F. 9: Internal architecture of the Unit Controller .....	97
Apx Figure F. 10: Internal architecture of the GSC block .....	98

## Tables

Table 1: Progress against research roadmap .....	11
Table 2: Comparison of transient stability margins obtained from the existing and updated tools under varied system parameters .....	18
Table 3: Comparison of transient stability margins obtained from PSCAD and Tool.....	20
Table 4: Comparison of stability margins for different slack bus locations and network arrangements .....	21
Table 5: Stability margins for different network arrangements with registered IBR.....	23
Table 6: Stability margins for different RPC gains .....	23
Table 7: CCT and time to reach SEP variation with the inertia coefficient.....	41
Table 8: Comparison of CCT values obtained from time domain simulation and the developed method for different inertia coefficients.....	42
Table 9: CCT and time to reach SEP variation with damping coefficient: VSG.....	42
Table 10: CCT and time to reach SEP variation with SCR .....	43
Table 11: Summary of key findings of VSG.....	43
Table 12: Comparison of CCT values obtained from time domain simulation and the developed method for different damping coefficients .....	46
Table 13: Comparison of CCT values when changing the inertia constant in GFMI with q-PCL and d-PCL .....	51
Table 14: Comparison of CCT values when changing the damping factor in GFMI with q-PCL and d-PCL .....	51
Table 15: Comparison of CCT values when changing the power reference in GFMI with q-PCL and d-PCL.....	51
Table 16: CCT of GFMI without and with PCL in a low-SCR grid ( $P^* = 0.8$ pu) .....	52
Table 17: CCT of GFMI without and with PCL in a high-SCR grid ( $P^* = 0.8$ pu) .....	53
Table 18: SEP and UEP angle of each inverter reference to the 4th inverter .....	57
Table 19: Comparison of CCT for different network arrangements.....	58
Table 20: CCT variation with inertia coefficient of GFMI 1 .....	59
Table 21: CCT variation with Pref of GFMI 1 .....	59
Table 22: CCT variation with line impedance .....	60
Table 23: Impact of VSG-based GFM parameters on transient and small-signal stability .....	71
Table 24: Impact of Droop-based GFM parameters on transient and small-signal stability .....	72
Apx Table A. 1: System and control parameters for the 3- cluster network.....	77
Apx Table B. 1: System and control parameters for the base case.....	78
Apx Table B. 2: CCT and CCA for tested control parameters of droop control GFMI with weak SCR = 2 and SCR = 4 .....	78
Apx Table B. 3: CCT and CCA for tested control parameters of VSG control GFMI with SCR = 2 and SCR = 4.....	79
Apx Table B. 4: CCT and CCA for tested control parameters of CGVSG control GFMI with SCR = 2 and SCR = 4 .....	80
Apx Table B. 5: Summary of findings.....	80
Apx Table C. 1: System for the 5-bus system: base case.....	81
Apx Table D. 1: Resulting SEP and UEP voltage and angle values from the developed tool.....	87
Apx Table D. 2: Computed DEP values from the developed tool.....	88

## Acknowledgments

The research presented in this report is funded by CSIRO as part of its contribution to the Australian Research in Power Systems Renewables Transition (AR-PST ) initiative. This work has been conducted with the support and collaboration of subject matter experts from both AEMO and CSIRO, whose insights and technical expertise have been invaluable in advancing this research.

This study aims to support Australia's transition to a stable, secure, and affordable power system, addressing key challenges associated with the increasing penetration of IBRs. The findings contribute to critical research identified under AR-PST , which is essential for accelerating the decarbonisation of the electricity grid and enhancing grid stability and resilience.

We extend our sincere gratitude to the technical experts and project advisors from CSIRO and AEMO, whose contributions have played a pivotal role in shaping the methodologies and outcomes of this work. Their expertise in power system dynamics, grid stability, and renewable integration has provided essential guidance throughout the research process.

We would also like to acknowledge Dr. Jinghze Xu for his contribution to the project through the provision of the voltage loop tuning method, which has informed key aspects of our analysis and design approach. Details of this contribution are provided in Appendix E.

More details on the AR-PST initiative can be found at:

<https://www.csiro.au/en/research/technology-space/energy/G-PST-Research-Roadmap>



# Executive Summary

This report addresses critical challenges related to large-signal transient stability in power grids increasingly dominated by inverter-based resources (IBRs), particularly grid-forming inverter (GFMI) technologies essential for Australia's renewable energy transition. It aligns with [Research Roadmap tasks](#) 4.1, 4.2, and 4.3, and delivers significant methodological and practical advancements for planning, operating, and managing IBR-intensive networks through four interconnected research tasks.

The research is structured around these four tasks, each building progressively on insights and methodologies developed throughout the project to establish a robust framework for transient stability assessment and operational improvement:

## **Task 1. Enhancement of Large-Signal Stability Analysis Tool:**

- Significantly upgraded the previously developed stability analysis tool by integrating inverter control loop dynamics.
- Enabled accurate estimation of transient stability margins and system responses under disturbances.
- Validated using detailed electromagnetic transient models (PSCAD), demonstrating close agreement with real-world scenarios, including the West Murray Zone.
- Investigated a range of operational scenarios, including slack bus location, network topology, integration of new power plants, and tuning of control gains.
- Confirmed utility in network planning and operational decision-making, particularly in weak grid scenarios and renewable energy zones.

## **Task 2. Sensitivity Analysis of Control Parameters and Fault Conditions:**

- Conducted extensive analyses assessing the impact of system parameters (e.g., inertia, damping, short-circuit ratio (SCR)) and control loop settings on transient stability.
- Key findings:
  - Inner control loops minimally affect critical clearing time (CCT) in weaker grids but influence post-fault recovery dynamics.
  - Grid strength and damping significantly influence transient stability margins and the domain of attraction, thereby affecting overall system resilience.
  - Assessed sensitivity to fault characteristics, highlighting how fault location, duration, and severity influence system dynamics.
- Developed a computationally efficient method for parameter sensitivity analysis, significantly reducing reliance on extensive time-domain PSCAD simulations.

## **Task 3. Stability Assessment Extension to Multi-IBR Networks:**

- Expanded the developed stability assessment framework using Lyapunov-based methods for multi-IBR configurations, enabling efficient calculation of system-wide CCT.
- Identified critical interactions among multiple GFMI, including:
  - Importance of considering current limiting behaviours in stability assessments.
  - Effects of inertia, damping, power references, and line impedances on system stability.
- Provided actionable insights for inverter placement, coordinated tuning, and contingency planning.

## **Task 4. Practical Tuning and Design Guidelines:**

- Formulated comprehensive and practical control tuning guidelines aligned with the National Electricity Rules (NER Schedule 5.2) for GFMI deployment.
- Emphasised that traditional single-input single-output tuning approaches are inadequate for multi-IBR systems due to significant plant-to-plant interactions.
- Recommendations include:
  - **Virtual Inertia:** Higher virtual inertia improves transient stability margins (longer CCT), balancing against energy storage constraints.
  - **Damping Settings:** Increased damping gains enhance both transient and small-signal stability, especially in strong-grid scenarios.
  - **Droop Coefficients:** Lower droop gains generally yield improved transient and small-signal stability, but require careful balancing against the operational capabilities of inverter energy storage.
- Highlighted the critical role of coordinated, system-aware tuning methods to achieve optimal grid performance and regulatory compliance.
- Emphasised the importance of simulation under realistic grid conditions for validating tuning strategies, ensuring robustness, and industry readiness.

#### **Delivered PSCAD Model:**

To facilitate practical application and adoption of the proposed tuning guidelines and design recommendations, the project has developed and delivered a comprehensive PSCAD simulation model. This model incorporates:

- Detailed representation of GFMI, covering key control layers (primary, voltage, and current loops) with adjustable parameters based on provided guidelines.
- Automated tuning procedures aligned with the recommended methodologies, enabling easy exploration and assessment of inverter parameter variations.
- Flexibility for configuring system-specific parameters (e.g., inverter ratings, network strength, desired control performance metrics) to rapidly evaluate transient stability and dynamic responses.
- Ready-to-use framework for system operators, technical managers, and researchers to validate design choices and inform planning decisions in real-world scenarios.

Collectively, the outcomes of these tasks provide robust tools, validated methodologies, and practical guidelines essential for managing and enhancing stability, resilience, and operational performance in Australia's evolving renewable energy landscape. These results empower technical managers, system planners, and grid operators to effectively address transient stability challenges in high-renewable penetration scenarios, ensuring reliable and secure grid operation.

Future research priorities include extending the stability framework to asymmetrical fault scenarios, developing robust metrics for quantifying and applying system strength support, and improving the modelling of emerging inverter-based loads such as electrolyzers and data centres. Additional focus is needed on the integration and dynamic behaviour of current limiters in multi-IBR networks, particularly under fault conditions, to enhance fault ride-through and recovery performance. Advancements in coordinated control strategies for multi-IBR systems will be crucial to mitigate plant-to-plant interactions and ensure scalable tuning approaches. Furthermore, the application of artificial intelligence (AI) offers promising pathways for real-time stability assessment, adaptive control tuning, and predictive grid management in increasingly complex and dynamic power systems.

# 1 Introduction

## 1.1. Background and Research Objectives

The Australian energy landscape is undergoing a profound transformation, driven by the rapid integration of renewable energy sources such as wind and solar. This shift is leading to an increasing dependence on inverter-based resources (IBRs), which are progressively replacing conventional synchronous generators. While this transition is essential for achieving a sustainable and low-carbon energy future, it also introduces significant challenges in ensuring grid stability, reliability, and resilience.



Grid-forming inverters (GFMI) have emerged as a crucial technology in addressing stability concerns in power systems with high IBR penetration. These inverters play a fundamental role in stabilising the grid by regulating voltage and frequency, even in the absence of conventional generators. However, as power networks become increasingly complex, a deeper understanding of transient and large-signal stability is necessary to maintain grid security and operational efficiency.


Stage 4 of the Australian Research in Power Systems Transition (AR-PST) research builds on the findings of Stage 3, aiming to enhance the tools and methodologies required to assess and improve large-signal stability in IBR-dominated networks. The focus of this stage is structured around four key areas:

- **Advancement of Large-Signal Stability Analysis Tools:** This task seeks to provide a more robust framework for evaluating grid stability under various disturbance conditions by incorporating inverter control dynamics into existing stability assessment tools.
- **Sensitivity Analysis of GFMI:** This task explores the influence of control parameter variations and different fault scenarios on large-signal stability, enabling the identification of optimal configurations to enhance system robustness.
- **Extension to Multi-IBR Systems:** Investigating the dynamic interactions among multiple IBRs across various network topologies, this task offers insights into the collective impact of these resources on overall system stability.
- **Development of Tuning and Design Guidelines:** Based on the insights gained from the preceding tasks, this phase aims to formulate practical guidelines for the configuration and operation of GFMI, supporting the development of more stable and resilient power systems.

Table 1 shows the Research Roadmap tasks being addressed by Stage-4 research activities.

Table 1: Progress against research roadmap

Roadmap Major Tasks	Roadmap Tasks	Stage 4 Tasks	Progress <sup>1</sup>
4. Protection and Reliability	4.1: IBRs' effect on existing protection systems	<ul style="list-style-type: none"><li>• Task 2: Sensitivity analysis of GFMI stability with respect to parameter variation and fault profile.</li><li>• Task 3: Extension to Multi-IBR Systems.</li></ul>	
	4.2: Enhancing IBR response during and subsequent to faults	<ul style="list-style-type: none"><li>• Task 4: Development of Tuning and Design Guidelines.</li></ul>	

	4.3: Assessment and enhancement of IBRs reliability	<ul style="list-style-type: none"> <li>• Task 2: Sensitivity analysis of GFMI stability with respect to parameter variation and fault profile.</li> <li>• Task 3: Extension to Multi-IBR Systems.</li> <li>• Task 4: Development of Tuning and Design Guidelines.</li> </ul>	
<sup>1</sup> Progress to date against roadmap tasks.			

### 1.1.1. Building on Stage 3: Advancing Stability Assessments and Tools in Stage 4

The research in Stage 4 builds upon the methodologies and findings from Stage 3, addressing key limitations and extending the analysis to more complex system conditions. In Stage 3, a transient stability assessment tool was developed for GFMI-dominated networks under simplified assumptions, such as constant GFMI point of common coupling (PCC) voltages and constant grid-following inverter (GFLI) currents. Additionally, the impact of inner control loops on stability margins and the influence of different fault profiles and grid strength were not explicitly considered.

Stage 4 enhances this approach by incorporating the dynamic relationship between GFMI PCC voltage and GFLI currents while integrating inner control loop dynamics into the analysis. This improvement allows for a more comprehensive stability assessment, making the tool applicable to a broader range of grid conditions. Furthermore, based on insights from Stage 3, this stage expands the investigation into large-signal stability by systematically evaluating the impact of critical control parameters and fault characteristics. A novel method is developed to quantify the domain of attraction (DOA) and critical clearing time (CCT) for faults, providing deeper insights into protection strategies and control tuning.

Moreover, recognising the need for improved stability in multi-IBR systems, Stage 4 proposes a new method for calculating stability indices and CCT in large-scale systems, considering inverter interactions and network-wide dynamics. The outcomes of both stages contribute to the formulation of tuning and design guidelines for GFMI, ensuring robust operation under diverse grid scenarios. By integrating findings from Stage 3 with the advancements made in Stage 4, this research aims to provide a comprehensive framework for enhancing the transient stability of IBR-dominated networks while informing industry practices for GFMI tuning and deployment.

## 1.2. Research Relevance to Australia

Australia's transition toward a renewable energy future presents distinct challenges, particularly as the National Electricity Market (NEM) shifts from a system dominated by synchronous generators to one primarily reliant on IBRs such as wind, solar and batteries. While this transition aligns with national decarbonisation objectives, it introduces complexities in maintaining grid stability, reliability, and resilience. The reduction of system inertia and voltage control traditionally provided by synchronous generators has made the grid more susceptible to disturbances, particularly in regions with weak system strength, such as the West Murray Zone.

In this respect, Stage 4 of this research project aims to address these challenges by refining analytical tools and methodologies to enhance the stability of Australia's evolving power system. This includes the development of advanced stability assessment tools, optimisation of GFMI configurations, and improvement of multi-IBR system stability. By strengthening the stability of renewable energy zones (REZs), this research facilitates seamless integration of renewables while reducing dependence on costly infrastructure upgrades. For example, optimising inverter configurations in weak grid regions such as the West Murray Zone has the potential to significantly reduce capital expenditures by mitigating the need for extensive network reinforcements.

Beyond direct technical benefits, this research contributes to Australia's global renewable energy integration leadership by establishing best practices and scalable frameworks applicable to other nations undergoing similar transitions. The insights gained from this study provide practical solutions for enhancing grid stability and reliability in IBR-dominated networks, reinforcing Australia's position at the forefront of renewable energy adoption.

The outcomes of this research effort are expected to alleviate the technical challenges of the energy transition in the NEM by:

- Providing robust methodologies to assess and improve transient stability in weak grid regions.
- Developing practical guidelines for optimal GFMI configurations and reducing operational risks.
- Enhancing the cost-effectiveness of renewable integration by minimising the need for additional network infrastructure.
- Establishing a scalable framework that supports both national and international grid stability strategies.

Through these advancements, this research plays a pivotal role in ensuring Australia's power system remains secure, reliable, and adaptable as it transitions toward a high-penetration renewable energy future.

## 2. Research Completed

The research conducted in Stage 4 builds upon the findings and methodologies developed in Stage 3, addressing key limitations and expanding the scope of analysis to enhance the stability and resilience of IBR networks. Each task focuses on refining existing tools, conducting sensitivity analyses, extending stability assessments to multi-IBR systems, and developing practical tuning and design guidelines for IBRs to support large-scale renewable integration.

Task 1 in Stage 4 is primarily an extension of the stability margin analysis and computational tool developed in Stage 3, aiming to refine and expand its capabilities for larger IBR-dominated networks. While the Stage 3 tool provided valuable insights into transient stability, it had certain limitations to address. Stability margin calculations were based solely on inverter PCC angles, local common bus angles and voltages, and the global common bus voltage, without fully capturing the dynamic behaviour of the system. The influence of inner control loop parameters, which play a crucial role in inverter stability, was not considered. Additionally, simplifying assumptions, such as treating the PCC voltage of virtual synchronous generators (VSGs) and the current of Grid-following (GFL) inverters as constant values, limited the accuracy of the assessments.

Stage 4 enhances this methodology by incorporating the voltage and current dynamics at the PCC into the stability margin calculations. This allows for a more comprehensive system stability assessment, providing a more accurate representation of transient behaviour under varying grid conditions. Moreover, the enhanced stability analysis tool will be validated using real-world system data, ensuring its practical applicability and effectiveness in industry-relevant scenarios.

Task 2 in Stage 4 focuses on the sensitivity analysis of GFMI stability, examining the impact of parameter variations and fault profiles on transient stability. This involves a systematic review of existing transient stability analysis methods and CCT calculation techniques to assess their suitability for GFMI. The goal is to identify the most critical inverter control parameters affecting transient stability and assess their influence under different grid conditions. The expected outcome is a comprehensive understanding of how inverter settings impact system resilience, leading to the identification of optimal parameter ranges that enhance stability.

Additionally, Task 2 introduces a novel approach to CCT and DOA calculations, specifically tailored for GFMI. Unlike conventional methods, this approach considers the unique dynamics of fault type, location, and duration, providing a more accurate assessment of stability boundaries and fault recovery capabilities in IBR-dominated networks. This work is crucial for defining operational limits and improving fault ride-through capabilities of inverters.

Task 3 extends the large-signal stability analysis conducted in Task 2 to include networks with multiple IBRs, considering the diversity in inverter types and configurations. By integrating the advanced stability assessment methodologies developed in the previous tasks, this study examines the collective impact of multiple IBRs on system stability. This involves conducting stability margin assessments across various network topologies, identifying potential vulnerabilities, and proposing mitigation strategies. Extensive simulations and real-world case studies will be carried out to validate the effectiveness of these approaches. The insights gained will contribute to improving coordination strategies among different inverter types, ensuring stable operation even in complex network configurations.

Task 4 in Stage 4 focuses on developing tuning and design guidelines for IBRs, leveraging insights from the previous tasks. These guidelines will serve as a practical framework for optimising inverter control settings, improving transient stability, and enhancing coordination between multiple IBRs in diverse network

topologies. The recommendations will address key aspects such as voltage and frequency regulation, dynamic response optimisation, and fault recovery strategies. Furthermore, the guidelines will align with AEMO's voluntary specifications for grid-forming inverters, ensuring that they support industry standards and regulatory requirements.

## 2.1. Task 1: Enhancing the Large-Signal Stability Analysis Tool

### 2.1.1. Methodology

A generalised representation of the network studied in this task is shown in [Figure 1](#). This arrangement comprises multiple clusters, each representing a distinct renewable energy zone. Each cluster  $h$  consists of  $n$  GFMI and  $m$  GFLI units, all linked to a global common bus, which maintains a voltage of  $V_c \angle 0$ . The global common bus connects to an infinite bus with voltage  $V_g \angle \theta_g$  through the grid impedance  $Z_g$ . Within each cluster  $h$ , the GFMI unit  $h.n$  is connected to the local common bus  $h$  through  $Z_{FM,h,n}$ , while the GFLI unit  $h.m$  is connected to the same local common bus via  $Z_{FL,h,m}$ .

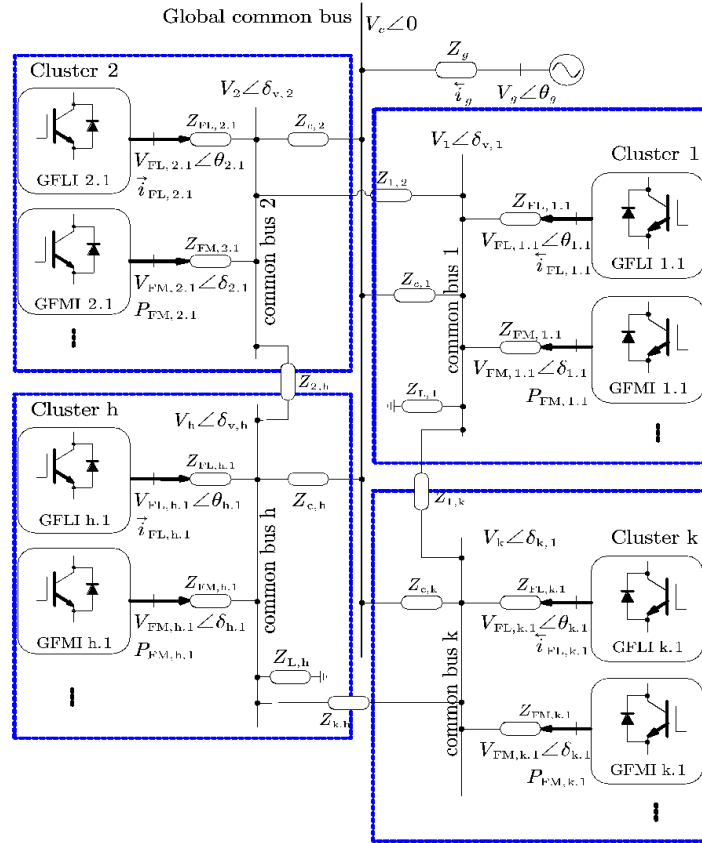


**Figure 1: Generalised representation of a multi-cluster multi-IBR network**

Additionally, clusters are interconnected via transmission lines characterised by impedance  $Z_{k,h}$ , which connects clusters  $k$  and  $h$ . Employing KCL [1],

$$\frac{V_h \angle \delta_{v,h} - V_c \angle 0}{Z_{c,h}} = \sum_{m=1}^{M_h} i_{FL,h,m} + \sum_{n=1}^{N_h} \frac{V_{FM,h,n} \angle \delta_{h,n} - V_h \angle \delta_{v,h}}{Z_{FM,h,n}} + \sum_{k=1}^{K_h} \frac{V_k \angle \delta_{v,k} - V_h \angle \delta_{v,h}}{Z_{k,h}} \quad (1)$$

where  $M_h$ ,  $N_h$ , and  $K_h$  denote the number of GFLI, GFMI, and interconnected clusters to cluster  $h$ , respectively. This equation can be broken down into the following relations :

$$V_h \cos(\delta_{v,h}) = |V_c| |Y_h| \cos(\theta_{Yh}) + \sum_{m=1}^{M_h} |i_{FL,h,m}| |Z_{eq,h}| \cos(\theta_{h,m} + \varphi_{h,m} + \theta_{eq,h}) \quad (2)$$

$$+ \sum_{n=1}^{N_h} |V_{FM,h,n}| |Y_{n,h}| \cos(\delta_{h,n} + \theta_{n,h}) + \sum_{k=1}^{K_h} |V_k| |Y_{k,h}| \cos(\delta_{v,k} + \theta_{k,h})$$

$$V_h \sin(\delta_{v,h}) = |V_c| |Y_h| \sin(\theta_{Yh}) + \sum_{m=1}^{M_h} |i_{FL,h,m}| |Z_{eq,h}| \sin(\theta_{h,m} + \varphi_{h,m} + \theta_{eq,h}) \quad (3)$$

$$+ \sum_{n=1}^{N_h} |V_{FM,h,n}| |Y_{n,h}| \sin(\delta_{h,n} + \theta_{n,h}) + \sum_{k=1}^{K_h} |V_k| |Y_{k,h}| \sin(\delta_{v,k} + \theta_{k,h})$$

where

$$Z_{eq,h} \angle \theta_{eq,h} = \left( \frac{1}{Z_{c,h}} + \sum_{n=1}^{N_h} \frac{1}{Z_{FM,h,n}} + \sum_{k=1}^{K_h} \frac{1}{Z_{k,h}} \right)^{-1}$$

$$Y_h \angle \theta_{Yh} = Z_{eq,h} \angle \theta_{eq,h} \times \frac{1}{Z_{c,h}} \quad (4)$$

$$Y_{n,h} \angle \theta_{n,h} = Z_{eq,h} \angle \theta_{eq,h} \times \frac{1}{Z_{FM,h,n}}$$

$$Y_{k,h} \angle \theta_{k,h} = Z_{eq,h} \angle \theta_{eq,h} \times \frac{1}{Z_{k,h}}$$

The methodology for Task 1 builds upon the generalised equations for calculating stability margins ( $D_{EP}$ ) presented in [1], addressing key limitations identified in previous analyses. While the existing tool provided valuable insights into transient stability, it did not fully capture the complex dynamic interactions within IBR-dominated networks.

Stability margin calculations were primarily based on inverter PCC angles, local common bus angles and voltages, and the global common bus voltage. However, this approach did not consider the influence of inner control loop parameters, which play a crucial role in shaping inverter response under disturbances. Additionally, simplifying assumptions were made, treating the VSG PCC voltage and GFLI current as constant values, despite their significant impact on system stability.

As shown in [1], critical values for  $V_h$  of GFMI and GFLI are obtained by  $V_h =$

$\frac{V_{FM,h,n}^2 G_{h,n} - \frac{2}{3} P_{o,h,n}}{V_{FM,h,n} [B_{h,n} \sin(\delta_{h,n} - \delta_{v,h}) + G_{h,n} \cos(\delta_{h,n} - \delta_{v,h})]}$  and  $V_h = \frac{I_{d,h,m} X_{h,m} + I_{q,h,m} R_{h,m}}{\sin(\theta_{h,m} - \delta_{v,h})}$ , respectively, showing that the VSG PCC voltage and GFLI current are essential variables that directly influence the system's transient stability. To achieve a more accurate stability margin calculation, it is necessary to incorporate these dynamics into the analysis, ensuring that the tool accounts for the full range of inverter behaviours under various grid conditions.

To incorporate VSG dynamics, the relation between  $v_{FM,h,n}$  and the local common bus angles and magnitudes must be determined. This can be achieved by analysing the power flow and voltage control loop of the GFMI. By defining  $G_{FM,h,n} = \frac{R_{FM,h,n}}{R_{FM,h,n}^2 + X_{FM,h,n}^2}$ ,  $B_{FM,h,n} = \frac{X_{FM,h,n}}{R_{FM,h,n}^2 + X_{FM,h,n}^2}$ , and  $Z_{FM,h,n} = R_{FM,h,n} + jX_{FM,h,n}$ , the active and reactive power injection from GFMI  $h.n$  in cluster  $h$  in Figure 1 to the common bus  $h$ , denoted as  $P_{FM,h,n}$  and  $Q_{FM,h,n}$ , are expressed as



$$P_{FM,h,n} = 1.5 \left( V_{FM,h,n}^2 G_{FM,h,n} - V_{FM,h,n} v_h B_{FM,h,n} \sin(\delta_{h,n} - \delta_{v,h}) \right) - 1.5 V_{FM,h,n} V_h G_{FM,h,n} \cos(\delta_{h,n} - \delta_{v,h}), \quad (5)$$

$$Q_{FM,h,n} = 1.5 \left( -V_{FM,h,n}^2 B_{FM,h,n} + V_{FM,h,n} V_h B_{FM,h,n} \cos(\delta_{h,n} - \delta_{v,h}) \right) - 1.5 V_{FM,h,n} V_h G_{FM,h,n} \sin(\delta_{h,n} - \delta_{v,h}). \quad (6)$$

By considering the droop-based reactive power controller, its output can be represented as

$$V_{FM,h,n,ref} = V_0 + k_{pq,h,n}(Q_{FM,h,n,0} - Q_{FM,h,n}), \quad (7)$$

where  $V_{FM,h,n,ref}$ ,  $V_0$ ,  $Q_{FM,h,n,0}$ , and  $k_{pq,h,n}$  represent the voltage reference for the voltage control loop, nominal voltage, reactive power set point, and proportional gain of the reactive power control loop of the GFMI  $h.n$ .

Since the voltage and current control loops operate at significantly higher bandwidths compared to the primary control loop [2], it is reasonable to assume that  $V_{FM,h,n,ref}$  and  $V_{FM,h,n}$  are nearly identical. Thus, by substituting for  $Q_{FM,h,n}$  from (6) into (7), and selecting the common bus voltage angles as the reference, solving for  $V_{FM,h,n}$  yields

$$V_{FM,h,n} = \frac{1.5 V_h [B_{FM,h,n} \cos(\delta_{h,n} - \delta_{v,h}) - G_{FM,h,n} \sin(\delta_{h,n} - \delta_{v,h})] + \frac{1}{k_{pq,h,n}} - \sqrt{\Delta}}{3 B_{FM,h,n}}, \quad (8)$$

where

$$\Delta = \left( 1.5 V_h [B_{FM,h,n} \cos(\delta_{h,n} - \delta_{v,h}) - G_{FM,h,n} \sin(\delta_{h,n} - \delta_{v,h})] + \frac{1}{k_{pq,h,n}} \right)^2 - 6 B_{FM,h,n} \frac{Q_{FM,h,n,0} k_{pq,h,n} + V_0}{k_{pq,h,n}}. \quad (9)$$

Using (8) and (9), the dynamics of the GFMI Point of Common Coupling (POC) voltage can be accurately incorporated into the analysis. These equations allow for a more comprehensive representation of the interaction between GFMI voltage, power injection, and grid conditions, ensuring that the influence of control dynamics and system variations on stability is properly accounted. By integrating these dynamics, the model provides a more precise assessment of the GFMI response to disturbances, improving the accuracy of stability margin calculations and system performance evaluations.

Without explicitly providing the GFMI current values  $I_{d,ref}$  and  $I_{q,ref}$ , the active power reference  $P_{FL,h,n}$  and reactive power reference  $Q_{FL,h,n}$  values can be directly input as parameters into the tool. This approach incorporates dynamics of the GFMI while increasing the accuracy in assessing system stability.

By following the same procedural steps outlined in [1], the stability margin  $D_{EP}$  of the system can be calculated accurately and efficiently. Incorporating these inverter dynamics ensures a more precise evaluation of the inverter's response to grid disturbances, leading to enhanced accuracy in stability margin calculations and a better understanding of system behaviour under varying conditions.

## Results

The 3-cluster network illustrated in Figure 2, comprising 7 IBRs, is used to demonstrate the improved performance of the stability margin calculation tool (referred to as Version 2), which incorporates the dynamics of inverter control loops. The detailed system parameters are provided in Apx Table A. 1.

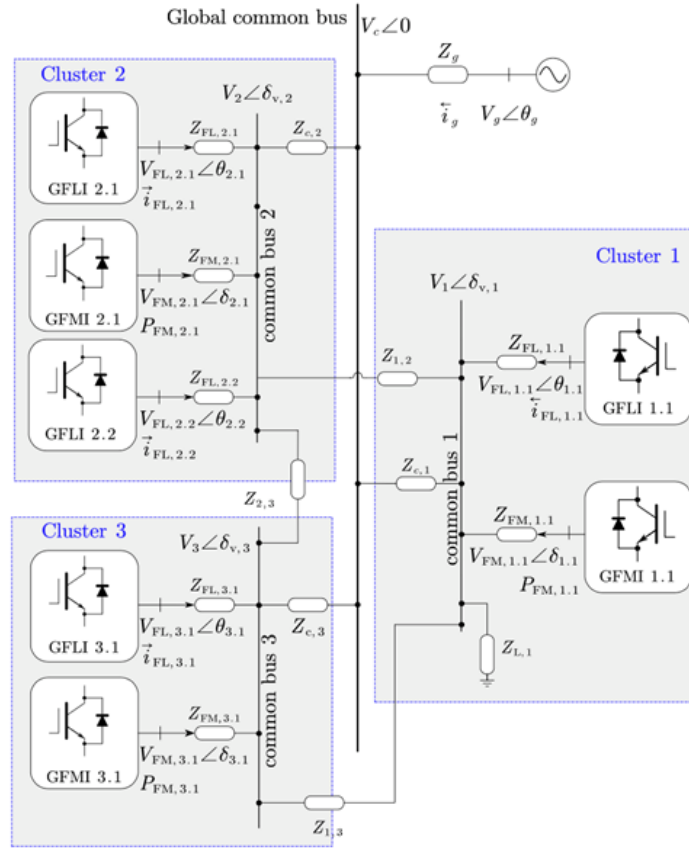


**Figure 2: Network diagram of the 3-cluster 7-IBR mesh network**

*Table 2: Comparison of transient stability margins obtained from the existing and updated tools under varied system parameters*

PARAMETER	CASE A	CASE B	CASE C
$P_{FM,1.1}$ (MW)	27.5	30.25	27.5
$Z_{c,1}$ [ $\Omega$ ]	$3.025+65.4488j$	$3.025+65.4488j$	$4.5375 + 98.173j$
$D_{EP}$ [PSCAD]	2.23	1.97	1.85
$D_{EP}$ [Tool ver1]	2.29	2.12	1.92
<b><math>D_{EP}</math> [Tool ver2]</b>	<b>2.22</b>	<b>2.048</b>	<b>1.84</b>

As shown in Table 2, in Case A, the reference PSCAD simulation yields a stability margin of 2.23. Version 2 of the tool closely matches this benchmark with an estimate of 2.22, indicating a notable improvement in accuracy compared to Version 1, which produced a margin of 2.29. In Cases B and C, the active power setpoint of GFMI1 and the line impedance are varied to assess the tool's robustness under different operating conditions. Across all cases, Version 2 consistently provides estimations that are more aligned with the PSCAD results than those of Version 1.

These findings confirm that incorporating inverter control dynamics significantly enhances the tool's accuracy. Furthermore, the improved tool facilitates faster and more reliable evaluation of transient stability, making it a practical framework for analysing the impact of control parameters on system stability under various network conditions.

### 2.1.2. Investigation of the West Murray Zone

A PSCAD model representing a section of the West Murray Zone is being developed to further validate the effectiveness of the enhanced stability assessment tool and gain deeper insights into system behaviour. This model aims to evaluate the transient stability implications of high IBR penetration and provide a framework for strategic inverter placement and tuning. As the initial step, a radial network model consisting of seven clusters with 19 IBRs has been constructed.

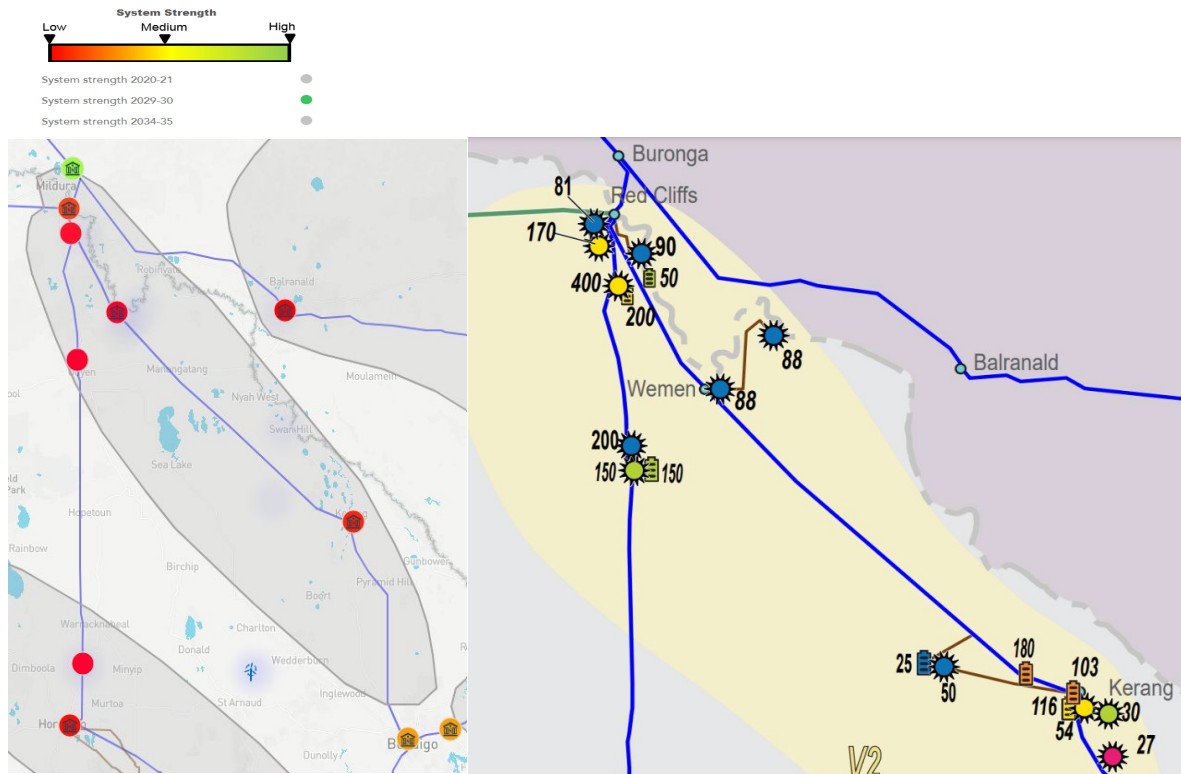


**Figure 3: WMZ and system strength levels [3],[4]**

In this study, batteries are modelled as grid-forming inverters, while solar farms are represented as grid-following inverters, providing a realistic approximation of the network's inverter composition. Line impedances are assigned proportionally to the geographical distances between nodes to preserve the physical accuracy of the network layout. Additionally, the active power reference of each power plant is based on the corresponding values indicated in the generation map [4], ensuring alignment with actual dispatch conditions.

Using the enhanced stability margin calculation tool, a series of sensitivity analyses were performed to investigate the influence of key factors on the transient stability of the West Murray Zone (WMZ). These include the location of the slack bus, variations in network configuration, and the placement of new power plants. In addition, dedicated studies were carried out to assess the impact of inverter control parameters, such as droop coefficients of the Reactive Power Control (RPC) loop in the GFMI control structure on the system's stability margin. The following sections provide a detailed description of these case studies and the insights gained.

## Results

### Validation of the Enhanced Stability Assessment Tool:

To validate the effectiveness of the enhanced stability assessment tool, a detailed PSCAD model of the WMZ was developed, with the ring network configuration selected as the base case. The system's critical clearing time was determined through a trial-and-error process using PSCAD simulations, and the corresponding angle deviations for each cluster were extracted from PSCAD plots.

For the same network, the enhanced tool was applied by inputting only the network data, enabling a rapid estimation of the stability margin for each cluster. As shown in [Table 3](#), the values estimated by the tool closely match those obtained from the PSCAD-based benchmark, confirming the method's accuracy and reliability. These results demonstrate the tool's capability to efficiently and accurately assess transient stability margins for networks of any scale and with any number of IBRs.

*Table 3: Comparison of transient stability margins obtained from PSCAD and Tool*

CLUSTER	$D_{EP}$ [PSCAD]	$D_{EP}$ [Tool]
1	1.56	1.58
2	1.51	1.51
3	1.42	1.42
4	1.61	1.64
5	1.40	1.40
6	1.46	1.53
7	1.41	1.47
<b>System <math>D_{EP}</math></b>	<b>1.40</b>	<b>1.40</b>

As shown in [Table 3](#), the tool enables the calculation of cluster-wise stability margins, with the system's overall stability margin being the lowest among the cluster values. In this case, Cluster 5 exhibits the lowest margin, indicating that it is the most vulnerable to instability under the current network arrangement. This highlights the need for special operational attention and potential design improvements for this cluster. By applying targeted modifications to inverter settings and network arrangements, the tool can be used to identify effective strategies to enhance the stability margin of Cluster 5 and, consequently, the overall system.

### Impact of Slack Bus Location on Stability Margin:

The second study investigates how the location of the slack bus influences the system's transient stability margin. Two test cases were considered: in the first, the slack bus was placed at Bendigo, a location with medium system strength as indicated in [Figure 3](#); in the second, it was positioned at Buronga, a location characterised by high system strength.

Conducting this analysis using PSCAD would require extensive modifications to network files and simulation settings, making the process time-consuming. In contrast, with the enhanced stability assessment tool, the analysis was performed efficiently by simply updating the network impedance data to reflect the slack bus relocation. This demonstrates the tool's practicality and effectiveness in rapidly evaluating how changes in grid configuration, such as slack bus placement, affect system stability.

Table 4: Comparison of stability margins for different slack bus locations and network arrangements

TEST	$Z_{1,2}$	$Z_{1,3}$	$Z_{1,4}$	$Z_{1,5}$	$Z_{1,6}$	$Z_{1,7}$	$Z_{2,3}$	$Z_{2,4}$	$Z_{2,5}$	$Z_{2,6}$	$Z_{2,7}$	$Z_{3,4}$	$Z_{3,5}$	$Z_{3,6}$	$Z_{3,7}$	$Z_{4,5}$	$Z_{4,6}$	$Z_{4,7}$	$Z_{5,6}$	$Z_{5,7}$	$Z_{6,7}$	$D_{EP}$ BENDIGO	$D_{EP}$ BURONGA
1	0	0	0	0	0	0	0	0	0	0	0	0	0	0	0	0	0	0	0	0	0	LSEP/ unstable	LSEP/ unstable
2	1	0	1	0	0	0	1	0	0	0	0	0	1	0	0	0	1	0	0	1	1	1.4000	0.2095
3	1	1	1	1	1	1	1	1	1	1	1	1	1	1	1	1	1	1	1	1	1	1.5381	0.1570
4	0	0	0	0	0	0	1	1	1	1	1	1	1	1	1	1	1	1	1	1	1	0.2228	LSEP/ unstable
5	0	1	1	1	1	1	0	0	0	0	0	1	1	1	1	1	1	1	1	1	1	LSEP/ unstable	0.17466
6	1	0	1	1	1	1	0	1	1	1	1	0	0	0	0	1	1	1	1	1	1	LSEP/ unstable	0.16421
7	1	1	0	1	1	1	1	0	1	1	1	0	1	1	1	0	0	0	0	1	1	LSEP/ unstable	0.16238
8	1	1	1	0	1	1	1	1	0	1	1	1	0	1	1	0	1	1	0	0	1	LSEP/ unstable	0.15065
9	1	1	1	1	0	1	1	1	1	0	1	1	1	0	1	1	0	1	0	1	0	LSEP/ unstable	0.15196
10	1	1	1	1	1	0	1	1	1	1	0	1	1	1	0	1	1	0	1	0	0	1.2765	LSEP/ unstable
11	1	0	1	0	0	0	0	0	0	0	0	0	0	0	0	0	0	0	0	0	0	LSEP/ unstable	LSEP/ unstable

\*LSEP: Lack of Stable Equilibrium Point

In Table 4, the variable  $Z_{k,h}$  represents the inter-cluster connections within the network, where a value of 0 indicates no connection and a value of 1 signifies the presence of a connection. Also, the term “LSEP/unstable” refers to configurations for which no stable equilibrium point exists, or where even minor disturbances cause a loss of synchronism between some or many units. This loss of synchronism may trigger protective relays, potentially resulting in partial or widespread network outages. By varying the network arrangement, the calculated  $D_{EP}$  values change accordingly, allowing the identification of the most stable configuration for a given slack bus location.

The different rows of Table 4 also allow for studying the impact of grid configuration on transient stability. The meshed network arrangement (Test 3) yields the highest stability margin when the slack bus is positioned in the Bendigo area. Conversely, when the slack bus is located in Buronga, the ring network configuration (Test 2) provides the greatest stability. Some configurations with low  $D_{EP}$  values were further tested in PSCAD simulations and were found to be unable to stably initiate, confirming the tool's predictive capability.

A current limitation of the tool is that it does not support direct comparison between different slack bus locations (e.g., Bendigo vs. Buronga) within the same analysis run. Therefore, comparisons between columns representing different slack bus placements in Table 4 should be interpreted separately. However, within a fixed slack bus location, the tool allows for a reliable comparison of various network arrangements to determine the most stable option.

### Integration of a New Power Plant into the West Murray Zone:

To demonstrate the practical application of the enhanced stability assessment tool, a case study was conducted involving the integration of a power plant of interest into the WMZ. As depicted in Figure 4, this power plant, listed in the 2024 NEM generation map [5], was introduced as the eighth cluster situated between Wemen and Kerang, with Bendigo designated as the slack bus location.

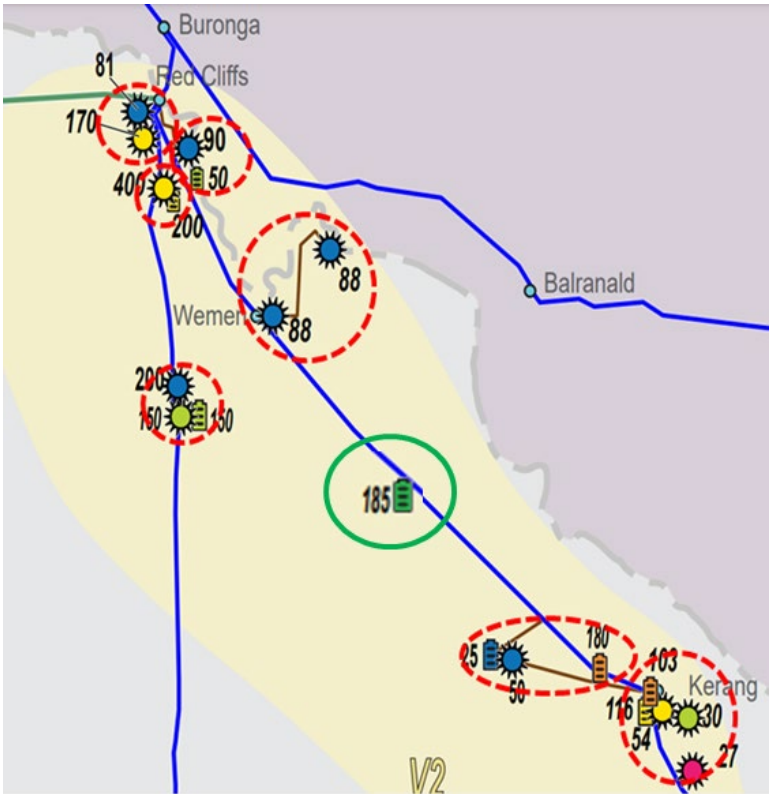


Figure 4: WMZ with the IBR of interest (Green) [5]

Table 5 presents the calculated stability margins for both ring and meshed network configurations incorporating the new cluster. The results indicate that adding the new power plant influences the system's stability margin, with variations observed between different network arrangements.

Table 5: Stability margins for different network arrangements with the IBR of interest

NETWORK	$D_{EP}$
Ring	1.7300
Mesh	1.8483

By performing various studies, the tool facilitates the identification of the most suitable connection points and network configurations for the new cluster. Furthermore, it enables the assessment of how different

inverter dispatch levels and control loop settings impact the stability margin. This capability allows for proactive stability studies prior to the physical installation of new power plants, ensuring informed decision-making and the implementation of measures to enhance overall system stability.

#### Impact of RPC Droop Gain on Transient Stability Margin:

With the integration of the RPC loop dynamics into the enhanced stability assessment tool, it is now possible to analyse how variations in RPC droop gain affect the transient stability margin of GFMI. This case study investigates the effect of different RPC droop settings on system stability.

Table 6: Stability margins for different RPC gains

TEST	$k_{pq,1.1}$	$k_{pq,3.1}$	$k_{pq,5.1}$	$k_{pq,6.1}$	$k_{pq,6.2}$	$k_{pq,7.1}$	$k_{pq,7.2}$	$D_{EP}$
1	1%	1%	1%	1%	1%	1%	1%	1.40
2	5%	1%	1%	1%	1%	1%	1%	1.72
3	5%	5%	5%	5%	5%	5%	5%	Unstable
4	1%	1%	1%	5%	1%	1%	1%	1.42
5	1%	1%	1%	5%	1%	5%	1%	1.35
6	1%	1%	1%	5%	5%	5%	5%	Unstable
7	5%	5%	5%	5%	1%	5%	1%	Unstable

As presented in Table 6, Test 1 applies a 1% droop coefficient to the RPC loop of all GFMI. In Test 2, the droop gain of a single inverter (denoted as  $k_{pq,1.1}$ ) is increased, resulting in an improvement in the overall system stability margin. However, Test 3 involves increasing the droop gains for all GFMI across the network, which leads to system instability.

These results demonstrate the tool's capability to evaluate the impact of droop gain tuning on stability. It provides valuable insights for selecting appropriate RPC droop settings to enhance the stability margin, both for existing grid-connected plants and during the integration of new power plants. This makes the tool particularly useful in network planning and operational decision-making processes.

#### Summary

The development of the large signal stability analysis tool in Stage 4 has delivered significant advancements in assessing the transient stability of multi-IBR systems under realistic grid conditions. Building on Stage 3, which assumed constant PCC voltages and GFLI currents. Stage 4 incorporates a more accurate representation of system dynamics by integrating control loop interactions, PCC voltage variations, and multiple inverters' dynamic behaviour.

Key improvements and outcomes include:

- **Integration of control loop dynamics:** The tool now accounts for the effects of reactive power controllers, enabling assessment of how these parameters influence transient stability. This enhancement addresses a critical gap in Stage 3.
- **Enhanced stability margin calculation:** The tool now provides improved accuracy in estimating transient stability margins by incorporating outer control loop dynamics. Validation results show close agreement with PSCAD simulations, confirming the tool's capability to assess system stability across radial and mesh networks.
- **Validation using real-world network model:** A detailed PSCAD model of the WMZ was developed to verify the tool's predictions under practical conditions. The tool demonstrated excellent agreement with time-domain simulations.



- **Application to operational and planning studies:** The tool was used to conduct a range of studies within the WMZ, including:
  - Assessment of the effect of slack bus location on system stability,
  - Evaluation of network topology variations and identification of optimal arrangements,
  - Analysis of newly registered power plant integration and its impact on system margins, and
  - Sensitivity analysis of RPC droop gains and their role in improving or degrading network stability.

These studies highlight the tool's versatility and practical utility in guiding decisions on inverter placement, tuning of control parameters, and pre-installation screening of new power plants.

Overall, the refined tool offers a robust, computationally efficient platform for power system operators, planners, and designers to assess and improve stability in inverter-dominated grids. The methodology is particularly relevant for weak-grid scenarios and renewable energy zones, enabling more secure and resilient grid operation in the transition to high-renewable energy systems.

### 2.1.3. Critical Learnings and Insights

The outcomes of Stage 4 have led to several important technical and operational insights relevant to both research and industry practice:

- **Inverter Control Dynamics Are Crucial:** Incorporating outer control loop dynamics significantly improves the accuracy of stability assessments. Ignoring these dynamics, as in previous approaches, can lead to misleading or overly conservative results.
- **Cluster-Level Analysis Enhances Visibility:** The ability to estimate stability margins at the cluster level enables targeted interventions. For example, identifying the weakest cluster in a network allows system operators to optimise local control settings or reinforce specific connections.
- **Slack Bus Location Matters:** The choice of the slack bus has a measurable impact on stability margins. High-strength slack bus locations (e.g., Buronga) support better performance for certain configurations, while others (e.g., Bendigo) may benefit more from meshed arrangements. These effects must be considered during network planning and reconfiguration.
- **Network Arrangement and Plant Integration Strategy:** The tool demonstrated the ability to rapidly test the impact of network arrangements and power plant additions on system stability. This supports proactive planning, helping to avoid configurations that could lead to unstable operation.
- **RPC Droop Gain Requires Careful Tuning:** While increasing the droop gain of individual GFMI's can improve local stability, indiscriminate adjustment across the network can introduce instability. This highlights the importance of coordinated tuning strategies based on system-wide analysis.
- **Tool Enables Pre-Installation Studies:** One of the most valuable outcomes is the ability to conduct detailed transient stability screening before the physical deployment of new IBRs. This facilitates more informed and cost-effective investment and operational decisions.

These learnings underscore the importance of moving beyond traditional static models and embracing dynamic, inverter-aware tools to support the secure and reliable operation of renewable-dominated power systems.



## 2.2. Task 2: Sensitivity Analysis of GFMI Stability with Respect to Parameter Variation and Fault Profile

### 2.2.1. Comprehensive Literature Review on Large Signal Stability Analysis and Critical Clearing Time Calculation Methods

To assess the stability characteristics of GFMI under large disturbances, an extensive review of existing large-signal stability analysis techniques and CCT calculation methods has been conducted. This review aims to identify current methodologies, their limitations, and potential improvements to apply for stability assessments for grid-forming inverters.

In large signal stability analysis, the focus is on identifying the existence of equilibrium points, which are stable equilibrium points (SEPs) and unstable equilibrium points (UEPs), and exploring the dynamics of the power angle as well as the stability boundary of the operating point. Given that large disturbances often trigger transient instability, the nonlinear properties of the system are pivotal for conducting transient stability (TS) analysis. Various methodologies are employed to analyse TS of GFMI qualitatively and quantitatively, including the power-angle analysis method, phase portraits, and Lyapunov's direct method. These methods are discussed in subsequent sections.

#### Power-Angle Analysis

Considering the simplified representation of the GFMI, as depicted in [Figure 5](#), and neglecting grid resistance, the power flow from the inverter to the grid is given by

$$P = \frac{|v_{pcc}| |v_g| \sin \delta}{x_g} \quad (10)$$

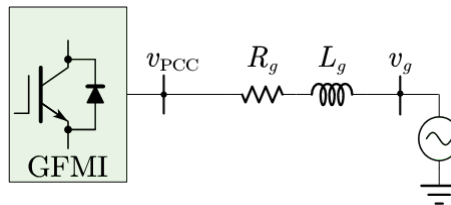


**Figure 5: Simplified diagram of a GFMI**

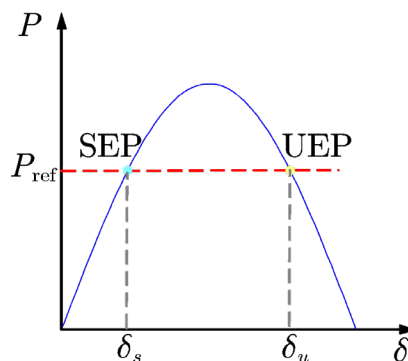


**Figure 6: Power-angle curve**

Due to the sinusoidal behaviour of the power-angle relation, the GFMI possesses two equilibrium points: an SEP and a UEP, as depicted in [Figure 6](#). In normal operations, the operating point is located at the SEP. Conversely, the UEP represents the initiation point for positive feedback within the synchronising loop [\[6\]](#).

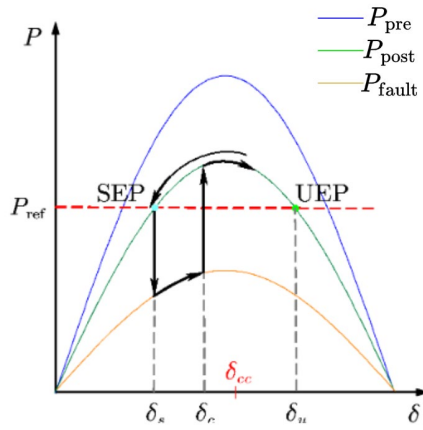


**Figure 7: Power-angle curve of a stable case**

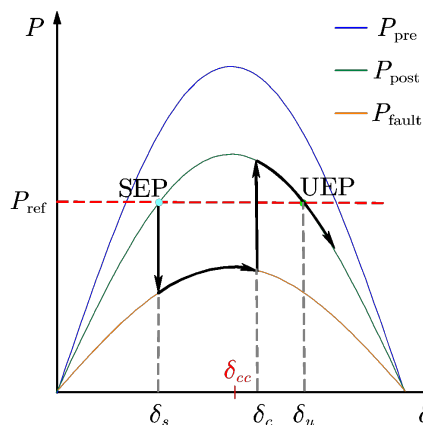


**Figure 8: Power-angle curve of an unstable case**

When operating without current limiters, a GFMI function in voltage control mode during a fault, displaying transient behaviours similar to those of a synchronous generator (SG). This response is governed by the swing equation, which defines the dynamics of the power angle. In Figure 7, it is worth noting that the post-fault  $P$ - $\delta$  curve is shown differently from the pre-fault  $P$ - $\delta$  curve to represent a general case in which system components, such as loads or transmission lines, may be disconnected following a fault. As illustrated in Figure 7, a fault in the system leads to a reduction in the maximum transferable power between the inverter and the grid. As a result, the power angle increases during the fault due to the mismatch between the injected power and the reference power. If the fault is cleared before the critical clearing angle (CCA)  $\delta_{cc}$ , the system can regain stability and return to normal operation, as shown in Figure 7. However, if the power angle surpasses  $\delta_{cc}$  during the fault, the system will lose synchronism, leading to instability as shown in Figure 8. To analyse the transient behaviour and determine the  $\delta_{cc}$ , time domain simulations are conducted. However, this approach encounters challenges, including significant computational demands and extended durations for simulations.

### Phase Portrait Analysis

As previously discussed, the large signal stability of the GFMI is closely tied to the dynamic response of the power angle  $\delta$  following a large disturbance. Given the nonlinear nature of this relationship and the involvement of the rate of change of the power angle  $\dot{\delta}$ , deriving an analytical solution becomes highly complex. To overcome this challenge, graphical techniques such as phase portrait analysis are utilised to study transient stability.

Phase portrait analysis involves plotting the system's state variables against one another, offering a visual representation of their trajectories over time [7]. This approach helps in understanding the evolution of system states, identifying stable and unstable operating conditions, and assessing the impact of disturbances on system stability.

To perform this analysis, it is first necessary to derive the dynamic equations that accurately describe the system's behaviour. These equations capture the nonlinear interactions within the power system, particularly the influence of inverter control dynamics on stability. Once formulated, software tools capable of solving nonlinear differential equations are employed to simulate and visualise the system's response [8]. This enables a more intuitive assessment of stability boundaries, equilibrium points, and transient behaviours, providing valuable insights for improving GFMI performance in IBR-dominated networks.

The transient behaviour of both droop-controlled GFMI and synchronous machine-based GFMI has been analysed using phase portrait techniques, as presented in [9]. As illustrated in Figure 9, when a fault occurs in the system, the power angle ( $\delta$ ) increases if  $\dot{\delta} > 0$  and decreases if  $\dot{\delta} < 0$ . The system attains stability at an SEP when  $\dot{\delta} = 0$ .

If the system has inertia, it exhibits an overshoot in the power angle, as shown in Figure 10, before settling into a stable state. The influence of control parameters on transient behaviour can be qualitatively assessed using this approach, providing insights into stability margins and system response characteristics. However, the accuracy of phase portrait analysis is highly dependent on the fidelity of the derived dynamic equations. Additionally, performing phase portrait studies for each scenario requires significant computational resources, making real-time applications challenging.

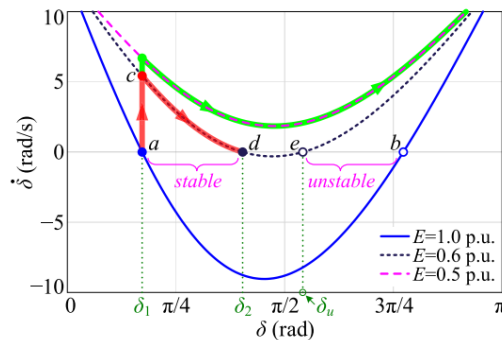


Figure 9: Phase portrait of the droop-controlled GFMI [8]

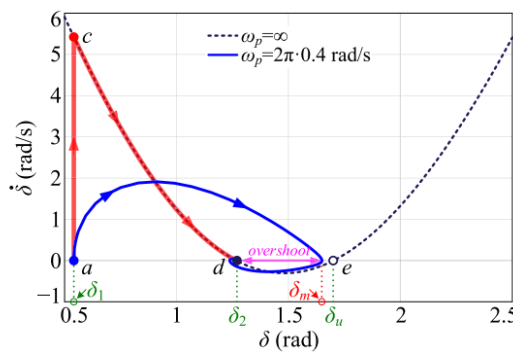


Figure 10: Phase portrait of the synchronous machine-based controlled GFMI [9]

## Lyapunov's Direct Method

In power system dynamics, equilibrium points represent steady states where all system forces are balanced, and no changes occur unless an external disturbance is introduced. These equilibrium points can be classified into three main types:

- **Stable Equilibrium Point:** A state where the system remains close to the equilibrium after a small disturbance.
- **Locally Asymptotically Stable Equilibrium:** A state where the system not only remains close to the equilibrium but eventually returns to it over time.
- **Unstable Equilibrium Point:** A critical boundary where, upon disturbance, the system diverges, leading to instability.

**Lyapunov's Stability Theory:** Lyapunov's direct method provides a mathematical framework for analysing the stability of nonlinear dynamic systems, making it particularly useful in power system stability studies. According to Lyapunov's stability theory, if a Lyapunov function  $V(x)$  can be defined within a region  $D$  in the state space such that

$$\begin{aligned} V(0) = 0 \text{ and } V(x) > 0 \text{ in } D - \{0\}; \text{ Positive definite function} \\ \dot{V}(x) \leq 0 \text{ in } D - \text{ Negative semi definite function,} \end{aligned} \quad (11)$$

then, the equilibrium point within  $D$  is stable. This ensures that for any initial condition within  $D$ , the system's trajectory will remain within this region, maintaining stability.

Furthermore, if  $\dot{V}(x)$  is strictly negative definite, the system is asymptotically stable, meaning it not only remains within the stability region but also converges back to the equilibrium point over time.

### Domain of Attraction in Power Systems:

In the context of power system stability, the domain of attraction represents the region in the state space where system trajectories naturally converge to the SEP after a disturbance [7]. As illustrated in Figure 11, if the post-fault condition remains within the DOA, the system stabilises and returns to normal operation. However, as shown in Figure 12, if the post-fault condition falls outside the DOA, the system loses stability and transitions toward an unstable state or an alternative operating point.

The size of the DOA is influenced by multiple factors, including grid strength, control parameters, and system dynamics. A larger DOA implies a wider stability margin, enhancing the system's resilience to disturbances. Accurately defining the DOA is crucial for quantifying stability margins, predicting system response to faults, and designing control strategies to ensure stable and reliable grid operation.

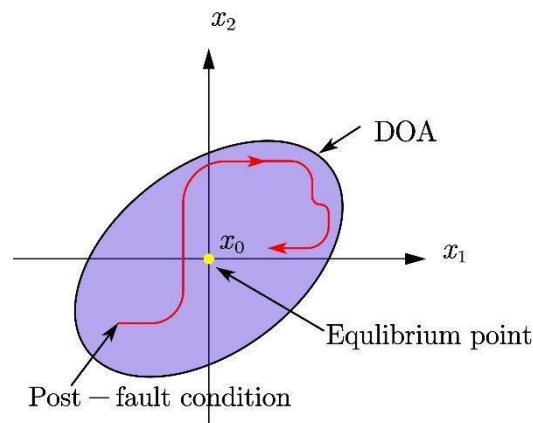


**Figure 11: Post-fault condition within the DOA -Stable case**

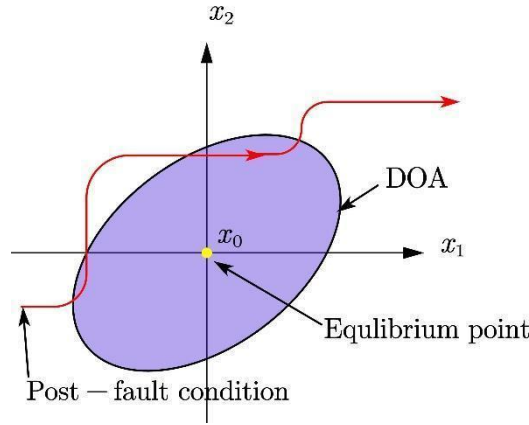


**Figure 12: Post-fault condition outside the DOA -Unstable case**

In the context of GFMI, Lyapunov's direct method provides a framework for assessing large signal stability without explicitly solving the system's differential equations. This approach is particularly valuable for nonlinear dynamic systems, such as GFMI, where analytical solutions are often impractical.

To apply Lyapunov's direct method for transient stability analysis in GFMI, a structured process is required. First, the system dynamics must be modelled, incorporating key state variables and their interactions through differential equations. Once the system model is established, a suitable Lyapunov function  $V(x)$  is selected or constructed [10]. Several approaches exist for constructing  $V(x)$ , including:

- Physically motivated Lyapunov functions, which consider the system's energy balance [7];
- Krasovskii's method, which utilises a derivative-based approach to define stability conditions [11], [12]; and
- The variable gradient method, which employs adaptive gradient-based criteria to formulate  $V(x)$  [13].

Once an appropriate Lyapunov function is identified, the DOA around a given equilibrium point can be estimated. The system's stability is determined by verifying whether the post-fault state lies within the DOA. If the system's state remains inside this region, it is guaranteed to be stable; otherwise, instability is expected to occur.

While extensive research has been conducted on transient stability analysis of SGs using Lyapunov's method, studies specifically focusing on GFMI remain limited. The transient instability of droop-controlled inverters has been explored in [14] and [15]. In [14], a second-order swing equation for a droop-controlled inverter was developed, and a Lyapunov candidate function was formulated to investigate transient stability issues. Study [15] examined the impact of current limiters on the transient instability mechanisms of droop-controlled inverters. Additionally, [16] proposed an approximate Lyapunov method to estimate the transient stability of VSGs, incorporating the effects of the RPC loop.

However, existing studies do not fully account for the interactions between control loops or the influence of varying grid conditions when constructing the Lyapunov function. Developing a generalised Lyapunov function that can accurately represent GFMI dynamics across different control strategies and grid conditions remains a significant challenge, requiring further research and refinement.

### Stability Margin Calculation Methods

To quantitatively assess large signal stability, various stability margin calculation methods have been proposed in the literature. These methods play a crucial role in system planning and operation, ensuring that stability constraints are maintained under different operating conditions. One of the key metrics used for evaluating system stability is the CCT, which represents the maximum allowable fault duration before

system instability occurs. If a fault is not cleared within this time frame, the system loses synchronism, potentially leading to cascading failures and collapse [17].

Several approaches have been developed to determine CCT, including:

- Forward numerical integration of the Lyapunov function [18], which evaluates system trajectories without requiring explicit time-domain simulations;
- Time-domain simulations [19], which assess system stability by directly modelling its response to disturbances; and
- Transient energy function analysis [20], which examines the system's ability to absorb and dissipate transient energy.

Beyond CCT-based approaches, transient stability can also be evaluated using the transient stability index (TSI), which is derived from the transient energy function. This method compares:

- The total transient energy ( $E_{cl}$ ), which represents the kinetic and potential energy injected into the system during a fault; and
- The critical energy ( $E_{cr}$ ), which reflects the system's post-fault energy absorption capability.

The TSI is computed as the difference between  $E_{cr}$  and  $E_{cl}$  relative to  $E_{cr}$ :

$$TSI = \frac{E_{cr} - E_{cl}}{E_{cr}} \quad (12)$$

A positive TSI (i.e., when  $E_{cr} > E_{cl}$ ) indicates that the system is stable, whereas a negative TSI suggests potential instability [20].

While stability margin calculation methods for SGs are extensively documented, their application to GFMI remains relatively underexplored. Existing studies typically focus on single-inverter systems and do not account for larger networks with multiple IBRs. Furthermore, the influence of control loop parameters on TS margins has not been thoroughly examined, highlighting the need for extended research to refine these methods for IBR-dominated grids.

## Summary

A substantial portion of existing research on large signal stability analysis for GFMI often assumes that the impact of inner loops, RPC, and grid conditions is negligible. However, such assumptions do not accurately represent the complexities of real-world operational conditions, potentially limiting the applicability of these analytical strategies in practical scenarios. Dynamic interactions between control loops, variations in grid strength, and external disturbances significantly influence system stability, necessitating more comprehensive analytical methods that incorporate these factors.

Additionally, research on TS analysis of compensated generalised VSG (CGVSG) [21] remains limited. Most existing approaches are designed for a single type of GFMI and lack generalisation across different control strategies, often focusing only on SMIB models or small networks. This limitation highlights the need for a robust TS assessment methodology applicable to various types of GFMI and larger network configurations.

Among available methods, Lyapunov's direct method is the most suitable approach for obtaining a quantitative stability margin in GFMI-dominated grids. Unlike conventional techniques, it provides a direct mathematical framework for evaluating stability margins, avoiding the computational intensity of extensive time-domain simulations. This approach is particularly effective for large-signal stability assessment, determining DOA, and estimating CCT under different operating conditions.

Following a comprehensive literature review, Lyapunov's direct method has been identified as the most effective technique for obtaining a clear understanding of stability boundaries in IBR-dominated grids. Its capability to provide a precise quantitative measure of TS margins makes it essential for ensuring the

secure and resilient operation of GFMI-based networks while accommodating various control strategies and grid conditions. Further refinement of this method is necessary to enhance its applicability to multi-IBR systems and large-scale networks, ensuring alignment with real-world grid operations.

### 2.2.2. Impact Assessment of Inverter Parameters on Stability

#### PSCAD Model Development

Detailed PSCAD models have been developed for droop, VSG, and CGVSG GFMI systems under single-machine infinite bus (SMIB) conditions to facilitate time-domain simulations. These models incorporate multiple control levels, as outlined in [22], ensuring a comprehensive representation of GFMI dynamics.

As shown in Figure 13, the GFMI model is connected to an ideal grid with an adjustable short circuit ratio (SCR) and  $X/R$  ratio. This configuration allows for the introduction of various fault types and grid disturbances, enabling the investigation of transient behaviour under different operating conditions. By systematically analysing the impact of control parameters on stability, these models serve as benchmark references, forming the basis for further sensitivity studies and performance evaluations in IBR-dominated networks.

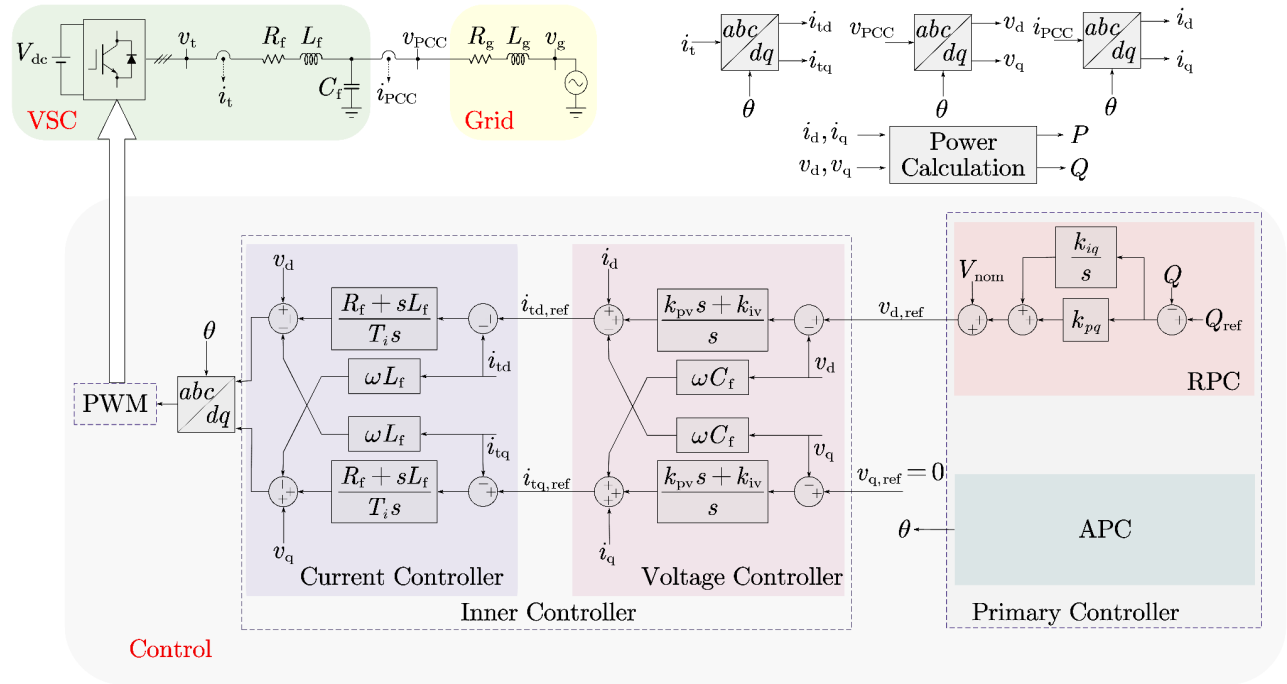


**Figure 13: Single-line diagram of a three-phase grid-connected inverter with a grid-forming control**

#### Time-domain Simulations

This section presents a detailed time-domain analysis to assess the performance of three grid-forming control (GFM) control strategies. The evaluation utilises CCA and CCT as key metrics to quantify TS under varying grid conditions and control parameters.

The base case parameters used in this study are provided in Apx Table B. 1. The droop coefficient for APC is set at 1%, while  $k_{pi}$  and  $k_{ii}$  values are determined based on Section 2.1, using a current control loop time constant of 1/1500 to achieve the desired rise time. The voltage control loop's proportional and integral gains are selected to ensure the CC loop operates at a higher bandwidth than the voltage control loop, maintaining proper control hierarchy [23]. The control parameters  $a$ ,  $b$ , and  $c$  are derived from the baseline  $D_p$  and  $J$  values, following the formulation outlined in [21].



## Impact of grid SCR on TS

The impact of grid SCR variations on TS and GFMI performance is thoroughly examined using the developed model. Two case studies are conducted, considering SCR values of 2 and 4, while maintaining a constant  $X_g/R_g$  ratio of 7. In both cases, GFMI operate with reference values of  $P_{ref} = 0.8$  MW and  $Q_{ref} = 0$  MVar. A three-phase fault is introduced at 15 seconds, lasting 0.8 seconds, after which the system returns to its pre-fault state.

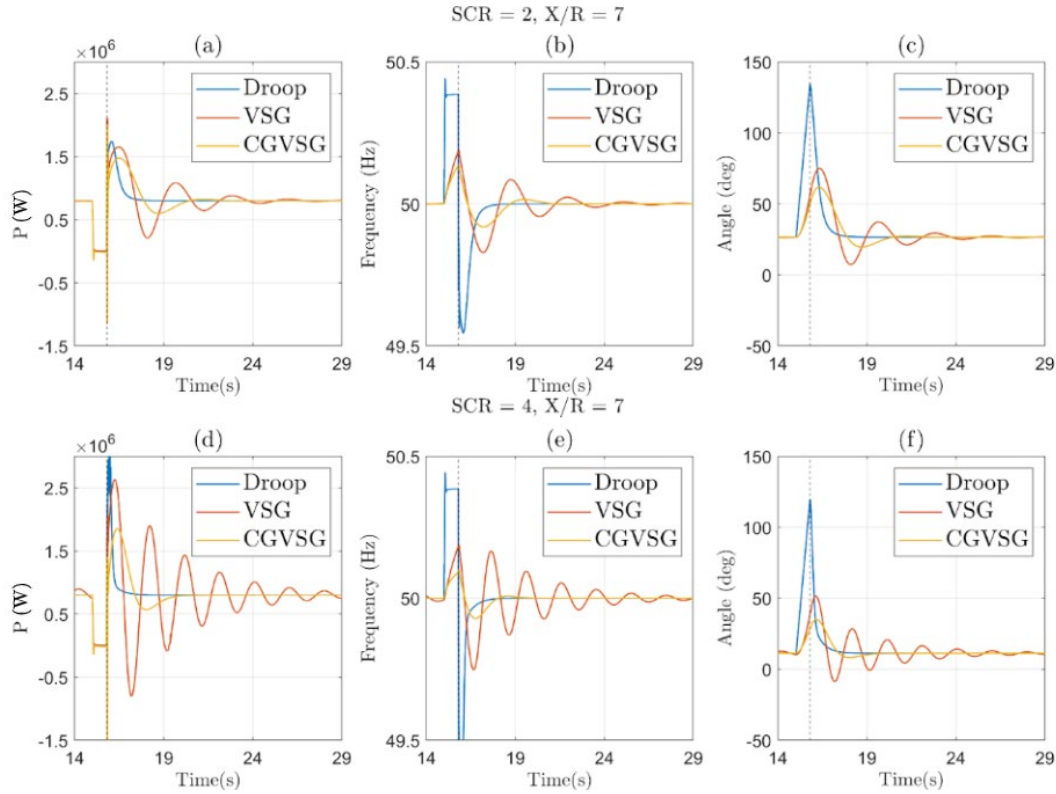


**Figure 14: Performance of the GFMI under three-phase fault at the grid: (Top) SCR=2, (Bottom) SCR=4 . (a), (d) PCC active power. (b), (e) Internal frequency signal of the GFMI. (c), (f) Power angle of the GFMI (relative to the infinite bus)**

In the swing equation framework, as inertia approaches zero, the system behaves as a droop-controlled GFMI, exhibiting a transient response with minimal post-fault oscillations and quickly stabilising at its pre-fault level, as depicted in Figure 14. However, during the fault, frequency and angle deviations are more pronounced compared to the other controllers. VSG and CGVSG experience power angle overshoot post-fault, followed by oscillations before returning to the SEP. Between the two, CGVSG displays fewer oscillations, indicating a smoother transition after fault clearance.

The influence of grid strength on TS is evident across all controller responses, with lower power angle deviations observed under lower SCR conditions. VSG exhibits significant oscillations in its internal and PCC signals post-fault, as shown in Figure 14(d), (e), and (f), requiring more time to reach the SEP. Conversely, CGVSG stabilises more efficiently, with fewer oscillations and a faster return to SEP in both grid conditions compared to the VSG. These findings emphasise the critical role of grid strength in shaping transient responses across different control strategies.

## Impact of Control Parameters on Transient Stability

This section examines the influence of control parameters on the transient behaviour of GFMI under weak and strong grid conditions, particularly in scenarios involving a three-phase fault. Simulation results are presented in Apx Table B. 2, Apx Table B. 3, and Apx Table B. 4, documenting CCT and CCA outcomes for



each test case. Parameters are evaluated under three conditions: base, decreased, and increased settings, and corresponding results are highlighted in each table.

#### **Droop-Controlled GFMI:**

As shown in [Apx Table B. 2](#), under base case parameters, the system exhibits a CCT of 0.97 seconds and a CCA of 157.853° in weak grid conditions. In contrast, when increasing the grid strength, CCT increases to 1.07 seconds, while CCA rises to 169.310°. This increase is attributed to the enhanced power transfer capability, which contributes to improved stability by providing a greater buffer before reaching critical operational limits.

Increasing the power reference leads to a decrease in both CCT and CCA, as it reduces the distance between SEP and UEP, increasing instability risks. The droop coefficient significantly influences CCT, where a lower droop coefficient results in an increase in CCT since smaller droop values lead to smaller frequency deviations for a given power change. However, CCA remains unaffected by variations in the droop coefficient in both grid conditions.

Based on CCT and CCA analysis, variations in the voltage controller's proportional and integral gains have no significant impact on large-signal stability. Additionally, increasing the time constant of the current controller reduces its proportional and integral gains, as described in [\[22\]](#); however, simulation results confirm that this has negligible influence on transient behaviour. Similarly, changes in RPC control parameters do not significantly affect CCT or CCA, suggesting that inner control loops and RPC have minimal influence on transient stability in droop-controlled GFMI under both low and moderate grid strength conditions. Nevertheless, further investigation is required to assess the potential impact of RPC in very high grid strength scenarios, where its influence may become more pronounced.

#### **VSG-controlled GFMI:**

Similar to droop control, the VSG exhibits higher CCT and CCA as the grid SCR increases, as shown in [Apx Table B. 3](#). The dispatch level affects transient behaviour, where a lower power reference results in higher CCT and CCA. Decreased droop coefficient increases the damping ratio, leading to improved CCT and CCA since greater damping reduces the acceleration area while increasing the deceleration area in the transient process, enhancing stability.

As the SCR increases, the VSG exhibits significant oscillations under higher droop coefficient values, leading to reduced stability during large disturbances. The inertia constant positively correlates with CCT, as an increase in virtual inertia reduces the rate of power angle variations. However, higher inertia negatively impacts CCA, as it causes larger overshoots post-fault clearance. As indicated in [Apx Table B. 3](#), the parameters of inner control loops and RPC have negligible influence on transient behaviour across a range of grid conditions.

#### **CGVSG-controlled GFMI:**

According to [Apx Table B. 4](#), CCT and CCA are negatively correlated with power dispatch level under both grid conditions. As described in [\[21\]](#), variations in  $D_p$  influence other CGVSG control parameters, making it different from other controllers. Unlike droop and VSG controllers, CGVSG does not exhibit a direct correlation between the droop coefficient and TS in weak grid conditions.

An improvement in CCT is observed with increasing SCR conditions, while CCA remains largely unaffected. Higher  $J$  values improve transient behaviour in weak grids, while in strong grids, CCT increases with higher  $J$  values, yet CCA remains unchanged. As with other controllers, inner control loops and RPC parameters have minimal influence on TS in CGVSG under both grid conditions.

## Comparison of GFMI Controllers under Fault Conditions

Figure 15 illustrates the response of three controllers under a three-phase fault, analysed up to the CCT of each controller while using base case parameters in weak grid conditions.

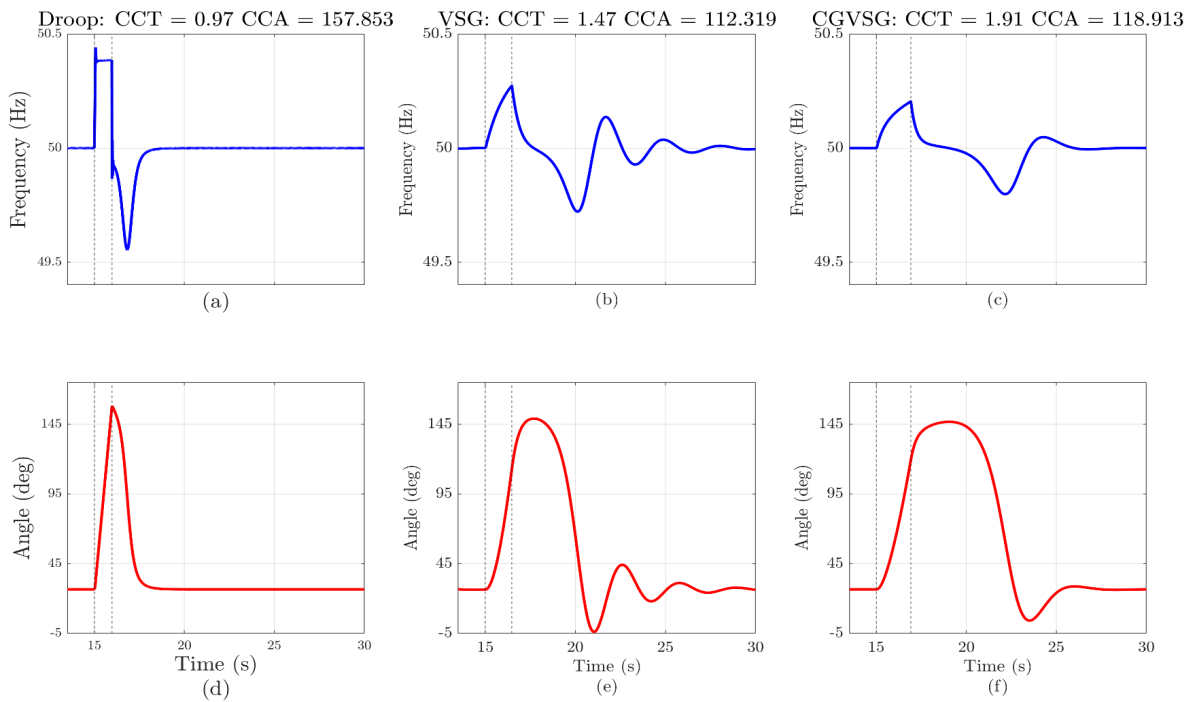


**Figure 15: Time-domain results for three-phase fault up to CCT of each controller for base case (a), (b), (c) frequencies. (d), (e), (f) power angle**

The droop-controlled GFMI, characterised by its first-order control dynamics, exhibits lower CCT and higher CCA, along with significant frequency and angle deviations during the fault period. This behaviour indicates a fast but less stable response to grid disturbances, making it more susceptible to transient instability.

In contrast, the CGVSG achieves the highest CCT, demonstrating superior transient stability compared to other controllers. It maintains lower frequency deviations during the fault, effectively damping fluctuations and ensuring a more stable operation. Additionally, CGVSG recovers quickly post-fault, outperforming VSG in terms of both stability and recovery speed.

The VSG, operating as a second-order system, exhibits high post-fault oscillations, reflecting its synthetic inertia and damping characteristics. This results in longer recovery times, requiring more time to stabilise after disturbances. The extended oscillatory behaviour indicates that additional tuning may be necessary to improve its transient performance in weak grid conditions.

## Summary

Ap<sub>x</sub> Table B. 5 summarises the findings on the impact of control loop parameters on CCA and CCT for GFMI<sub>s</sub> under different grid conditions. The results indicate that the inner control loops and RPC loop have negligible influence on TS, allowing for their exclusion in TS analysis without compromising assessment accuracy, thereby improving computational efficiency in system modelling.

The study confirms that CGVSG demonstrates superior robustness, especially as grid SCR increases, compared to VSG and droop-controlled systems. Additionally, reducing the power reference enhances system stability by increasing the distance between SEP and UEP, contributing to improved transient performance.

A positive correlation is observed between the damping coefficient and CCT for both droop and VSG systems, indicating that higher damping significantly enhances TS. For VSG, the inertia constant positively correlates with CCT but negatively with CCA, leading to mixed effects on TS.

These findings emphasise the importance of primary control loop parameters in transient behaviour analysis and CCT evaluation, underscoring the need for careful tuning of GFMI control strategies to optimise system stability across different grid conditions.

### 2.2.3. Development of A Novel CCT Calculation Methodology

This study focuses on the development and validation of a novel CCT calculation method that incorporates the unique dynamics of GFMI. This method is designed to assess the influence of fault type, location, and duration on system stability, providing a more comprehensive approach to CCT estimation in inverter-dominated grids.

Based on the literature review, Lyapunov's theorem has been identified as a robust framework for this methodology, as it enables the estimation of the DOA and provides an accurate calculation of CCT for IBR-dominated networks.

Insights from [Section 2.2.2](#) play a critical role in shaping this approach. Key factors such as APC loop parameters including  $P_{ref}$ ,  $D$ , and  $J$  as well as grid conditions such as SCR variations, will be integrated into the Lyapunov function formulation. This ensures that the methodology is not only accurate but also practical for real-world applications, effectively capturing transient stability behaviour across different grid conditions and control settings.

#### Methodology

The Lyapunov function for the VSG was formulated by referring to literature on synchronous generators, adapting stability analysis techniques used for conventional power systems to an IBR-dominated framework. The objective was to develop a Lyapunov-based stability criterion that accurately characterises the transient behaviour of a GFMI and determines its stability under disturbances.

The methodology begins with the swing equation for the VSG, expressed as:

$$J\omega_0 \frac{d^2\delta}{dt^2} = P_{ref} - P - D \frac{d\delta}{dt} \quad (13)$$

where  $J$  is the moment of inertia,  $\omega_0$  is the nominal angular velocity,  $\delta$  represents the power angle,  $P_{ref}$  is the reference active power,  $P$  is the delivered active power, and  $D$  is the damping coefficient. These parameters define the system's transient behaviour and influence its stability response following disturbances.

To represent the system's dynamic behaviour, the following state variables were introduced:

$$\begin{aligned} x_1 &= x_2 = \delta \\ x_2 &= \dot{\delta} = \omega \end{aligned} \quad (14)$$

where  $\delta$  represents the power angle relative to the grid and  $\omega$  represents the power angle variation. This transformation enables the swing equation to be rewritten in state-space form, facilitating a Lyapunov-based stability assessment. To simplify the stability analysis, the post-fault SEP was shifted to the origin, allowing the system equations to be reformulated as:

$$\begin{aligned}\dot{x}_1 &= \omega \\ \dot{x}_2 &= \frac{D}{J\omega_0}x_2 - \frac{1}{J\omega_0}(P_e \sin(x_1 + \delta_s) - P_e \sin \delta_s)\end{aligned}\quad (15)$$

where:

$$\begin{aligned}\delta_s &= \left(\frac{P_{ref}}{P_e}\right) \\ P_e &= \frac{V_c V_g}{x_g}.\end{aligned}\quad (16)$$

Using the derived system dynamics, a Lyapunov function for the VSG was developed to quantify system energy and assess stability:

$$V(x) = \frac{1}{2}Jx_2^2 - P_e \cos(x_1 + \delta_s) + P_e \cos \delta_s - x_1 P_{ref} + \frac{D^2}{2J\omega_0}x_1^2 + Dx_1x_2 \quad (17)$$

The function satisfies the Lyapunov stability conditions  $V(x) > 0$  and  $\dot{V}(x) \leq 0$ .

With a suitable Lyapunov function established, the CCT determination procedure follows a structured approach, as illustrated in [Figure 16](#). This methodology applies Lyapunov's direct method to determine the maximum permissible fault duration before the system loses stability.

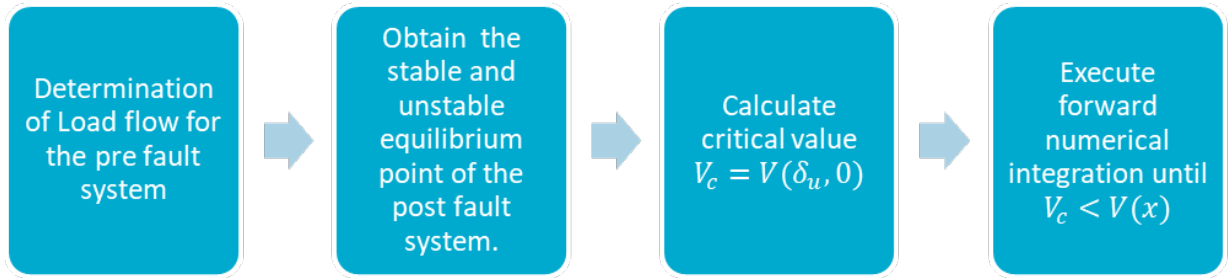


**Figure 16: Computer program flow chart for CCT calculation**

This formulation provides a mathematical foundation for analysing TS in VSG-based networks, offering insights into the effects of control parameters and grid conditions on system stability.

The process begins by obtaining the steady-state power flow solution of the pre-fault system, ensuring that the initial operating conditions are well-defined. Following this, the SEP and UEP of the post-fault system are identified. The SEP represents the stable equilibrium state, while the UEP defines the boundary between stability and instability.

Once these equilibrium points are established, the critical energy value  $V_c$  is calculated using the developed Lyapunov function. This value represents the maximum energy the system can sustain while remaining stable and is given by:

$$V_c = V(\delta_u, 0) \quad (18)$$

where  $\delta_u$  corresponds to the UEP. If the system's energy surpasses this threshold, it indicates a transition toward instability.

To determine the exact CCT, forward numerical integration is performed. Starting from the initial post-fault condition, the Lyapunov function  $V(x)$  is calculated. At each step, its value is compared against  $V_c$  to assess whether the system remains within stability limits.

The CCT is identified as the precise moment when  $V(x)$  exceeds  $V_c$ . This represents the maximum allowable fault duration before the system enters an unstable state. If the fault is cleared within this time, the system returns to its SEP, ensuring stability. However, if the fault persists beyond CCT, the system loses synchronism, leading to instability.

To further analyse stability, the DOA is determined by evaluating the Lyapunov function over a range of initial conditions. By applying phase portrait analysis, the system's trajectories in state space are mapped, revealing regions where the system naturally returns to its equilibrium state. This visualisation helps identify the stability boundary, which is influenced by parameters such as inertia, damping, fault profile, etc.

## Results

### Determination of Stability of Post-fault State:

The developed method enables a detailed analysis of the dynamic behaviour of the system, providing insights into stability characteristics under fault conditions. Figure 17 illustrates the DOA for the VSG in the studied system, based on the parameters presented in Apx Table B. 1.

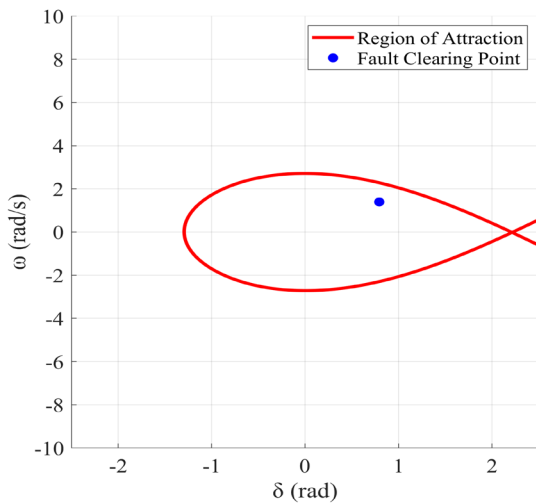


**Figure 17: Region of attraction with stable case: VSG**

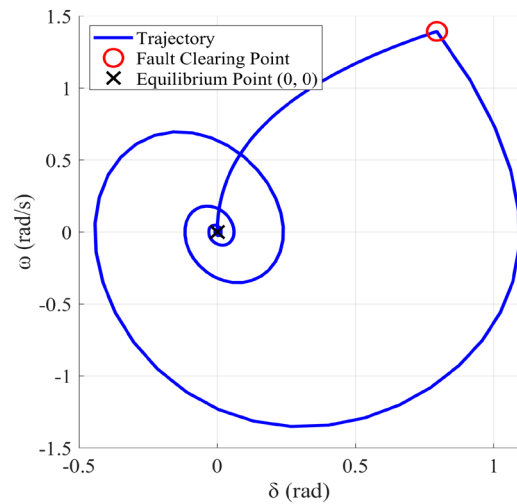


**Figure 18: Phase portrait dynamic of stable case: VSG**

When a fault occurs, the stability of the post-fault system can be determined by assessing the fault clearing point (blue dot). If the fault clearing point lies within the DOA, as depicted in Figure 18, the system successfully converges to the SEP, as demonstrated in Figure 19. Conversely, if the fault clearing point is outside the DOA, as shown in Figure 19, the system fails to regain stability, leading to instability, as illustrated in Figure 20.

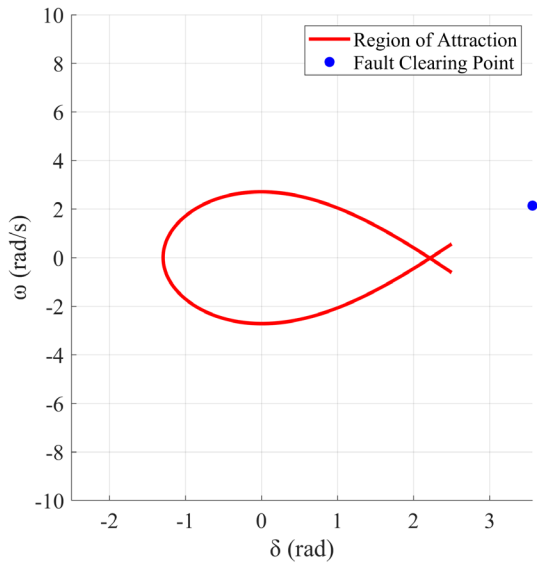


**Figure 19: Region of attraction with unstable case: VSG**

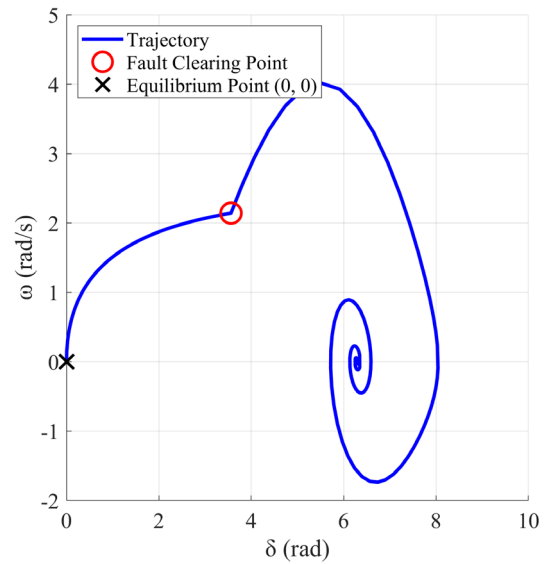


**Figure 20: Phase portrait of the dynamics of the unstable case: VSG**

#### Determination of CCT and CCA using Forward Integration:

By following the steps outlined in Figure 16, the CCT and CCA of the system can be efficiently determined using forward numerical integration. This approach allows for a precise estimation of the system's stability limits under fault conditions. As depicted in Figure 21, the CCT is identified as the exact time at which the Lyapunov function  $V(x)$  surpasses the critical energy threshold  $V_c$ . Once  $V(x)$  exceeds  $V_c$ , the system transitions into instability as shown in Figure 18, marking the CCT as the upper bound for fault duration before synchronism is lost. The CCA is determined by extracting the  $x_1(\delta)$  value at the corresponding time when the system reaches CCT, providing a critical measure of the system's post-fault stability boundary.

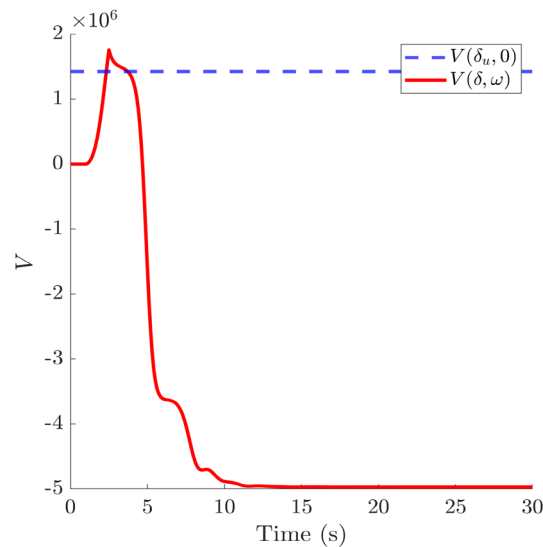


**Figure 21: Energy function value variation during the fault: VSG**

#### Validation of the Developed Method with PSCAD Simulations:

The VSG model in PSCAD was developed using the parameters listed in Apx Table B. 1, and the CCT and CCA of the system were observed through simulation. Traditionally, determining these values requires multiple trial-and-error tests, making the process computationally intensive, time-consuming, and prone to

inaccuracies. Identifying the precise CCT and CCA through conventional simulations often involves repeated fault-clearing experiments, increasing the complexity of stability assessments.

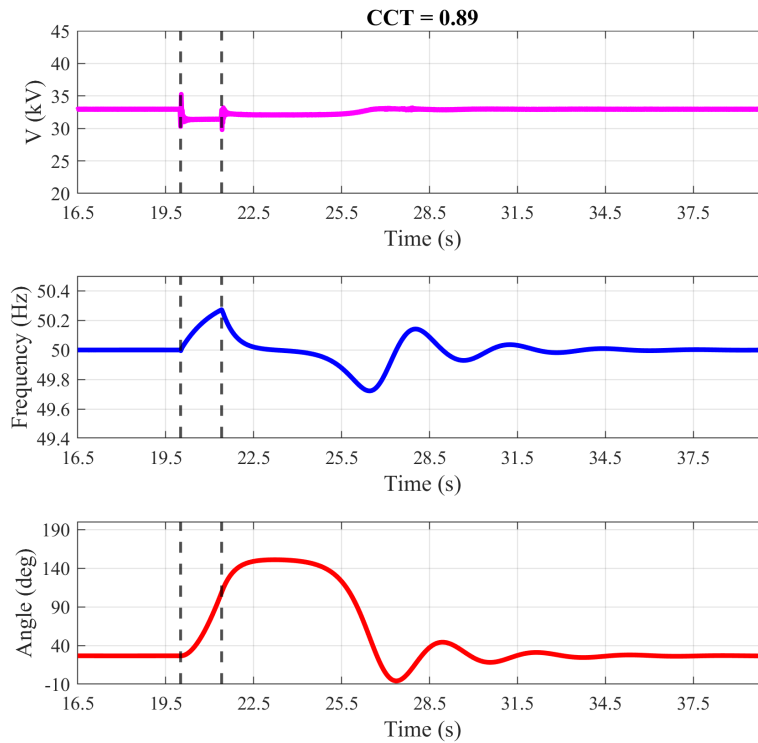


**Figure 22: Time domain results for the VSG with a three-phase fault at the grid**

However, with the developed method, these values can be determined quickly and efficiently without requiring iterative testing. Figure 22 presents the PSCAD simulation results, demonstrating a strong correlation between the CCT and CCA values obtained through PSCAD and those calculated using the proposed Lyapunov-based method. As shown in Table 8, the computed values align closely with the simulation results, validating the accuracy of the developed approach.

Beyond simply identifying CCT and CCA, the developed method provides additional insights that cannot be obtained using PSCAD alone. Specifically, this approach allows for the estimation of the time required for the system to return to stable operation under various fault scenarios, offering a more comprehensive understanding of system recovery dynamics. This capability enhances stability margin assessments and facilitates efficient tuning of control parameters, making the method highly valuable for IBR-dominated power system analysis.

#### Study the Impact of System Parameters:

The developed method not only enables efficient CCT and CCA estimation but also facilitates a comprehensive analysis of the impact of system parameters on TS. This capability provides deeper insights into how different control and system parameters influence stability, allowing for optimised parameter selection.

#### Impact of Inertia Coefficient:

*Table 7: CCT and time to reach SEP variation with the inertia coefficient*

$J$	CCT (s)	TIME TO REACH SEP (s)
$J$	1.3268	1.0167
$1.5J$	1.5317	1.0226

$0.5J$	1.0789	1.0087
--------	--------	--------

As presented in Table 7, an increase in the inertia coefficient results in a higher CCT, indicating that a system with greater inertia can withstand faults for a longer duration before losing stability. However, this increase in inertia also leads to a reduction in DOA, as illustrated in Figure 23. A smaller DOA implies a narrower stability margin, making the system more susceptible to disturbances if the fault-clearing conditions are not precisely maintained. These findings emphasise the importance of careful selection of inertia values, balancing fault tolerance and system recovery time to achieve optimal performance in VSG-based systems.

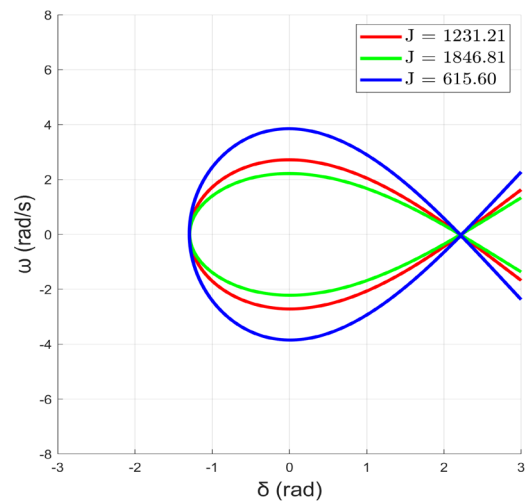


**Figure 23: Region of attraction variation with inertia coefficient**

Table 8 compares the CCT values obtained using the developed method with PSCAD simulation results for different inertia values. The results demonstrate a high degree of accuracy, with the developed method producing values closely matching those derived from PSCAD simulations. This further validates the effectiveness of the proposed Lyapunov-based approach in accurately capturing the impact of inertia on system stability while significantly reducing computational effort compared to traditional simulation-based techniques.

*Table 8: Comparison of CCT values obtained from time domain simulation and the developed method for different inertia coefficients*

$J$	CCT (s)	
	Developed method	PSCAD
$J$	1.33	1.40
$1.5J$	1.53	1.59
$0.5J$	1.08	1.15

**Impact of the Damping Coefficient:**

This case study examines the influence of the damping coefficient on CCT and DOA. As shown in Table 9, a decrease in the damping coefficient results in a reduction in CCT, indicating that lower damping reduces the system’s ability to withstand disturbances before instability occurs. Additionally, a lower damping



coefficient leads to a longer recovery time, causing the system to take more time to reach the SEP after a disturbance.

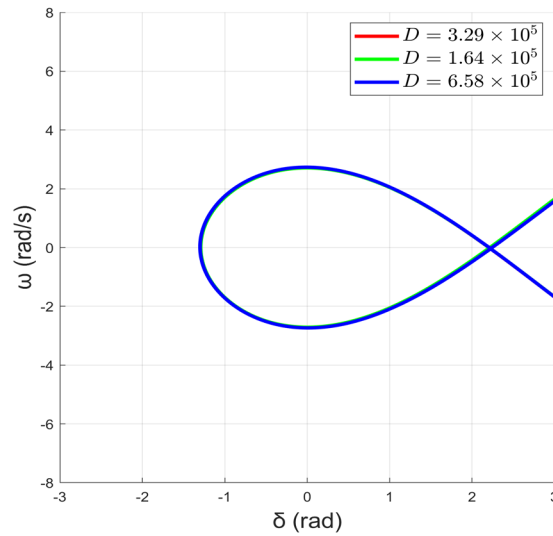


**Figure 24: Region of attraction variation with damping coefficient: VSG**

However, as illustrated in Figure 24, damping has no significant impact on the DOA. This suggests that while damping affects transient response characteristics, such as settling time and oscillation damping, it does not substantially alter the overall stability boundary of the system. These findings emphasise the importance of appropriate damping selection.

*Table 9: CCT and time to reach SEP variation with damping coefficient: VSG*

$D$	CCT (s)	TIME TO REACH SEP (s)
$D$	1.3268	1.0167
$0.5D$	1.1349	-
$2D$	1.8740	1.0077

#### Impact of Grid Strength:

Another significant advantage of the developed method is its ability to efficiently analyse the impact of grid strength on stability, an assessment that is typically challenging and time-consuming using PSCAD. As shown in Table 10, an increase in SCR results in a higher CCT, indicating that SCR enhances the system's ability to withstand disturbances for a longer duration before instability occurs. Additionally, with a higher SCR, the system reaches the SEP more quickly, demonstrating faster fault recovery. Furthermore, DOA also expands as SCR increases, as shown in Figure 25. This highlights the importance of grid strength in determining system large signal stability.

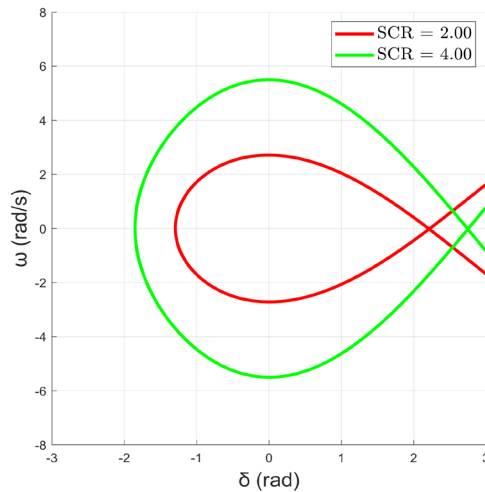


**Figure 25: Region of attraction variation with SCR**

*Table 10: CCT and time to reach SEP variation with SCR*

SCR	CCT (s)	TIME TO REACH SEP (s)
2	1.3268	1.0167
4	1.7966	1.0159

Key Findings: VSG Stability Analysis:

The developed method enables the determination of the DOA, providing a comprehensive stability assessment under various fault conditions. By evaluating whether the fault clearing point lies within the DOA, system stability can be effectively predicted. Additionally, this method facilitates the precise calculation of CCT, CCA, and the time required to reach a stable operating point significantly faster than conventional time-domain simulations.

*Table 11: Summary of key findings of VSG*

PARAMETER	EFFECT ON CCT	EFFECT ON DOA	EFFECT ON TIME TO STABILITY
↑Inertia	↑Increases	↓ Decreases	Longer
↑Damping	↑Increases	-	Shorter
↑SCR	↑Increases	↑Increases	Shorter

[Table 11](#) summarises the key relationships observed between system parameters and stability metrics using the developed method. The findings reveal that increasing inertia enhances CCT, allowing the system to tolerate faults for a longer duration. However, this results in a reduction in DOA and a longer stabilisation time, making parameter selection critical. For damping, an increase leads to improved stability by extending CCT, but it also reduces DOA while accelerating system recovery. Lastly, higher SCR values lead to an increase in both CCT and DOA. These insights are essential for tuning system parameters to optimise transient stability and enhance the resilience of VSG-based networks.

### Application to Droop-based Control:

The developed method can also be extended to analyse different grid-forming control strategies, including droop-based control. When inertia approaches zero, the controller exhibits droop-like behaviour, significantly altering the system's dynamic response. Using this method, it is possible to accurately determine the region of attraction for various control parameters and fault scenarios, enabling a more comprehensive stability assessment.

As illustrated in Figure 26, the system's dynamic behaviour during and after a fault differs notably from VSG-based control. Due to the absence of inertia, the system stabilises without oscillations, demonstrating a faster but less damped transient response. Additionally, as shown in Figure 27, the DOA for the droop-controlled system is larger compared to the VSG, suggesting a broader stability region.

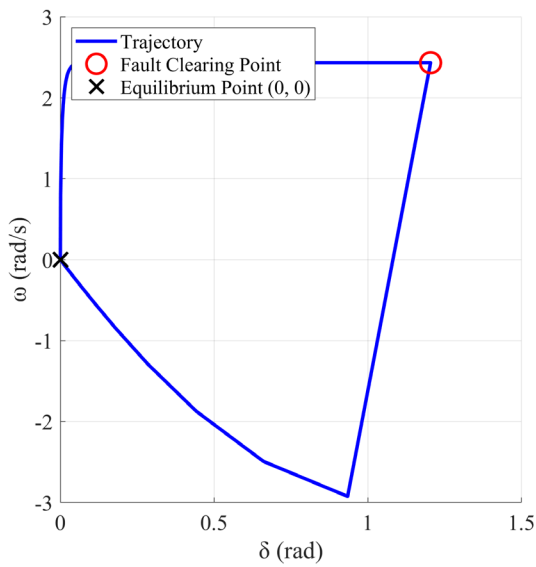


**Figure 26: Phase portrait dynamics of the stable case: droop**

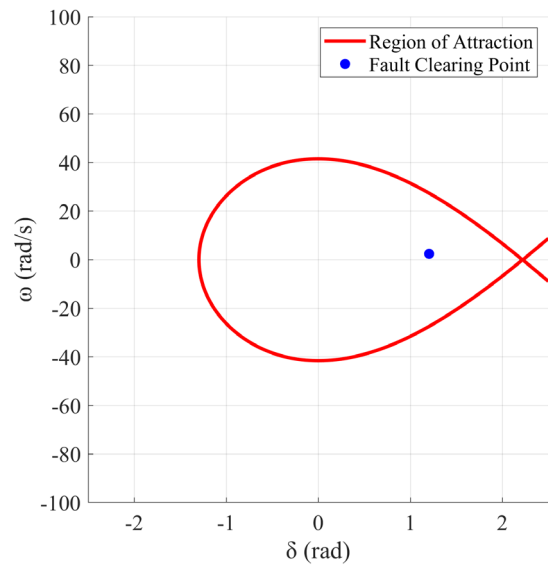


**Figure 27: Region of attraction with the stable case: droop**

### Validation with PSCAD Simulations:

The results presented in Figure 28, obtained from PSCAD simulations using the trial-and-error method, closely align with the calculated values derived from the developed method. This strong correlation further validates the accuracy and reliability of the proposed approach in assessing TS for droop-based control.

Similar to the VSG case, the developed method also enables the estimation of the time required to reach stable operation, a critical metric that cannot be directly obtained through conventional PSCAD simulations. This capability enhances the efficiency of stability assessments, allowing for a more systematic and computationally efficient evaluation of droop-controlled GFMI under various fault scenarios and parameter variations.

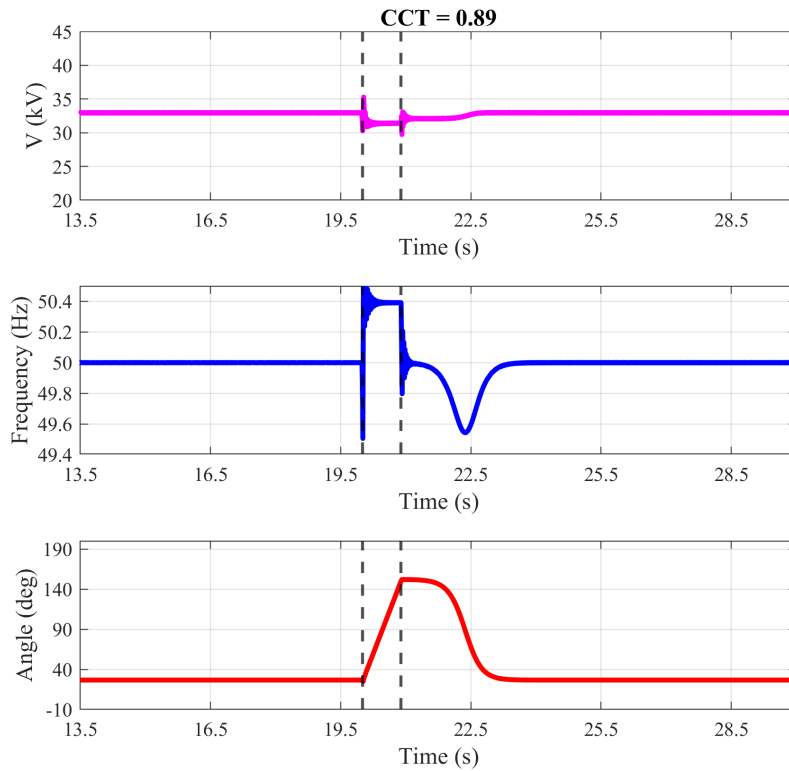


**Figure 28: Time domain results for the droop with a three-phase fault at the grid**

### Study the Impact of System Parameters:

#### Impact of the Damping Coefficient:

Similar to the VSG, the developed method enables a detailed analysis of how CCT and DOA vary with different system parameters in droop-based controllers. As shown in [Table 12](#) and [Figure 29](#), a decrease in the damping coefficient results in a reduction in both CCT and DOA, indicating a lower tolerance to disturbances and a narrower stability region.

Furthermore, as demonstrated in [Table 12](#), the developed method provides accurate CCT values for different parameter settings significantly faster than conventional PSCAD simulations, eliminating the need for trial-and-error testing. This efficiency makes the method highly valuable for grid-forming control optimisation, enabling the rapid tuning of droop controllers to enhance transient stability in inverter-dominated power systems.

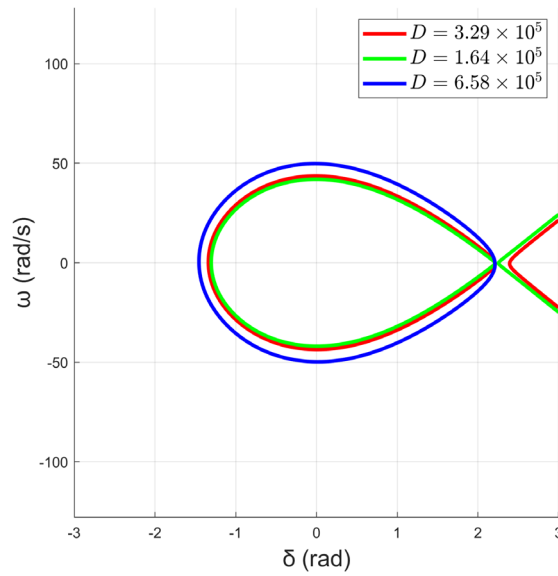


**Figure 29: Region of attraction variation with damping coefficient: droop**

The developed method provides an efficient and accurate approach for analysing the sensitivity of GFMI stability under varying control parameters and fault conditions. By systematically evaluating the impact of inertia, damping, SCR, and droop coefficients, key insights have been gained into their influence on CCT, DOA, and system recovery time. The ability to determine these stability metrics significantly faster than conventional PSCAD simulations enhances the feasibility of real-time stability assessments and control tuning. While the findings presented in this report demonstrate the method's robustness, further work is required to extend the approach to GFMI with limiters and refine the methodology for broader practical applications.

*Table 12: Comparison of CCT values obtained from time domain simulation and the developed method for different damping coefficients*

$D$	CCT (s)	
	Developed method	PSCAD
$D$	0.89	0.89
$0.5D$	0.43	0.45
$2D$	1.81	1.84

## 2.2.4. Impact of Prioritised Current Limiters on the Transient Stability

### Modelling of GFMI with PCL:

The prioritised current limiter (PCL) is a critical component in GFMI, providing essential protection against overcurrent conditions during severe grid faults. In [Section 2.2.3](#), a conventional Lyapunov function was employed to estimate the ROA, CCT, and CCA for VSG-based GFMI operating without a PCL. However, this methodology becomes inadequate when applied to GFMI equipped with PCL due to the switching behaviour introduced by the current-limiting mechanism. To accurately assess the transient stability of GFMI under such conditions, it is essential to understand the system's dynamic response to fault events in the presence of a PCL. This understanding serves as the foundation for developing a novel Lyapunov-based approach tailored to GFMI with PCL, enabling the estimation of the ROA. As a first step, it is necessary to derive the analytical expression for the quadrature-prioritised current limiter (q-PCL).

$$i_{q,sat}^* = \text{sign}(i_q^*) \min(|i_q^*|, I_m) \quad (19)$$

$$i_{d,sat}^* = \text{sign}(i_d^*) \min(|i_d^*|, \sqrt{I_m^2 - (i_{q,sat}^*)^2}) \quad (20)$$

where  $i_q^*$  and  $i_d^*$  represent the reference currents generated by the inner voltage loop.  $I_m$  denotes the maximum allowable current. In [\(20\)](#), it is shown that after prioritising the q-axis current, the PCL allocates any remaining current margin to the d-axis; if no margin remains, the d-axis current is set to zero. Similarly, the direct-prioritised current limiter (d-PCL) can be defined by swapping the priority: the d-axis current is prioritised first, and the q-axis is adjusted based on the remaining current capacity.

$$i_{d,sat}^* = \text{sign}(i_d^*) \min(|i_d^*|, I_m) \quad (21)$$

$$i_{q,sat}^* = \text{sign}(i_q^*) \min(|i_q^*|, \sqrt{I_m^2 - (i_{d,sat}^*)^2}) \quad (22)$$

Secondly, the transient model of the VSG-based GFMI with PCL should be derived as follows:

$$\frac{d}{dt} \delta = \omega \quad (23)$$

$$J \frac{d}{dt} \omega = -D\omega - (P(\delta) - P^*) \quad (24)$$

$$P(\delta) = P_{nm}(\delta) = \frac{k^2 V^*}{Z_g} \cos \delta_z - \frac{k V^* V_g}{Z_g} \cos (\delta + \delta_z), \quad \text{if } \sqrt{(i_d^*)^2 + (i_q^*)^2} \leq I_m \quad (25)$$

$$P(\delta) = P_{clm}(\delta) = V(\delta) I_m \cos (-\phi(\delta)), \quad \text{if } \sqrt{(i_d^*)^2 + (i_q^*)^2} > I_m \quad (26)$$

where  $\delta$  and  $\omega$  are the phase angle of the POC voltage and the angular speed deviation, respectively.  $J$  and  $D$  represent the inertia constant and the damping factor, respectively.  $P(\delta)$  and  $P^*$  denote the output power and reference power of the GFMI.  $V^*$  and  $V_g$  are the reference voltage of the GFMI and the grid voltage magnitude, respectively. The grid impedance is expressed as  $Z_g e^{j\delta_z}$ , and  $k$  is the transformer ratio. In [\(25\)](#)

and (26), the switching behaviour is characterised by two expressions of  $P(\delta)$  corresponding to two operating modes: normal mode (NM) and current-limited mode (CLM). In NM, the GFMI operates as a voltage source that sets the POC voltage  $V^* e^{j\delta}$ . In CLM, GFMI operates as a current source, injecting the maximum current  $I_m e^{j(\phi+\delta)}$ . Since  $\phi$  is unknown, it is derived using the power conservation principle between the primary and secondary sides of the transformer, as shown below.

$$P_{pri} = P_{sec} \quad (27)$$

$$\phi_{q-PCL} = \sin^{-1} \left( \frac{f(\delta)}{\sqrt{I_m^2 + B^2}} \right) + \tan^{-1} \left( \frac{B}{I_m} \right) \quad (28)$$

$$\phi_{d-PCL} = \pi - \sin^{-1} \left( \frac{f(\delta)}{\sqrt{I_m^2 + B^2}} \right) - \tan^{-1} \left( \frac{B}{I_m} \right) \quad (29)$$

where:

$$f(\delta) = -\frac{kV_g}{Z_g} \sin(\delta + \delta_z) - \frac{V_g}{k \cos \delta_z} \left( \frac{1}{\omega_0 C_f} - \frac{k^2}{Z_g} \sin \delta_z \right) \cos(\delta + \delta_z) \quad (30)$$

$$B = \frac{Z_g I_m}{k^2 \cos \delta_z} \left( \frac{1}{\omega_0 C_f} - \frac{k^2}{Z_g} \sin \delta_z \right) \quad (31)$$

Note that  $\omega_0$  is the fundamental angular speed and  $C_f$  is the filter capacitor of GFMI. Additionally, to guarantee the existence of a stable equilibrium point,  $\phi$  must exist. This condition leads to the following inequality:

$$-1 \leq \frac{f(\delta)}{\sqrt{I_m^2 + B^2}} \leq 1 \quad (32)$$

which, upon solving, yields  $\delta \in [\delta^{s,-}, \delta^{s,+}]$ . If the system's state exceeds this range, it becomes unstable.

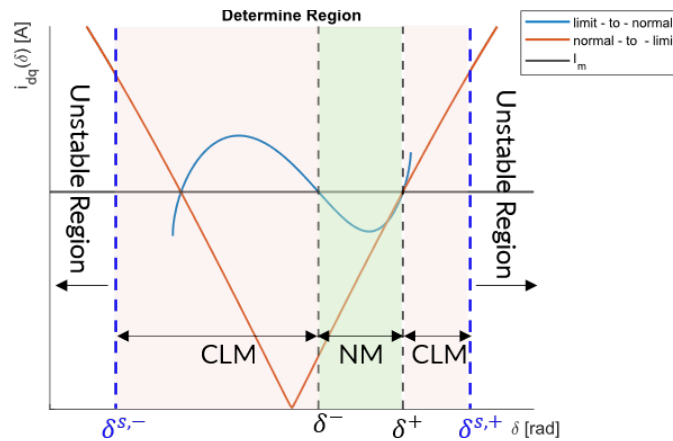


**Figure 30: The region of each operation mode: normal mode and current-limited mode**

Additionally, in (23)–(26), it is evident that the model is not a *pure* state-space model for the variables  $(\delta, \omega)$  due to the inequalities associated with  $i_d^*$  and  $i_q^*$ . Therefore, it is necessary to transform (23)–(26) into a state-space model for  $(\delta, \omega)$ . To achieve this, we consider the operational ranges for each mode in the GFMI with PCL. Figure 30 illustrates an example of the regions for each operating mode, including NM and CLM. If

$\delta^- \leq \delta \leq \delta^+$ , the NM is active. If  $\delta^{s,-} \leq \delta \leq \delta^{s,+}$  or  $\delta^{s,+} \leq \delta \leq \delta^{s,+}$ , the CLM is active. Consequently, (23)–(26) can now be transformed into a state-space model as follows:

$$\frac{d}{dt}\delta = \omega \quad (33)$$

$$J \frac{d}{dt}\omega = -D\omega - (P(\delta) - P^*) \quad (34)$$

$$P(\delta) = P_{nm}(\delta) = \frac{k^2 V^*}{Z_g} \cos \delta_z - \frac{k V^* V_g}{Z_g} \cos (\delta + \delta_z), \quad \text{if } \delta^- \leq \delta \leq \delta^+ \quad (35)$$

$$P(\delta) = P_{clm}(\delta) = V(\delta) I_m \cos (-\phi(\delta)), \quad \text{if } \delta^{s,-} \leq \delta \leq \delta^{s,+} \text{ or } \delta^+ \leq \delta \leq \delta^{s,+} \quad (36)$$

### ROA and CCT Estimation:

Based on the state-space model of  $(\delta, \omega)$ , a Lyapunov-based method can be developed to estimate the ROA. First, Lyapunov functions for both NM and CLM are derived as follows:

$$V_{nm}(\delta, \omega) = \frac{1}{2} J \omega^2 + \int_0^\delta P_{nm}(\delta) - P^* d\delta \quad (37)$$

$$V_{clm}(\delta, \omega) = \frac{1}{2} J \omega^2 + \int_0^\delta P_{clm}(\delta) - P^* d\delta \quad (38)$$

As discussed in Section 2.2.3, it is important to note that  $V_{nm}(\delta, \omega)$  and  $V_{clm}(\delta, \omega)$  are valid Lyapunov functions within their respective regions. Specifically,  $V_{nm} > 0$  and  $d/dt(V_{nm}) < 0$  for  $\delta^- \leq \delta \leq \delta^+$ , while  $V_{clm} > 0$  and  $d/dt(V_{clm}) < 0$  for  $\delta^{s,-} \leq \delta \leq \delta^{s,+}$  or  $\delta^{s,+} \leq \delta \leq \delta^{s,+}$ . Using these Lyapunov functions, the ROA for each mode can be derived by identifying the lowest unstable equilibrium point, as discussed in Section 2.2.3. Figure 31 illustrates the process of constructing the estimated ROA for (33)–(36). First, the ROA for normal mode is built, shown by the black solid closed curve. Then, the ROA for the current-limited mode is constructed, depicted by the blue solid closed curve. Finally, the estimated ROA for (33)–(36) is the overlapping region of the blue and black curves.

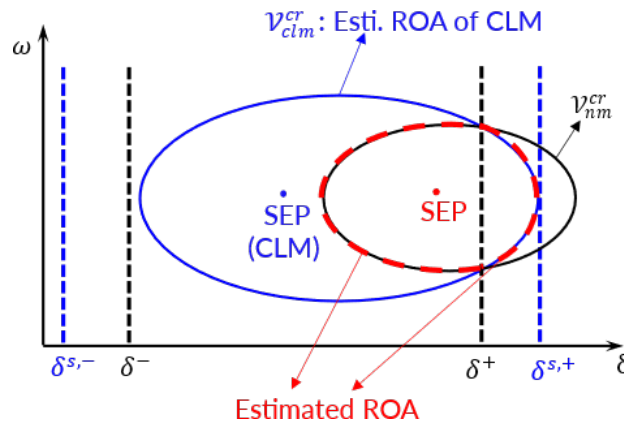


**Figure 31: The region of each operation mode: normal mode and current-limited mode**



## Verification of the Proposed Method:

This section verifies the proposed method through an example with the active power reference  $P^* = 0.6$  pu. The estimated CCT for the GFMI with q-PCL is shown in Figure 32, where a CCT of 0.52s is obtained. The exact CCT, obtained by the switching electromagnetic-transient model in PSCAD, is 0.56s, as shown in Figure 33. Therefore, the error between the estimated and exact values is 7.14%.

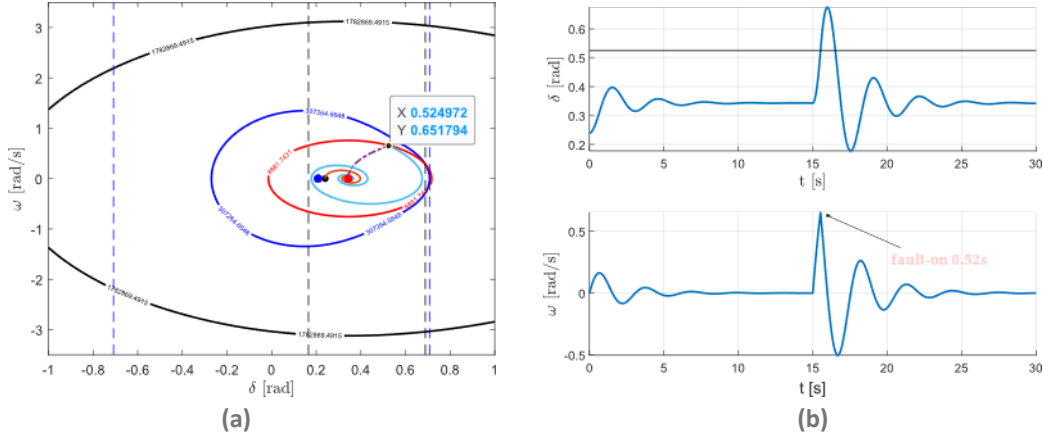


**Figure 32:** The estimated ROA is shown by the red closed curve, which provides the estimated CCT of 0.52s

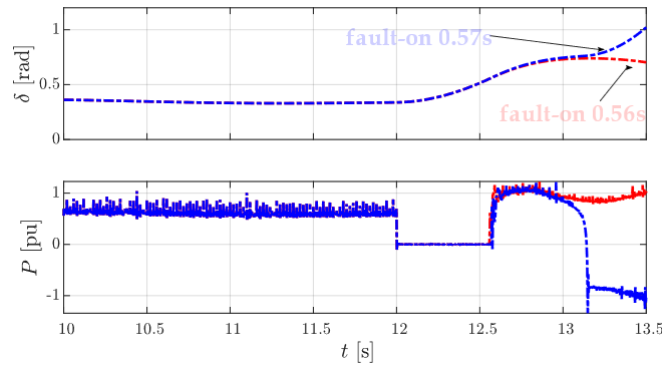


**Figure 33:** The exact CCT from PSCAD is 0.56s

## Sensitivity Analysis:

### Impact of Changing Inertia Constant $J$ (Low-SCR Grid):

*Table 13: Comparison of CCT values when changing the inertia constant in GFMI with q-PCL and d-PCL*

$J$	CCT (s)			
	Exact CCT (q-PCL) (s)	Estimated CCT (q-PCL) (s)	Exact CCT (d-PCL) (s)	Estimated CCT (d-PCL) (s)
$0.5J$	0.22	0.19	0.04	0.03
$J$	0.28	0.26	0.06	0.04
$1.5J$	0.33	0.31	0.07	0.05

Table 13 presents the estimated CCT and the exact CCT for varying inertia values. Notably, as the inertia constant increases, the CCT also increases. This trend is consistent with the CCT observed in the GFMI without PCL.

#### Impact of Changing the Damping Factor $D$ (Low-SCR Grid)

Table 14 illustrates the variation of the CCT with increasing damping factor. Notably, as the damping factor increases, the CCT also increases. This trend is consistent with the CCT observed in the GFMI without PCL.

Table 14: Comparison of CCT values when changing the damping factor in GFMI with q-PCL and d-PCL

$D$	CCT (s)			
	Exact CCT (q-PCL) (s)	Estimated CCT (q-PCL) (s)	Exact CCT (d-PCL) (s)	Estimated CCT (d-PCL) (s)
$0.5D$	0.25	0.22	0.04	0.04
$D$	0.28	0.26	0.06	0.04
$1.5D$	0.33	0.28	0.06	0.04

Additionally, it is evident that the proposed method yields a conservative value for the CCT, reflecting its accuracy.

#### Impact of Changing the Power Reference $P^*$ (Low-SCR Grid)

Table 15: Comparison of CCT values when changing the power reference in GFMI with q-PCL and d-PCL

POWER REFERENCE ( $P^*$ )	CCT (s)			
	Exact CCT (q-PCL) (s)	Estimated CCT (q-PCL) (s)	Exact CCT (d-PCL) (s)	Estimated CCT (d-PCL) (s)
$P^* = 0.5pu$	0.74	0.70	0.64	0.39
$P^* = 0.6pu$	0.56	0.52	0.39	0.24
$P^* = 0.7pu$	0.41	0.38	0.25	0.15

Table 15 shows that the CCT decreases as the GFMI injects more active power into the system. Furthermore, from Tables 13–15, it can be observed that, in a low-SCR grid, the q-PCL provides a higher CCT compared to the d-PCL.

#### Impact of Changing the Maximum Current (Low-SCR Grid)

It is important to examine the relationship between the maximum current ( $I_m$ ) and the CCT of the GFMI with q-PCL. This relationship helps operators select the appropriate maximum current to achieve the desired CCT. Figure 34 illustrates the non-linear relationship between  $I_m$  and CCT, showing that as  $I_m$  increases, the CCT also increases.

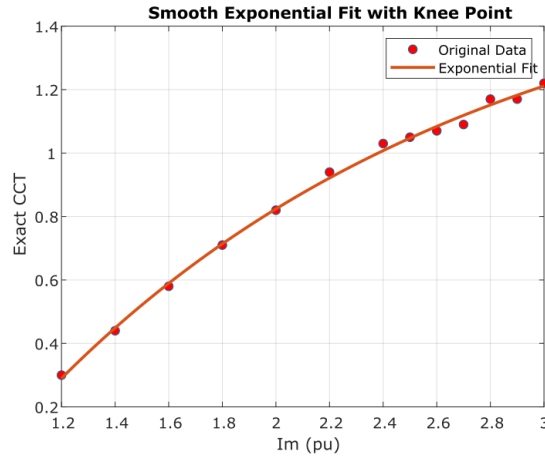


**Figure 34: The nonlinear relationship between  $I_m$  and CCT**

#### Impact of Changing SCR (Low and High-SCR Grid)

It is also important to consider the impact of SCR on the performance of GFMI with q-PCL and d-PCL. GFMI without PCL provides a larger ROA and a higher CCT, while the presence of PCL reduces the ROA area, resulting in a lower CCT. For a low-SCR grid, GFMI with q-PCL offers a higher CCT compared to GFMI with d-PCL. However, as SCR increases, GFMI with d-PCL provides a higher CCT than GFMI with q-PCL, indicating better transient stability in these cases. Furthermore, in a low-SCR grid, the grid's impact on GFMI is smaller compared to a high-SCR grid, leading to a narrower voltage loop bandwidth to ensure system stability. In this scenario, the feed-forward term in the voltage loop may be set to less than 1 to enhance stability (see [Section 2.4.5: Voltage Loop Control](#)). Conversely, in a high-SCR grid, where the grid's impact is more significant, the voltage loop bandwidth should be wider to maintain stability, with the feed-forward term also set to less than 1.

*Table 16: CCT of GFMI without and with PCL in a low-SCR grid ( $P^* = 0.8$  pu)*

SCR	CCT (s)					
	Exact CCT (without PCL) (s)	Esti. CCT (without PCL) (s)	Exact CCT (q-PCL) (s)	Esti. CCT (q-PCL) (s)	Exact CCT (d-PCL) (s)	Esti. CCT (d-PCL) (s)
4	1.9	1.6	0.15	0.12	0.18	0.14
2	1.5	1.3	0.27	0.23	0.13	0.05

[Table 16](#) shows that, compared to GFMI without PCL, the CCT of GFMI with PCL is significantly lower. For SCR = 2, GFMI with q-PCL exhibits a higher CCT than GFMI with d-PCL, indicating better transient stability in this case. However, when SCR = 4, the CCT of GFMI with d-PCL exceeds that of GFMI with q-PCL. This trend becomes more apparent as SCR increases, as shown in [Table 17](#).

*Table 17: CCT of GFMI without and with PCL in a high-SCR grid ( $P^* = 0.8$  pu)*

SCR	CCT (s)		
	Exact CCT (without PCL) (s)	Exact CCT (q-PCL) (s)	Exact CCT (d-PCL) (s)
20	1.2	0.01	0.10
15	1.3	0.01	0.20

Table 17 shows that as SCR increases, the CCT decreases. The results indicate that GFMI without PCL offers better transient stability with a higher CCT. Furthermore, the CCT of GFMI with q-PCL is lower than that of GFMI with d-PCL, suggesting that GFMI with d-PCL has higher transient stability margin compared to GFMI with q-PCL.

### 2.2.5. Critical Learnings and Insights

The sensitivity analysis conducted in Task 2 provides key insights into how different system parameters and fault profiles influence the large-signal stability of GFMI-dominated grids. This research integrates a broader range of control parameters and grid conditions, allowing for a more comprehensive assessment of stability margins. The main findings include:

- Existing large-signal stability assessment techniques, such as energy function-based approaches, phase portrait analysis, and Lyapunov methods, have been primarily applied to SMIB models, limiting their applicability to multi-IBR networks. Most conventional studies neglect inner control loop dynamics and network interactions, which are crucial for accurately capturing the stability behaviour of GFMI.
- Lyapunov-based methods were identified as the most suitable approach for obtaining CCT and DOA, as they provide a systematic and scalable framework for evaluating large-signal stability.
- Inner control loop parameters (current and voltage controllers) have minimal direct impact on CCT but influence fault response and post-fault recovery dynamics. The reactive power controller loop parameters did not significantly affect stability margins, suggesting that other tuning mechanisms are more effective in enhancing stability.
- Increasing inertia improves large-signal stability by allowing the system to withstand disturbances for a longer duration. However, higher inertia leads to a reduced DOA, making the system more susceptible to prolonged disturbances.
- A higher damping coefficient increases CCT and improves system recovery, effectively reducing oscillations after a fault. However, damping has a negligible impact on the DOA, indicating that while it enhances system recovery, it does not expand the large signal stability region.
- A higher SCR significantly enhances large-signal stability, as both CCT and DOA increase. A stronger grid allows the system to sustain larger disturbances for a longer duration and recover more efficiently.
- The sensitivity analysis approach developed in Stage 4 significantly improves computational efficiency by reducing trial-and-error simulations in PSCAD. By employing a systematic parameter variation framework, the method provides precise stability assessments, significantly reducing analysis time while maintaining high accuracy.

These insights contribute to a deeper understanding of GFMI behaviour under varying conditions, aiding in the development of refined control strategies and operational guidelines to improve grid resilience. Future work will focus on extending this sensitivity analysis to larger, multi-IBR systems, integrating real-world grid scenarios, and validating findings through hardware-in-the-loop testing.

## 2.3. Task 3: Large Signal Stability Analysis of Multi IBR System

### 2.3.1. Expand the Developed Large-Signal Stability Analysis to Include Systems with Multiple IBRs

The developed large-signal stability analysis is extended to multi-IBR systems to evaluate the dynamic interactions and stability margins in networks with multiple GFMI. Unlike single-IBR systems, where stability is influenced primarily by local inverter dynamics and grid conditions, multi-IBR networks introduce complex interactions between multiple grid-forming inverters. These interactions can significantly impact large signal stability, necessitating a more comprehensive analysis approach.

To achieve this, the developed Lyapunov-based method is applied to assess CCT and transient energy margins for systems containing multiple IBR clusters. The extended model incorporates coupling effects between IBRs, considering factors such as:

- Control parameter variations across different inverters,
- Fault propagation effects and their influence on multiple IBR stability, and
- Impact of network topology.

By integrating these factors, the stability assessment framework enables the identification of weak points in multi-IBR systems and provides guidelines for optimal inverter placement and tuning. Furthermore, by leveraging Lyapunov's direct method, the CCT of the network can be determined efficiently, allowing for a more accurate prediction of network-wide transient behaviour. These advancements allow the proposed method to serve as a powerful tool for assessing multi-IBR system stability, improving fault ride-through capability, and guiding control strategies for future IBR-dominated grids.

#### Methodology

Consider a  $k$ -bus system comprising  $n - 1$  GFMI, as illustrated in [Figure 35](#). Using the Kron reduction method [24], the system is reduced to an equivalent network that includes only the inverter buses and the slack bus. The swing equation for the  $i$ -th inverter in the reduced system is expressed as:

$$J_i \omega_0 \frac{d^2 \delta_i}{dt^2} + D_i \frac{d\delta_i}{dt} = P_{ref,i} - E_i^2 G_{ii} - E_i \sum_{j=1, j \neq i}^{n-1} E_j \left( G_{ij} \cos(\delta_i - \delta_j) + B_{ij} \sin(\delta_i - \delta_j) \right) - E_i E_n (G_{in} \cos \delta_i + B_{in} \sin \delta_i) \quad (39)$$

Here,  $G_{ij} + jB_{ij} = \frac{1}{Z_{ij} \angle \theta_{ij}}$  represents the short-circuit transfer admittance between the  $i$ -th and  $j$ -th inverters, which are obtained using the Kron reduction method.  $J_i$ ,  $D_i$ , and  $P_{ref,i}$  represent the inertia coefficient, the damping coefficient, and the power reference of each inverter, respectively. The  $n$ -th bus, which is connected to the grid, is considered the reference bus, and all angle measurements are taken relative to this bus.

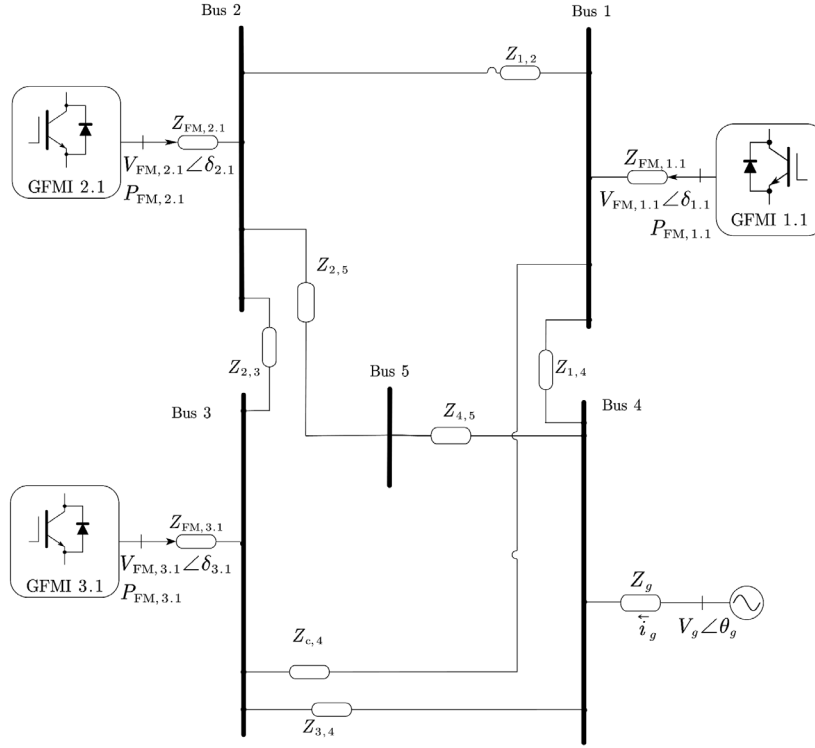


**Figure 35:  $n - 1$  inverter system with slack bus**

Assuming zero transfer conductance, the swing equation simplifies to:

$$J_i \omega_0 \frac{d^2 \delta_i}{dt^2} + D_i \frac{d\delta_i}{dt} = P_{ref,i} - E_i \sum_{j=1, j \neq i}^n E_j B_{ij} \sin(\delta_i - \delta_j) - E_i E_n B_{in} \sin \delta_i \quad (40)$$

To facilitate stability analysis, the equilibrium points (EPs) are calculated using the following equation:

$$P_{ref,i} - E_i \sum_{j=1, j \neq i}^{n-1} E_j B_{ij} \sin(\delta_i^s - \delta_j^s) - E_i E_n B_{in} \sin \delta_i^s = 0 \quad (41)$$

In this study, the Newton-Raphson (NR) method is employed to solve the nonlinear system of equations, achieving rapid convergence regardless of the number of equations involved. The justification for using the NR method lies in the similarity of these equations to traditional load flow problems, for which the NR method is well established and highly effective. For the calculation of SEPs, initial conditions are set close to 0 radians, while for UEPs, initial conditions are provided near  $\pi$  radians.

By considering  $n$ -th bus as the reference bus, the state vectors as defined as:

$$\delta_i = \Delta \omega_i$$

$$\Delta \omega_i = D_i \Delta \omega_i = P_{ref,i} - E_i \sum_{j=1}^n E_j B_{ij} \sin(\delta_i - \delta_j) - E_i E_n B_{in} \sin \delta_i \quad (42)$$

Applying forward numerical integration, the Lyapunov function for a damped system is derived as:

$$\begin{aligned}
V = & \frac{1}{2}(J_T)\omega_0 \sum_{i=1}^{n-1} \Delta\omega_i^2 - (J_T)\omega_0 \sum_{i=1}^{n-1} \frac{P_{mi}}{J_i\omega_0}(\delta_i - \delta_i^s) \\
& - \sum_{i=1}^{n-2} \sum_{j=i+1}^{n-1} E_j B_{ij} (\cos \delta_{ij} - \cos \delta_{ij}^s) \\
& - E_n J_T \omega_0 \sum_{i=1}^{n-1} \frac{E_i B_{in}}{J_i\omega_0} (\cos \delta_i - \cos \delta_i^s) \\
& - (J_T)\omega_0 \sum_{i=1}^{n-1} \frac{D_i \Delta\omega_i (\delta_i - \delta_i^s) + \frac{D_i^2 (\delta_i - \delta_i^s)^2}{2J_i\omega_0}}{J_i\omega_0}
\end{aligned} \tag{43}$$

Here  $J_T = \sum_{i=1}^{n-1} J_i$  represents the total inertia of the system, and  $\delta_{ij} = \delta_i - \delta_j$  denotes the angle difference between inverters  $i$  and  $j$ . This formulation enables an efficient assessment of multi-IBR system stability, providing insights into large-signal transient behaviour, system interactions, and stability boundaries such as the CCT of the network.

The calculation of the CCT for a larger system follows a structured approach, similar to the method outlined in [Section 2.2.3](#). The process begins with determining the admittance matrix of the post-fault system, simplifying the network by reducing it to its inverter PCC buses while preserving the influence of external buses. This reduction facilitates a more efficient stability analysis by focusing on the key components governing system dynamics.

Next, the SEP and UEP of the post-fault system are identified using the NR method, which is applied within the reference frame to compute these equilibrium points precisely. Once these values are determined, they are substituted into the Lyapunov function, allowing for the calculation of the CCT.

By evaluating the Lyapunov function at the UEP, the CCT is determined, providing a quantitative measure of the system's transient stability margin. This method offers a systematic and accurate approach for stability assessment, enabling effective analysis of the system under severe fault conditions such as bolted faults and significant voltage sags as well as under various control parameter settings.

### 2.3.2. Use the Developed Method As a Tool and Calculate the CCT of the System

To validate the developed method, a 5-bus system comprising three GFMI connected to the slack bus is considered, as illustrated in [Figure 36](#). The detailed system parameters are provided in [Apx Table C. 1](#). A PSCAD model was developed for this network, and a three-phase bolted fault was applied at the slack bus. Using a trial-and-error approach, the CCT of the system was determined through time-domain simulations. In contrast, the developed method calculates the CCT directly and efficiently by using only the system parameters as inputs, significantly reducing the time required for analysis. The following section presents the results obtained from both approaches, highlighting the accuracy and efficiency of the developed method.

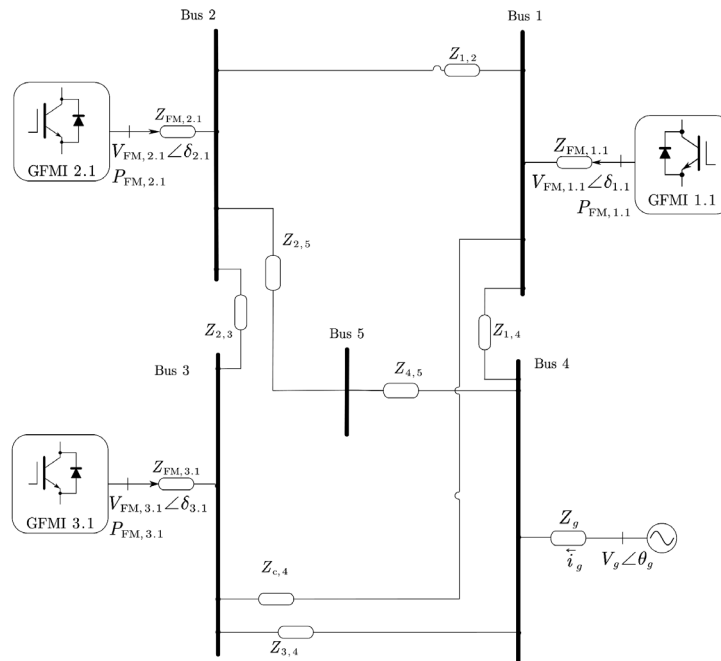


**Figure 36: Five-bus system with three inverters**

Using the developed method, the impedance matrix was calculated by neglecting transfer conductance, thereby simplifying the system model for stability assessment. The NR method was then applied to determine the SEP and UEP angles, as summarised in Table 18. The results demonstrate that the estimated equilibrium point angles closely match those obtained from PSCAD plots, validating the accuracy of the method. Finally, by substituting the identified equilibrium points into the Lyapunov function in (43) and performing forward numerical integration, the system's energy evolution was obtained. By comparing the Lyapunov function value with the system's critical energy threshold, as illustrated in Figure 37, the CCT of the system was calculated as 1.21 seconds. This result is in close agreement with the value obtained through PSCAD simulations, confirming the reliability and accuracy of the developed method for transient stability analysis.

*Table 18: SEP and UEP angle of each inverter reference to the 4th inverter*

INVERTER	PSCAD - EP (DEGREES)	LF - EP (DEGREES)	PERCENTAGE ERROR
<b>SEP</b>			
1	29.2348	29.5081	0.935
2	29.4219	29.9001	1.625
3	29.6866	29.6960	0.032
<b>UEP</b>			
1	150.3952	150.0727	0.214
2	151.2933	150.6632	0.416
3	152.7396	150.4118	1.524
<b>CCT</b>	<b>1.22</b>	<b>1.21</b>	<b>0.4818</b>



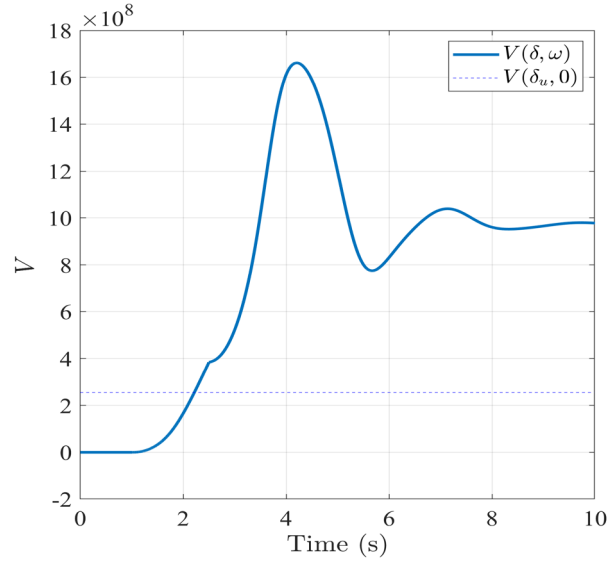


**Figure 37: Energy function value variation during the fault**

### 2.3.3. Effectiveness Evaluation of the Proposed Methodology

#### Impact of Network Topology Variation:

In this study, the network shown in Figure 36 is considered, and the developed method is applied to calculate the CCT for each network configuration. In Table 19, the variable  $Z_{k,h}$  represents the connection between two buses, where a value of 0 indicates no connection and a value of 1 signifies the presence of a connection. By varying the network configuration, the resulting CCT values change accordingly, allowing for the analysis of CCT variations under different scenarios, such as line outages and fault events.

*Table 19: Comparison of CCT for different network arrangements*

TEST	$Z_{1,2}$	$Z_{1,3}$	$Z_{1,4}$	$Z_{2,3}$	$Z_{2,5}$	$Z_{3,4}$	$Z_{4,5}$	CCT
1	1	1	1	1	1	1	1	1.214
2	0	1	1	1	1	1	1	1.203
3	1	0	1	1	1	1	1	1.213
4	0	1	1	0	1	1	1	1.206
5	1	1	1	0	1	1	1	1.217
6	1	1	0	1	1	1	1	0.747

In Test 1, where all network connections are intact, the system achieves a CCT of 1.21 seconds. When the connection between Inverters 1 and 2 is removed or fails, the CCT slightly decreases to 1.20 seconds. Interestingly, removing the connection between Inverters 2 and 3 results in an increase in the CCT, indicating improved stability under this configuration. However, when the direct connection from Inverter 1

to the grid is removed, as shown in Test 6, the CCT decreases significantly, reflecting a substantial reduction in system stability.

These results demonstrate that the developed tool can effectively calculate the CCT for any network comprising GFMI and help identify the most stable network configuration, which corresponds to the highest CCT. Additionally, the tool provides valuable insights into how different fault scenarios impact system stability, enabling the evaluation of critical contingencies and supporting the design of more resilient network configurations.

**Impact of Inertia Coefficient on Stability Index:**

The impact of inertia on the CCT was analysed by varying the virtual inertia constant of GFMI 1 ( $J_1$ ) while keeping all other system parameters constant, as specified in [Apx Table C. 1](#). As presented in [Table 20](#) (left), increasing the inertia coefficient of GFMI 1 leads to corresponding changes in the CCT. Using the developed tool, it is possible to assess how reductions in inertia provision from specific power plants affect system stability and to determine appropriate mitigation strategies.

Additionally, [Table 20](#) (right) illustrates that as the total virtual inertia of the system increases, the CCT also increases, indicating improved transient stability. Conversely, a reduction in total virtual inertia leads to a lower CCT, increasing the risk of system instability under fault conditions. These results clearly demonstrate that higher inertia improves the system’s ability to withstand disturbances by extending the allowable fault-clearing time and providing greater damping during transient events.

However, while increased inertia enhances stability, excessive inertia may negatively impact the system’s dynamic response by slowing the rate of frequency recovery and voltage restoration after disturbances. This underscores the importance of optimally tuning inertia parameters to achieve a balanced trade-off between stability margins and system responsiveness in multi-GFMI networks.

The developed tool enables network planners and operators to quantitatively assess this trade-off, facilitating informed decisions regarding inertia allocation and virtual inertia controller settings. These insights are particularly critical for weak grid regions and renewable energy zones, where stability challenges are more pronounced due to low system strength and high penetration of inverter-based resources.

*Table 20: CCT variation with inertia coefficient of GFMI 1*

INERTIA	CCT	INERTIA	CCT
$J_1$	1.214	$J_T$	1.214
$2J_1$	1.244	$2J_T$	1.087
$0.5J_1$	1.273	$0.5J_T$	1.460

**Impact of  $P_{ref}$  on Stability Index:**

*Table 21: CCT variation with  $P_{ref}$  of GFMI 1*

$P_{ref}$	CCT
$P_{ref,1}$	1.214
$2P_{ref,1}$	0.713

$0.5P_{ref,1}$	1.5950
----------------	--------

The effect of power reference on the CCT was analysed by varying the power reference of GFMI 1, while keeping all other system parameters unchanged. As shown in Table 21, an increase in  $P_{ref,1}$  results in a decrease in the CCT, indicating a reduction in transient stability. This trend indicates that higher active power dispatch levels reduce the system's ability to withstand disturbances, as more of the inverter's capacity is committed to meeting active power demands, leaving less headroom to provide critical dynamic support during fault events. In contrast, operating GFMI's with lower active power references enhances their capability to respond effectively to disturbances, resulting in higher CCT values and improved transient stability.

These findings highlight the need for careful consideration when setting  $P_{ref}$  values in grid-forming inverters, particularly in weak grid regions. Dynamic adjustment of power references, especially during high-risk operating conditions, can serve as an effective stability enhancement strategy. Additionally, these results can guide the development of control strategies that balance power delivery with system stability objectives, ensuring resilient operation under both normal and contingency scenarios.

#### Impact of Line Impedances on Stability Index:

The effect of line impedance on the CCT was analysed by varying the impedance between Buses 1 and 4 ( $Z_{1,4}$ ), while keeping all other system parameters unchanged. As shown in Table 22, an increase in  $Z_{1,4}$  results in a decrease in the CCT, indicating a reduction in transient stability. Specifically, when  $Z_{1,4}$  is doubled, the CCT decreases from 1.214 seconds to 1.075 seconds, highlighting increased system vulnerability. Conversely, reducing  $Z_{1,4}$  by half improves the CCT to 1.350 seconds, demonstrating enhanced stability.

Table 22: CCT variation with line impedance

$Z$	CCT
$Z_{1,4}$	1.214
$2Z_{1,4}$	1.075
$0.5Z_{1,4}$	1.350

These results show that variations in line impedance, such as those caused by faults or outages in a double-circuit transmission system, have a direct and measurable impact on system stability. Using the developed tool, operators can quickly assess the consequences of such events and plan appropriate mitigation actions. While there is no explicit formula linking impedance and CCT, the tool facilitates this rapid assessment through simulation-based analysis of different fault scenarios.

These findings underscore the critical importance of carefully managing line impedances within the network to preserve transient stability. Transmission planning should consider not only the steady-state performance but also the dynamic response of the system under fault conditions. Strategic placement of grid-forming inverters, reinforcement of key transmission corridors, and the use of adaptive protection schemes can help mitigate the adverse effects of increased line impedances, ensuring the network remains stable and resilient against large disturbances.

## Summary

Task 3 successfully completed the extension of large-signal stability analysis to multi-IBR systems, providing a robust framework to assess transient stability margins and dynamic interactions in networks with multiple GFMI. The developed Lyapunov-based method was effectively applied to calculate CCT, enabling systematic stability assessments under a wide range of network configurations and control settings.

Key achievements of Task 3 include:

- Development and validation of a computationally efficient method capable of accurately estimating CCT values, with close agreement to detailed PSCAD simulations.
- Comprehensive evaluation of network topology impacts, identifying the most stable configurations under varying fault conditions.
- Sensitivity analyses quantifying the influence of inertia coefficients, power references, and line impedances on system stability margins.
- Demonstration of the method's practical application for pre-installation studies of new power plants, inverter control tuning, and stability improvement strategies in weak-grid scenarios.

The developed framework offers valuable guidance for power system planners and operators, enabling optimised inverter placement, control parameter tuning, and network design decisions to enhance system stability and resilience in future high-renewable energy environments.

### 2.3.4. Critical Learnings and Insights

Task 3 extends the large-signal stability analysis to multi-IBR systems, addressing the complex interactions between multiple GFMI. The findings so far provide important insights into system-wide stability dynamics.

- **Validation of Lyapunov-Based Method for Multi-IBR Systems:** The developed method has been validated for complex multi-IBR networks, confirming its effectiveness in accurately calculating the CCT. This provides a faster and reliable alternative to time-consuming electromagnetic transient (EMT) simulations.
- **Significant Impact of Control Parameters on Stability:** Inertia, damping, and power reference settings of GFMI have a direct and measurable influence on CCT. Proper tuning of these parameters is essential to enhance system resilience while maintaining dynamic performance.
- **Network Topology Strongly Influences Stability:** The studies confirmed that network arrangements have a significant impact on CCT, with certain weakly connected topologies increasing system vulnerability. The developed method effectively identifies the most stable network configurations, enabling informed decisions for enhancing grid stability.
- **Line Impedance Variations Affect Stability Margins:** Variations in line impedances, either through network design or fault events, significantly affect CCT and overall stability. The tool enables rapid evaluation of such scenarios, assisting in contingency planning and network reinforcement strategies.
- **Need for Optimal Balance Between Stability and Dynamic Response:** While increasing inertia improves transient stability, excessive inertia can negatively affect the system's dynamic response. The tool supports achieving an optimal balance by enabling detailed sensitivity studies.

Task 3 outcomes have established a strong foundation for practical application in future grid planning and operational decision-making, supporting Australia's renewable energy transition and enhancing grid security in high-IBR environments.

## 2.4. Task 4: Development of Tuning and Design Guidelines for IBRs

Building upon the findings and methodologies established in the previous tasks, Task 4 focuses on developing practical tuning and design guidelines to enhance the stability and operational performance of IBR-dominated grids under diverse network conditions. The key objective is to synthesise insights from earlier analyses and translate them into actionable recommendations for industry implementation.

A critical aspect of this task involves integrating the Lyapunov-based stability analysis and sensitivity studies conducted in Tasks 2 and 3. This process leverages insights into key parameters such as droop coefficients, inertia constants, and fault response behaviours, enabling the formulation of generalised tuning strategies for grid-forming inverters. These strategies are designed to ensure both steady-state performance and transient stability, allowing for robust operation across varying grid conditions.

### 2.4.1. Development of Practical Tuning and Design Guidelines for Grid-forming IBRs

Currently, grid-forming capabilities have been successfully implemented in Battery Energy Storage Systems (BESSs), enabling these systems to support grid stability, regulate voltage and frequency, and enhance overall network resilience. As the penetration of renewable energy sources continues to increase, the role of grid-forming BESS becomes increasingly critical for ensuring the stability and reliability of modern power systems.

The guidelines presented herein focus exclusively on the implementation and operational aspects of grid-forming BESS, outlining control strategies, stability considerations, and best practices for integration. These guidelines aim to support the effective deployment of BESS technologies in grid-forming roles and to promote robust and resilient power system operation in high-renewable scenarios.

### 2.4.2. AEMO Guidance on Grid-Forming BESS Integration in the NEM

In December 2022, the AEMO published a fact sheet titled “Grid-Forming BESS Connections.” This document provides guidance on the connection of standalone BESS equipped with grid-forming inverters to the NEM. Specifically, it outlines the requirements and procedures for compliance with Rule 5.3 of the National Electricity Rules (NER) as of December 2022.

As highlighted in this fact sheet, grid-forming inverters generate their own internal voltage waveform and can synchronise with the grid or operate independently and unlike traditional grid-following inverters, grid-forming inverters can support system stability by providing inertia and system strength. The connection and registration processes for grid-forming BESS in the NEM are similar to those for grid-following BESS, but additional technical considerations apply.

Grid-forming inverters have unique response characteristics compared to grid-following inverters, which require careful performance tuning. These inverters can provide system strength support and inertia, but improper tuning may cause adverse system effects. Tuning trade-offs must be considered, as grid-forming inverters respond differently to faults, frequency disturbances, and voltage fluctuations. It is essential to ensure grid-forming BESS meets access standards without negatively impacting the power system.

### 2.4.3. Specific Requirements for GFM BESS According to NER Schedule 5.2

While NER Schedule 5.2 does not prescribe technology-specific requirements, it outlines performance-based access standards that GFM BESS must meet for connection. These systems are assessed as asynchronous generating units and must demonstrate compliance with clauses such as S5.2.5.1 (Reactive Power Capability), S5.2.5.4 (Response to Voltage Disturbances), and S5.2.5.5 (Response to Disturbances After Contingency Events), etc.

Due to their fast dynamic response, GFM BESS can support system strength and stability. However, achieving compliant performance may require careful tuning of control systems, especially under low system strength or islanding scenarios. For example, response speed and reactive current injection must align with system needs and the agreed performance standards.

Applicants are expected to engage with the transmission network system provider (TNSP) and AEMO to assess and validate performance against relevant clauses, particularly where alternative access standards are proposed. Ultimately, the tuning and configuration of GFM BESS should be tailored to network conditions and verified through detailed studies, without assuming enhanced performance guarantees under all conditions.

#### 2.4.4. UNIFI Consortium Specific Requirements for GFM Resources (Ver. 2)

Existing power system standards primarily focus on GFL IBRs, which limits the widespread adoption and standardisation of GFM resources. Furthermore, inconsistent interpretations of GFM behaviour by manufacturers have led to variability in grid responses, underscoring the need for well-defined performance specifications to guide inverter manufacturers in design and implementation. The UNIFI Consortium seeks to address these challenges by developing standardised GFM integration methodologies for synchronous machines and other IBRs. The initiative defines UNIFI Specifications, ensuring vendor-agnostic operation at both the power system and inverter levels.

According to the North American Electric Reliability Corporation, the UNIFI Consortium defines GFM IBR controls as maintaining an internal voltage phasor that remains constant or nearly constant within the subtransient to transient time frame. While GFL IBRs maintain output current during disturbances and adjust power injection over tens of cycles, GFM IBRs maintain voltage magnitude and phase angle immediately after disturbances, ensuring synchronisation with other grid resources over longer timescales.

##### Performance Requirements for Normal Grid Operation

- **Voltage and Frequency Maintenance:** GFM IBRs must keep voltage and frequency within specified ranges during normal operation and restore deviations to ensure system stability.
- **Autonomous Grid Support:** GFM IBRs should autonomously respond to transient and steady-state changes in voltage, current, and frequency. For example, if voltage drops in a transmission network, the IBR should increase reactive power output to restore stability.
- **Dispatchability of Power Output:** Power output must be adjustable by system operators or local goals (e.g., market clearing), ensuring power can be remotely controlled based on network constraints.
- **Damping of Voltage and Frequency Oscillations:** GFM IBRs must prevent grid oscillations by providing positive damping within common grid resonance frequency ranges.
- **Active and Reactive Power Sharing:** Power output should be autonomously adjusted using droop control, similar to synchronous generators and GFL IBRs.
- **Operation in Low System Strength Grids:** GFM IBRs must operate stably in low-strength grids while avoiding excessive current injection.
- **Response to System Unbalance:** GFM IBRs should provide negative sequence current within their capabilities to help balance voltages in the presence of system unbalances.

##### Performance Requirements for Operation Outside Normal Conditions

- **Ride-Through Behaviour:** GFM IBRs should withstand voltage sags by injecting current to support voltage recovery, within their physical limitations. The priorities during grid events are:
- **Self-protection:** Prevent exceeding critical operational limits.
- **System-wide stability:** Maintain grid-forming behaviour if possible.
- **Optimality:** After ensuring protection and stability, return to setpoint values.
- **Response to Symmetrical Faults:** Maintain balanced internal voltage and inject current to counteract voltage changes. Short-term rated current should be provided temporarily, such as “1.5 times full-rated current for 2 seconds.”

- **Response to Asymmetrical Faults:** Maintain balanced voltage as much as possible, outputting unbalanced currents as necessary.
- **Response to Abnormal Frequency:** Modulate active power to aid in frequency recovery, maintaining stability within standard limits.
- **Response to Phase Jumps and Voltage Steps:** Absorb or inject power to resist phase angle and voltage magnitude changes.

### Additional GFM Capabilities and Considerations

- **Intentional Islanding:** GFM IBRs designed for islanding should maintain stable voltage and frequency. Not all IBRs within an island must have this capability.
- **Black Start and System Restoration:** Some GFM IBRs may provide black start services to aid grid recovery after blackouts, particularly in high-IBR grids where synchronous machines are unavailable.
- **Regulating Voltage Harmonics:** GFM IBRs must comply with voltage harmonic distortion requirements and may inject harmonic currents to mitigate voltage harmonics.
- **Communications with System Operator:** Secure communication should be maintained between GFM IBRs and system operators. Operations must remain unaffected by communication delays or interruptions.
- **Secondary Voltage and Frequency Signal Response:** GFM IBRs should respond to external signals for power flow control and reach a steady-state condition within specified operational limits.

#### 2.4.5. Design and Tuning Guidelines for GFM BESS

It is important to note that, currently, there is no standardised model for GFM BESS, and each manufacturer uses its own proprietary models. For the purposes of providing design guidelines in this document, it is assumed that the general control model shown in [Figure 38](#) is employed. This model serves as a reference for the design of various control layers. The figure illustrates the main control blocks, including the primary control loop, the inner control loops, and the pulse width modulation (PWM) unit. It is noteworthy that the references for the primary control loop are provided by higher-level control systems, such as the power plant controller (PPC), which are not shown in this figure.

As depicted, the inner control loops consist of voltage control (VC) and current control (CC) loops, with the current control loop shown as optional. This reflects recent research trends aiming to eliminate the CC loop in order to increase the control bandwidth of the VC and primary control loops. However, the current protection capabilities of IBRs within these schemes remain uncertain and require further investigation, particularly concerning the use of virtual impedances and their delicate design. These advanced schemes, however, are beyond the scope of this report, which focuses on the generally accepted control structures, including the CC loop.



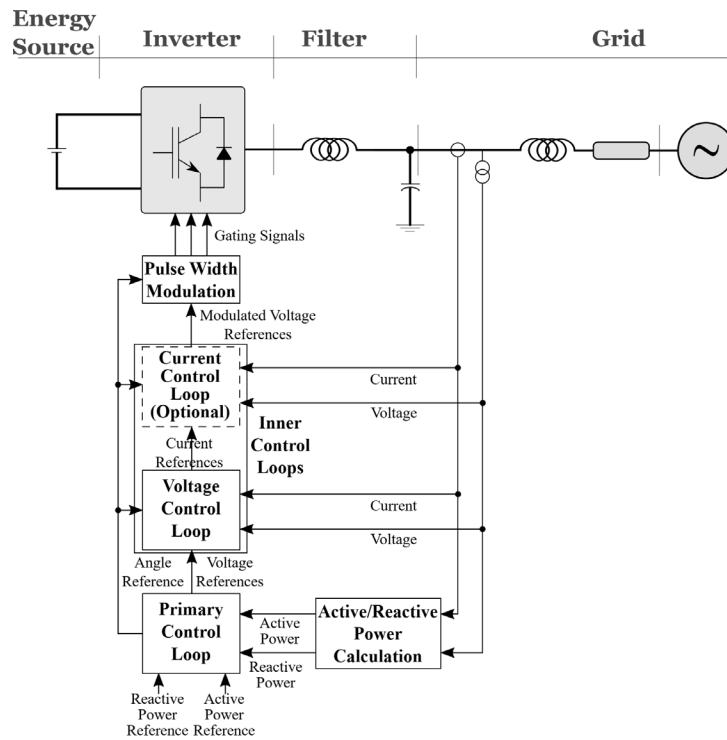


**Figure 38: General block diagram of the control system for a GFM BESS**

### Pulse-Width Modulation Unit

Grid-forming inverters must respond almost instantaneously to voltage disturbances, necessitating a rapid response from the inner control loops. A distinction between grid-forming and grid-following inverters lies in the number of cascaded control loops. Unlike grid-following inverters, grid-forming inverters typically incorporate a greater number of control layers. Given that the conventional approach to designing cascaded control loops involves assigning lower bandwidths to higher control levels relative to lower ones, an increased number of control layers results in significantly reduced bandwidth in the outer loops, particularly the primary control loop. This reduction in bandwidth may lead to inadequate dynamic responses, potentially failing to meet the compliance requirements of NER Schedule 5.2.

One proposed solution, as discussed earlier, involves eliminating the current control loop; however, this approach presents challenges, particularly concerning current protection capabilities. A more practical alternative is to modulate the power electronic switches of the inverter-based resource at higher switching frequencies. This strategy enhances the bandwidth available for the inner control loops, thereby improving the system's dynamic performance and its ability to meet regulatory requirements. Additionally, this technique reduces output voltage distortion and minimises harmonic content. However, careful thermal management is required to mitigate switching losses. Other recommended techniques include:

- Implementing Third-Order Harmonic (TOH) Injection, which improves waveform quality, reduces Total Harmonic Distortion (THD), and enhances inverter efficiency by better utilising the DC bus voltage.
- Utilising Space Vector Modulation (SVM) or advanced modulation schemes to improve DC bus voltage utilisation and reduce harmonic distortion compared to conventional sine-triangle PWM. Furthermore, advanced methods such as Model Predictive Control-based PWM can further optimise inverter performance.

### Current Control Loop

In GFM IBRs, the design and implementation of a dedicated current control loop plays a vital role in achieving robust performance, especially in systems operating at higher switching frequencies. While certain simplified schemes may forgo a current loop, the inclusion of this control layer is strongly



recommended due to its advantages in reliability, dynamic responsiveness, and current-limiting functionality.

### Control Framework and Reference Frame Transformation:

A widely adopted control strategy for IBRs involves executing control in the synchronous rotating reference frame (dq-frame). This approach enables decoupling of active and reactive power control and simplifies the implementation of Proportional-Integral (PI) controllers, which are standard in industrial applications due to their simplicity and effectiveness.

In this framework, the measured three-phase voltages and currents are transformed into two orthogonal components—direct-axis (d) and quadrature-axis (q)—using Clarke-Park transformations. This transformation allows the control actions to be applied independently in each axis, facilitating more precise regulation and improved dynamic behaviour.

### Structure of the Current Control Loop:

A conventional current control loop in the dq-frame typically comprises three main control elements:

- **PI Control Terms:** The core regulators that ensure the dq-axis current components track their reference values. These references are commonly generated by a higher-level control layer, such as the voltage control loop in GFM systems.
- **Decoupling Terms:** These terms compensate for the inherent coupling between the d and q axes, improving control accuracy and system stability during transients.
- **Feedforward Terms:** Implemented as voltage feedforward components, these enhance the loop's ability to reject disturbances and respond quickly to grid dynamics.

The integration of decoupling and feedforward terms is highly recommended, as these elements significantly enhance the current loop's ability to reject disturbances, improve dynamic performance, and enable smoother system startup. They also contribute to increased control bandwidth. However, the voltage control strategy discussed in the next subsection necessitates a relatively low gain for the feedforward terms in the current control loop. To reconcile this with the benefits of feedforward implementation, a low-pass filter must be applied to the voltage feedforward path within the current control loop. This filter ensures compatibility with the voltage loop's bandwidth constraints while preserving the dynamic benefits of feedforward compensation. A characteristic frequency of 50 Hz is recommended for the low-pass filter to suit a wide range of applications.

It is important to emphasise that in GFM IBRs incorporating parallel compensation components, such as filter capacitors or LCL filters, the current measurements used for feedback control should be taken prior to the compensation elements. This ensures that the control loop acts directly on the inverter's output currents rather than distorted downstream quantities.

### Loop Bandwidth and Gain Tuning Considerations:

The current control loop must be designed with a high bandwidth to ensure rapid response and accurate current tracking under dynamic conditions. As such, the tuning of the PI controllers must carefully account for system parameters, including the inverter's filter inductance, desired closed-loop response time, and any inherent measurement and switching delays.

To maintain robust performance and avoid instability due to phase lag or overshoot, the PI controller gains should be selected based on established analytical formulas. The recommended tuning relations are as follows:

$$k_{ii} = K_{cc}L_f \quad (44)$$

$$k_{pi} = K_{cc}R_f \quad (45)$$

in which,  $k_{ii}$  and  $k_{pi}$  denote the integral and proportional gains of the current control PI controller, respectively, while  $L_f$  represents the IBR output harmonic filter inductance. Additionally,  $K_{cc}$  is a design parameter that determines the bandwidth of the current control loop. Higher values of  $K_{cc}$  lead to faster current response; however, the switching frequency imposes a practical upper limit. A  $K_{cc}$  value in the range of 500 to 2000 rad/s is suitable for a wide range of applications.

Note that these equations serve as a starting point for parameter selection and may be further refined through small-signal modelling or time-domain simulations tailored to the specific converter configuration.

### Practical Implementation Considerations:

Beyond theoretical tuning, several practical implementation aspects must be addressed to ensure reliable and safe operation:

- **Output Limiters:** The outputs of the current loop correspond to the terminal voltage reference signals for the inverter. These must be constrained to stay within permissible bounds, which are determined by the nominal DC-link voltage and modulation technique employed. For example, SVM and TOH injection can slightly extend the allowable voltage range, but exceeding these limits leads to overmodulation, increased THD, and degraded voltage quality.
- **Input Limiters:** The input to the current control loop—the current reference values—must also be constrained. These references must not exceed the current handling capacity of the inverter's power electronic switches. Overcurrent conditions pose serious risks of hardware damage and must be avoided through the use of properly tuned current limiters.

### Impact of Current Limiting on Transient Stability:

While current limiting mechanisms are essential for protecting hardware, they can compromise system performance, particularly with respect to transient stability. In GFM IBRs, current limiters restrict the inverter's ability to respond to rapid changes in load or grid conditions, thereby reducing the transient stability margin. Generally, the lower the current limit, the smaller the transient stability margin. To determine an appropriate current limit, [Figure 34](#) and the corresponding results discussed earlier can be referenced.

Different limiting strategies yield different impacts:

- **q-axis Priority Current Limiting:** This approach favours the provision of reactive power support during grid faults, thereby enhancing voltage stability. It is particularly well-suited for weak grid conditions, where maintaining voltage is critical.
- **d-axis Priority Current Limiting:** More beneficial in strong grid environments, d-PCL prioritises active power delivery and typically results in improved overall transient stability under high short-circuit ratio conditions.

The selection between q-PCL and d-PCL should be based on a detailed analysis of the grid strength and the specific performance objectives of the GFM IBR.

### Higher-Level Control Compensation:

It is important to note that higher-level control mechanisms, such as those implemented at the primary and secondary control levels, may compensate for the limitations introduced by current limiting. Advanced techniques can enhance system stability and provide more flexibility in meeting grid requirements.

Further research and development are encouraged to assess how such higher-level strategies can be integrated with the current loop design to achieve both protection and performance goals in GFM applications.

### Voltage Control Loop

In the control hierarchy of grid-forming IBRs, the inner current control loop ensures that terminal current references are tracked with high accuracy and speed. Building upon this, the voltage control loop is tasked

with generating appropriate current references such that the voltage at the GFM PoC accurately follows the reference set by the outer (primary) control loop.

While some implementations omit the voltage loop in favour of virtual impedances for faster dynamic response, this simplification introduces sensitivity to grid strength and requires careful impedance tuning. Hence, in scenarios where high inverter switching frequencies are used, this report recommends retaining the voltage control loop for improved reliability and robustness.

### Control Loop Structure:

The voltage control loop, typically implemented in the dq reference frame, consists of three fundamental components:

- **PI Controller Terms:** Regulate the dq-axis voltage components to follow their references, which are provided by the higher-level (primary) control layer.
- **Decoupling Terms:** Compensate for cross-coupling between the d and q axes to enhance accuracy and stability, particularly during transients.
- **Feedforward Terms:** Introduced through the current feedforward, these improve disturbance rejection and enable a faster dynamic response to grid events.

### Bandwidth Considerations and Tuning Approach:

To avoid interaction with the faster inner current control loop, the voltage control loop should operate with a medium bandwidth. This ensures fast voltage tracking while preserving system stability.

Tuning recommended here is based on the method elaborated in [Appendix E](#), which takes into account the dynamic behaviour of the current loop. The controller gains are defined as:

$$k_{iv} = \frac{\omega_c}{1 - \frac{\omega_c}{\omega_0}} d \times SCR_{max} \quad (46)$$

$$k_{pv} = \frac{\phi_r}{1 - \frac{\omega_c}{\omega_0}} d \times SCR_{max} \quad (47)$$

with:

$$d = \frac{\frac{\omega_0 - \omega_c}{L_f \times SCR_{max}} - \omega_c}{K_{cc} \sin(\phi_{PM} - \phi_r)} \quad (48)$$

in which,  $k_{iv}$  and  $k_{pv}$  denote the integral and proportional gains of the voltage control PI controller, respectively,  $\omega_0 = 2\pi \times 50$  is the nominal angular frequency of the grid, and  $\omega_c$  is the desired bandwidth of the voltage loop, a design parameter that can be selected by the designer.  $K_{cc}$  is the current control gain, which determines the current loop's bandwidth.  $SCR_{max}$  represents the maximum expected short-circuit ratio (grid strength) at the point of connection of the grid-forming IBR, while  $L_f$  denotes the output filter inductance of the IBR. Additionally,  $\phi_{PM}$  is the desired phase margin for the voltage loop, with a typical value of around  $45^\circ$  being suitable. The parameter  $\phi_r$  represents the residue angle resulting from the interaction between the voltage PI controller gains and its open-loop bandwidth. As detailed in [Appendix E](#),  $\phi_r$  is another design parameter and should be chosen within the range of  $(10^\circ, 15^\circ)$ . It is worth mentioning that the above conditions are derived for grids with high X/R ratios; since lower X/R ratios imply higher resistance, the proposed method inherently yields higher stability margins for such grids.

These tuning expressions provide a reliable starting point and should be validated through small-signal analysis or time-domain simulation tailored to the specific converter hardware.

### Decoupling and Feedforward Enhancements:

The use of decoupling and feedforward terms is strongly recommended to enhance dynamic performance and extend the effective control bandwidth. However, special attention must be given to the tuning of the feedforward gains.

Unlike the current control loop, setting the voltage loop feedforward gains to unity can result in poorly damped or even unstable modes, particularly under certain operating conditions. To prevent this, as explained in [Appendix E](#), the feedforward gains should be calculated using the following equation:

$$\beta_i = 1 - d \cos(\phi_{PM} - \phi_r) \quad (49)$$

in which,  $\beta_i$  represents the voltage loop feedforward gains. It is also important to ensure that current measurements used for feedforward control are taken after the parallel filter elements to accurately represent the actual injected current.

### Interaction with Grid Strength and Primary Control:

While maintaining bandwidth separation between the voltage and current loops is a necessary condition for stability in small-signal models, the impact on transient stability is generally limited, provided this separation is preserved.

However, when connected to stronger grids (i.e., higher SCR), care must be taken during voltage loop tuning. Inappropriate bandwidth selection may lead to interaction with the primary control layer, potentially degrading the IBR's transient stability margin. In such cases, tuning must strike a balance between fast response and avoidance of control interference.

### Practical Implementation:

From a practical perspective, it is recommended to limit the rate of change of the voltage setpoint, typically set by the primary control loop. Although this limiter is not directly considered in small-signal analysis, it can significantly influence transient performance.

These rate limiters help decouple the operation of the primary and voltage control loops during fast dynamic events, which in turn enhances the transient stability of the GFM IBR. The precise impact of these practical considerations warrants further analysis, which will be the focus of upcoming studies stemming from this report.

### Primary Control Loop

As discussed in prior sections, grid-forming control strategies such as VSG and droop-based methods utilise comparable inner-loop structures. These fast-acting inner loops are responsible for regulating the voltage phasor, ensuring accurate tracking of both magnitude and phase angle, even under rapidly changing conditions. When adequately tuned and operating at bandwidths significantly higher than the outer control loop, the inner loops offer a stable foundation for voltage regulation. In such configurations, the outer loop becomes the primary driver of the overall dynamic performance and grid-forming behaviour.

The key functional divergence between VSG and droop-based GFMs lies in their outer control loops. This outer layer governs how the converter responds to power–frequency and voltage–reactive power deviations, directly influencing both transient and small-signal stability of the IBR and the surrounding network. Under normal operation and assuming current limiters remain inactive, the outer control loop dictates the transient stability margin. Therefore, its design must be approached with careful consideration of both system-level objectives and operational constraints.

However, this assumption breaks down under fault conditions in strong grid environments. When current limiters are activated, they impose hard constraints on output current, suppressing the influence of the outer loop. In such scenarios, the transient stability is no longer determined by the outer control strategy but instead by the characteristics and activation thresholds of the current limiting system. As a design recommendation, engineers should assess the likelihood of current limiter activation under expected fault

conditions, especially in strong grid scenarios, and ensure that current limiters are coordinated with protection schemes and dynamic performance requirements.

**VSG-Based Control – Parameter Recommendations:**

In the case of VSG-based GFMIs, two outer-loop parameters are central to achieving desirable stability characteristics: the virtual inertia constant and the damping gain.

Virtual Inertia Constant: As summarised in [Table 23](#), increasing the virtual inertia constant generally improves transient stability and extends the CCT. However, similar to synchronous generators, this may also lead to a slight reduction in electromechanical mode damping if not balanced with appropriate damping gain. In very weak networks with low grid strength, excessively high virtual inertia can negatively impact voltage stability and may lead to voltage collapse if not properly managed. Therefore, it is recommended to adopt high virtual inertia values only when both oscillatory mode damping and voltage stability margins are maintained at acceptable levels. Additionally, the energy storage capacity and frequency regulation commitments of the IBR must be sufficient to support the increased inertia demand. These values should be determined through a coordinated approach with the grid operator, taking into account system-level service requirements and the limitations of the IBR’s energy buffer.

Damping Gain: Higher damping gains are also beneficial, improving both transient and small-signal stability. [Table 23](#) highlights that systems with elevated damping exhibit more robust oscillatory mode suppression and improved CCTs. Hence, increased damping gains are recommended, particularly for installations in high SCR environments where interaction between the primary and inner loops can become problematic. In such strong grids, reduced bandwidth separation can lead to control interaction or even instability. To mitigate this, higher damping gains are specifically advised. However, excessive damping can dampen the IBR’s responsiveness to frequency deviations, thus, tuning must also account for the dynamic limits of the battery system. A balanced design should prioritise stability without compromising the IBR’s frequency event performance.

*Table 23: Impact of VSG-based GFM parameters on transient and small-signal stability*

Parameter	TRANSIENT STABILITY		SMALL-SIGNAL STABILITY	
	Effect on CCT	Effect on DOA	Effect on Mode Natural Frequency	Effect on Mode Damping
Virtual Inertia Gain ↑	↑ Increases	↓ Decreases	↓ Decreases	↓ Decreases
Damping Gain ↑	↑ Increases	-	-	↑ Increases

**Droop-Based Control – Parameter Recommendations:**

In droop-based GFMI, the outer-loop functionality is determined by the droop gain, which has an inverse relationship with the damping gain of VSGs. The design considerations are analogous:

Droop Gain: Lower droop gains are generally favourable, as shown in [Table 24](#), enhancing both transient and small-signal stability. Therefore, low droop gains are recommended to maximise the system’s stability margins. However, a flatter power–frequency characteristic resulting from low droop settings demands that the IBR maintain a wider active power variation range, increasing stress on the energy buffer. For this reason, the minimum allowable droop gain should be selected based on the converter’s power capabilities and the grid’s operational expectations.

Table 24: Impact of Droop-based GFM parameters on transient and small-signal stability

TRANSIENT STABILITY			SMALL-SIGNAL STABILITY	
Parameter	Effect on CCT	Effect on DOA	Effect on Mode Natural Frequency	Effect on Mode Damping
Droop Gain ↑	↓ Decreases	↓ Decreases	-	↓ Decreases

As with VSGs, for GFMs connected to very strong grids, the reduced separation between inner and outer loop bandwidths may result in unwanted control interactions. In these cases, lower droop gains (equivalently, higher effective damping) are again recommended to preserve stability.

#### Reactive Power Control – Parameter Recommendations:

Based on the simulation results presented in the previous section, no clear relationship was observed between the RPC gain and transient stability. Therefore, this report does not provide a definitive recommendation for tuning this control loop. However, our experience indicates that a 1-5% droop typically performs well in terms of both small-signal and large-signal stability.

#### Summary of Design Recommendations

To support practitioners in configuring grid-forming converters for both stability and performance, the following design guidelines are recommended:

- Ensure inner loops are significantly faster than outer loops to preserve modular control hierarchy and system stability.
- Use high virtual inertia settings where adequate oscillatory damping can be maintained, and energy storage capacity and frequency regulation commitments permit, prioritising longer CCT and enhanced transient stability margins.
- Adopt higher damping gains, especially in high SCR environments, to prevent instability due to inner–outer loop interactions.
- Specify lower droop gains for droop-based GFMs to improve both transient and small-signal stability, balancing against energy buffer capabilities.
- Avoid excessive damping or excessively low droop gains that may compromise the IBR’s frequency event performance.
- Evaluate current limiter dynamics in strong grids to ensure outer-loop assumptions remain valid under fault conditions.

These recommendations are intended to guide equipment manufacturers, system integrators, and grid operators in collaboratively designing robust, responsive, and regulation-compliant GFM controls tailored to the specific demands of their networks. It is important to note that these guidelines do not explicitly incorporate PPC considerations, which are a critical component affecting GFM plant performance and system interactions. Moreover, adherence to relevant regulatory technical requirements and system operation recommendations remains essential to ensure safe and reliable integration of grid-forming plants. Users are encouraged to apply these guidelines in conjunction with the latest regulatory frameworks and operational practices.

#### 2.4.6. Developed PSCAD Simulation File

To support the practical application of the proposed tuning guidelines and design considerations, a dedicated PSCAD simulation file has been developed. This model integrates all key recommendations outlined in this section, allowing users to explore and apply tuning strategies across multiple control layers in a user-friendly environment.

The simulation file has been designed with flexibility and usability in mind. Users can specify key system-level parameters, such as inverter ratings, network strength, and desired control performance metrics. Based on these inputs, the file automatically configures and tunes the relevant control levels, according to the recommended practices.

This model aims to bridge the gap between theoretical methods and practical implementation, providing a ready-to-use tool that facilitates both learning and deployment of coordinated tuning strategies in a desired power system.

Further details on the PSCAD model are provided in [Appendix F](#).

#### 2.4.7. Critical Learnings and Insights

The investigations carried out in this project have revealed several key technical and methodological insights relevant to IBR stability studies and control tuning in a regulatory context:

- **IBR interactions require system-aware tuning:** Conventional SISO tuning is insufficient in multi-IBR settings, highlighting the need for frameworks that consider plant-to-plant interactions.
- **Regulatory requirements shape control design:** NER S5.2 provisions on voltage control and fault response significantly constrain tuning options, necessitating integrated compliance-aware methods.
- **Tuning methods must balance rigour and usability:** Industry adoption hinges on methods that are technically sound yet interpretable and implementable in real-world settings.
- **System-level coordination is increasingly essential:** Emerging trends and regulatory guidance emphasise co-optimised control across multiple IBRs and network conditions.
- **Simulation remains critical for validation:** Practical tuning and stability approaches must be tested in realistic multi-IBR scenarios, including weak-grid conditions.



### 3. Conclusions

This report presents a comprehensive framework for large-signal transient stability assessment and improvement in power systems increasingly dominated by inverter-based resources, with a particular focus on grid-forming inverters. Through four interrelated research tasks, significant methodological and practical advancements were achieved, addressing both the analytical challenges and operational needs of modern power grids transitioning to high renewable energy penetration.

Task 1 delivered a refined large-signal stability analysis tool that incorporates detailed inverter control dynamics and allows for accurate transient stability margin estimation under a wide range of scenarios. The tool's validation against electromagnetic transient simulations and application to the developed West Murray Zone model demonstrated its practical utility in network planning and operational studies. Key learnings emphasised the influence of outer control loops, slack bus location, and coordinated tuning of reactive power control gains on stability outcomes. The tool enables pre-installation screening and supports more informed decision-making in weak-grid environments.

Task 2 introduced an efficient sensitivity analysis framework to evaluate how control parameters and grid conditions affect stability. It revealed that while inner control loops and RPC dynamics have limited direct influence on critical clearing time, parameters such as inertia, damping, and short-circuit ratio play critical roles in determining system resilience. Importantly, the proposed Lyapunov-based analysis method provides a scalable and less computationally intensive alternative to exhaustive EMT simulations, offering a pathway for both fast and planning-stage assessments.

Task 3 extended the analytical framework to multi-IBR networks, incorporating Lyapunov-based methods to capture complex interactions among multiple GFMs. The approach accurately estimates system-wide CCT and identifies how control settings, network topology, and line impedance variations influence transient stability. This task affirmed the need for coordinated inverter tuning strategies and network-aware planning to avoid instability arising from plant-to-plant interactions or adverse topological configurations.

Task 4 focused on developing practical, compliance-aligned tuning and design guidelines tailored to multi-IBR networks under the National Electricity Rules. Findings highlighted that traditional SISO tuning methods are inadequate, underscoring the importance of system-level, coordinated approaches that consider regulatory constraints and system dynamics. Virtual inertia, damping, and droop settings were shown to significantly affect both transient and small-signal stability, with trade-offs between energy availability, recovery performance, and control robustness.

Additionally, the project delivered a ready-to-use PSCAD simulation model, incorporating detailed GFM representations and automated tuning procedures. This model enables stakeholders to evaluate tuning strategies under realistic conditions and supports industry readiness through hands-on validation of proposed methodologies.

Collectively, the outcomes of this research provide:

- Validated tools for accurate and efficient large-signal stability analysis,
- Insights for parameter sensitivity and system interactions,
- Guidelines for coordinated and regulation-compliant tuning, and
- Models to support practical adoption and ongoing industry collaboration.

These contributions empower system operators, planners, and technical managers to address the pressing challenges of managing IBR-rich grids, particularly in weak or renewable-intensive regions. The work enhances the capacity for proactive stability management, informed decision-making, and secure integration of emerging technologies.



## 4. Recommendation Research Priorities

The following future research activities are aligned with the 2021 Roadmap and are prioritised based on their criticality and urgency. Each task builds upon the findings of Stage 4 and aims to further enhance the large-signal stability of IBR-dominated networks.

### High Priority (Short-Term)

- Investigation of the Impact of Current Limiters on Stability Margins and Domain of Attraction
  - Evaluate how current limiters influence large-signal stability, particularly the domain of attraction under fault conditions.
  - Build on Stage 4 insights using PSCAD simulations (e.g., West Murray benchmark) and an upgraded modelling tool.
  - Deliver an updated limiter-tuning note and improvements to the fault-handling framework.
- Assessment of Asymmetrical Faults and Their Impact on Transient Stability
  - Extend the current large-signal stability framework to handle unbalanced and negative-sequence dynamics.
  - Investigate the sensitivity of grid-forming and grid-following inverters to asymmetrical faults, particularly in weak grids.
  - Refine protection design and control tuning approaches, supported by enhanced EMT-based fault analysis methods.
- Electrolysers and Inverter-Based Loads (IBLs) Modelling for Grid Integration Studies
  - Build detailed EMT models of electrolysers and other inverter-based loads.
  - Provide validated benchmark cases, a modelling guideline, and representative demo studies.
  - Enhance planning and operational tools to consider the dynamic behaviour of large-scale inverter-connected loads.
- Quantification and Application of System-Strength Support (SSS) Metrics
  - Use EMT simulations to derive SSS sizing curves and planning metrics.
  - Investigate sensitivities to reactive power set-points, inverter tuning, and distance from grid support.
  - Validate results in PSCAD and produce a planning note for TNSPs and project developers.

### Medium Priority (Medium-Term)

- Development of Transient Stability Enhancement Methods for GFMIs
  - Formulate a generalised method for improving transient stability under a range of grid conditions.
  - Address interactions between control systems and current limiters that affect post-fault stability.
  - Support the reduction of curtailment events and improve inverter reliability in weak networks.
- Extension of the Transient Stability Enhancement Method to Multi-IBR and Mixed Systems

- Apply stability enhancement strategies to interconnected systems with multiple inverters and inverter-based loads.
- Analyse coordinated behaviour and develop multi-inverter tuning and control guidelines.
- Support long-term integration of diverse inverter technologies in high-renewable power systems.
- Development of Coordinated Grid-Forming and Grid-Following Inverter Control Strategies
  - Design coordinated control frameworks for GFMI and GFLI to support stable operation across various grid conditions.
  - Leverage EMT studies of mixed IBR/IBL faults in weak grid environments.
  - Develop coordinated fault ride-through rules and publish a stability performance report for operators and manufacturers.

### Low Priority (Long-Term)

- Development of Advanced Protection Schemes for IBR-Dominated Grids
  - Explore adaptive protection strategies that address the fast dynamics of inverter-based systems.
  - Integrate findings from asymmetrical fault studies to improve fault detection, discrimination, and ride-through capability.
  - Produce a refined grid-forming inverter guide tailored to modern protection needs.
- Integration of AI-Based Predictive Stability Assessment Tools for Future Power Systems
  - Explore AI and machine learning methods for real-time stability assessment, fault detection and adaptive control.
  - Develop data-driven frameworks to autonomously adjust inverter settings in response to grid conditions.
  - Enable predictive and resilient operation in complex, high-renewable environments.

# Appendix A

## Parameters Used for the 3-Cluster Model

*Apx Table A. 1: System and control parameters for the 3- cluster network*

PARAMETER	VALUE (BASE CASE)
Base Power (MVA)	55
Base Voltage (kV)	110
$\omega_0$ (rad/s)	$2\pi \times 50$
$V_g$ (pu)	1
$Z_g$ (pu)	j0.15
$Z_{c,2}$ (pu)	0.010+j0.300
$Z_{c,3}$ (pu)	0.010+j0.300
$P_{FM,2.1}$ (MW)	22.5
$P_{FM,3.1}$ (MW)	26.0
$V_{FM,2.1}$ (pu)	1.03
$V_{FM,3.1}$ (pu)	1.03
$I_{FL,d,1.1} + I_{FL,q,1.1}$ (pu)	0.63 - j0.44
$I_{FL,d,2.1} + I_{FL,q,2.1}$ (pu)	0.50 - j0.31
$I_{FL,d,2.2} + I_{FL,q,2.2}$ (pu)	0.63 - j0.38
$I_{FL,d,3.1} + I_{FL,q,3.1}$ (pu)	0.63 - j0.50
$Z_{1,2}$ (pu)	0.005+j0.150
$Z_{1,3}$ (pu)	0.005+j0.150
$Z_{1,2}$ (pu)	0.0075+j0.225
$Z_{L,1}$ ( $\Omega$ )	1210

# Appendix B

## Parameters Used for the PSCAD Models

Apx Table B. 1: System and control parameters for the base case

PARAMETER	SYMBOL	VALUE
Rated DC Link Voltage (kV)	$V_{dc}$	3
Grid Voltage (kV)	$V_g$	33
Power reference (MW)	$P_{ref}$	0.8
Inverter Side Resistance ( $\Omega$ )	$R_f$	0.01
Inverter Side Inductance (mH)	$L_f$	0.2
Filter Capacitor ( $\mu\text{F}$ )	$C_f$	70
Inner Control Loops		
Proportional gain of VC (S)	$k_{pv}$	2
Integral gain of VC (S/s)	$k_{iv}$	5
Time constant of CC (s)	$T_i$	1/1500
Primary Control Loops		
Inertia Coefficient ( $\text{Ws}^2/\text{rad}$ )	$J$	1230
Droop Coefficient (Hz/W)	$D_p$	$3.042 \times 10^{-6}$
Proportional gain of RPC (V/var)	$k_{pq}$	$5 \times 10^{-7}$
Integral gain of RPC (V/var·s)	$k_{iq}$	$1 \times 10^{-6}$

## CCT and CCA for the Tested Control Parameters of GFM

Apx Table B. 2: CCT and CCA for tested control parameters of droop control GFMI with weak SCR = 2 and SCR = 4

PARAMETER		SCR = 2		SCR = 4	
		CCT (s)	CCA (deg)	CCT(s)	CCA (deg)
Base case		0.97	157.853	1.07	169.310
$P_{ref}$	0.5	1.82	170.596	1.84	173.146
	1.0	0.69	150.209	0.80	165.373
$D_p$	$1.52 \times 10^{-6}$	1.88	155.340	2.14	169.212
	$6.08 \times 10^{-6}$	0.49	155.901	0.52	168.939
$k_{pv}$	1	0.98	157.967	1.07	169.158
	3	0.96	157.456	1.06	168.958

$k_{iv}$	2.5	0.96	154.966	1.06	169.087
	7.5	0.95	155.108	1.08	168.822
$T_{iv}$	1/1000	0.98	157.765	1.06	168.942
	1/1500	0.96	157.765	1.07	169.329
$k_{pq}$	$5 \times 10^{-8}$	0.97	157.727	1.06	169.197
	$5 \times 10^{-6}$	0.97	157.765	1.07	169.277
$k_{iq}$	$1 \times 10^{-7}$	0.97	157.626	1.07	169.297
	$1 \times 10^{-5}$	0.97	157.655	1.06	169.267

Apx Table B. 3: CCT and CCA for tested control parameters of VSG control GFMI with SCR = 2 and SCR = 4

PARAMETER		SCR = 2		SCR = 4	
		CCT (s)	CCA (deg)	CCT(s)	CCA (deg)
Base case		1.47	112.319	1.75	123.068
$P_{ref}$	0.5	2.45	137.143	2.65	141.027
	1.0	1.09	98.217	1.42	112.661
$D_p$	$1.52 \times 10^{-6}$	2.13	133.411	2.65	141.140
	$6.08 \times 10^{-6}$	1.15	97.146	High oscillations	
$J$	615	1.23	123.340	1.42	131.488
	1645	1.65	107.428	2.01	120.473
$k_{pv}$	1	1.47	111.809	1.76	122.967
	3	1.46	111.886	1.75	124.383
$k_{iv}$	2.5	1.48	113.471	1.74	121.999
	7.5	1.46	111.391	1.74	124.221
$T_{iv}$	1/1000	1.46	111.391	1.74	121.999
	1/1500	1.48	113.471	1.75	123.049
$k_{pq}$	$5 \times 10^{-8}$	1.46	111.886	1.75	123.044
	$5 \times 10^{-6}$	1.47	112.229	1.73	121.186
$k_{iq}$	$1 \times 10^{-7}$	1.47	111.486	1.74	123.102
	$1 \times 10^{-5}$	1.48	112.339	1.75	121.086

Apx Table B. 4: CCT and CCA for tested control parameters of CGVSG control GFMI with SCR = 2 and SCR = 4

PARAMETER		SCR = 2		SCR = 4	
		CCT (s)	CCA (deg)	CCT(s)	CCA (deg)
Base case		1.91	118.913	2.94	131.524
0.5		3.10	136.45	4.33	143.423

$P_{ref}$	1.0	1.41	106.31	2.39	123.993
$D_p$	$1.52 \times 10^{-6}$	2.11	132.374	2.72	138.547
	$6.08 \times 10^{-6}$	2.38	122.142	3.98	135.424
$J$	615	1.35	123.698	1.90	131.670
	1645	2.40	116.851	3.89	132.553
$k_{pv}$	1	1.90	118.257	2.92	130.349
	3	1.91	118.844	2.95	132.079
$k_{iv}$	2.5	1.94	121.137	2.93	130.318
	7.5	1.89	117.800	2.95	132.079
$T_{iv}$	1/1000	1.91	118.913	2.94	131.524
	1/1500	1.91	118.922	2.94	131.532
$k_{pq}$	$5 \times 10^{-8}$	1.91	118.916	2.94	129.538
	$5 \times 10^{-6}$	1.89	117.427	2.94	129.560
$k_{iq}$	$1 \times 10^{-7}$	1.91	118.914	2.94	129.512
	$1 \times 10^{-5}$	1.48	118.221	2.94	129.535

Apx Table B. 5: Summary of findings

CONTROL STRATEGY	GRID CONDITION	IMPACT OF INNER LOOP	IMPACT OF RPC	IMPACT OF APC ( $P_{ref}$ )	IMPACT OF APC ( $D_p$ )	IMPACT OF APC ( $J$ )
Droop	SCR =2	Negligible	Negligible	High	High	-
	SCR =4				High	-
VSG	SCR =2				High	High
	SCR =4				Very High	High
CGVSG	SCR =2				Moderate	High
	SCR =4				High	High

# Appendix C

## Parameters Used for the 5-Bus System

Apx Table C. 1: System for the 5-bus system: base case

SYMBOL	VALUE
$V$ (kV)	33
$Z_{1,2}(\Omega)$	$j39.89$
$Z_{1,3}(\Omega)$	$j65.00$
$Z_{2,3}(\Omega)$	$j49.95$
$Z_{3,4}(\Omega)$	$j59.69$
$Z_{1,4}(\Omega)$	$j54.97$
$Z_{2,5}(\Omega)$	$j44.92$
$Z_{5,4}(\Omega)$	$j58.11$
$Z_{FM,1}(\Omega)$	$j3.14$
$Z_{FM,2}(\Omega)$	$j4.54$
$Z_{FM,3}(\Omega)$	$j4.94$
$Z_g(\Omega)$	$j3.14$
$P_{ref,1}$ (MW)	0.8
$P_{ref,2}$ (MW)	0.5
$P_{ref,3}$ (MW)	0.7
$J_1$ ( $Ws^2/rad$ )	369.36
$J_2$ ( $Ws^2/rad$ )	492.48
$J_3$ ( $Ws^2/rad$ )	861.84

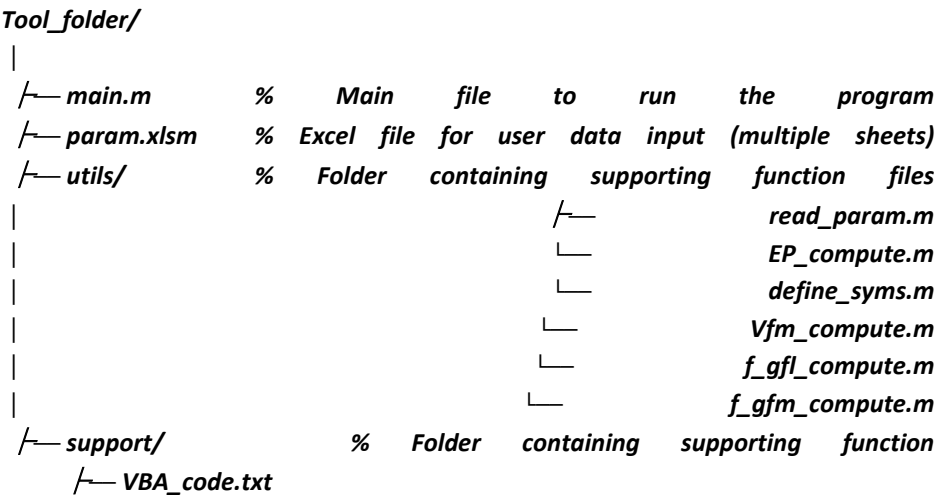
# Appendix D

## User Guide for Running the Developed Tool with Excel-Based Input

This appendix provides an overview and user guide for the MATLAB tool introduced in [Section 2.1](#) for the multi-IBR networks. It follows the parameter definitions presented in [Figure 2](#) and aims to assist users in preparing these parameters and other required input data, executing the code, and interpreting the output results.

### Tool Structure

The project folder is organised as shown in [Apx Figure D. 1](#):



**Apx Figure D. 1: The organisation of the project folder**

Here is the brief description of the tool folder:

#### **main.m**

This is the primary MATLAB script to be executed by the user. It reads input data from the Excel file and generates outputs by calling supporting functions located in the utils folder for a multi-IBR network.

#### **param.xlsm**

This Excel file is used for user data input related to the multi-IBR configuration, impedances, specification of IBRs and initial values.

#### **utils/**

This folder contains MATLAB functions that perform specific, modular tasks to support the main script. These functions are not intended to be executed directly by the user but are called internally.

#### **VBA\_code.txt**

This text file contains the developed VBA code for the Excel macro. It generates the required sheets based



on the configuration in the Config sheet. The macro is triggered by clicking a button in the Config sheet.

## Data Preparation in Excel File

In this section, we guide users through the process of preparing input data in the provided Excel file.

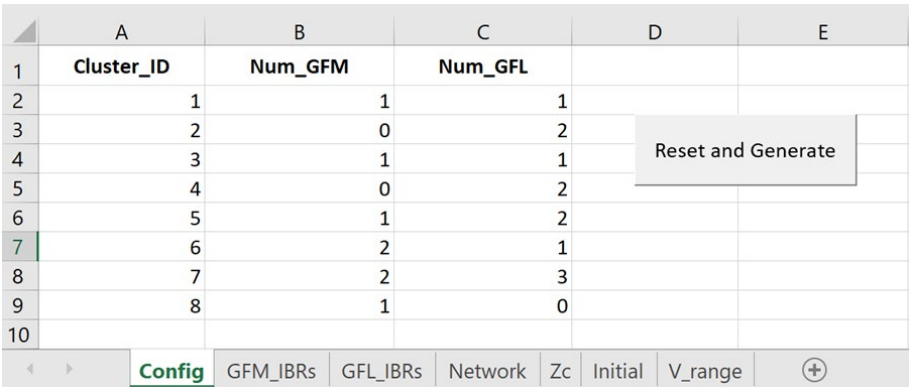
### Before You Start

Firstly, ensure that macros are enabled in your Excel environment. If you encounter issues, the VBA macro code is available in the project folder (VBA\_code.txt). The Excel file contains multiple sheets, each representing a different category of data (e.g., “Config”, “GFM\_IBRs”, “GFL\_IBRs”, “Network”, “Zc”, “Initial”, “V\_range”) for inputting different categories of data. The main sheet is “Config”, as shown in the following figure.

### Step 1: Config Sheet

This sheet contains high-level configuration data for the multi-IBR network. Consider an example multi-IBR network that includes 8 clusters, each with a specific number of GFM and GFL IBRs. To fill in this sheet,

- Enter the number of IBRs per cluster under “Num\_GFM” and “Num\_GFL” columns (refer to [Apx Figure D. 2](#) as an example)
- After completing this input, click the “**Reset and Generate**” button. This will reset and populate the subsequent sheets needed for detailed input.



	A	B	C	D	E
	Cluster_ID	Num_GFM	Num_GFL		
1					
2	1	1	1		
3	2	0	2		
4	3	1	1	Reset and Generate	
5	4	0	2		
6	5	1	2		
7	6	2	1		
8	7	2	3		
9	8	1	0		
10					

**Apx Figure D. 2: Sample of “Config” sheet**

### Step 2: GFM\_IBRs Sheet

In this sheet, provide the following data for each GFM IBR (refer to [Apx Figure D. 3](#) as an example):

- Active and reactive power: P, Q
- Control gains: K\_pq
- Voltage: V
- Impedance: Z\_real, Z\_imag

	A	B	C	D	E	F	G	H
1	Cluster_ID	GFM_ID	P	Q	K_pq	V	Z_real	Z_imag
2	1	1	5.00E+07	0	2.40E-06	1.85E+05	7.61E-01	6.84E+00
3	3	1	2.00E+08	0	2.40E-06	1.85E+05	4.38E-01	3.94E+00
4	5	1	1.50E+08	0	2.40E-06	1.85E+05	9.46E-01	8.51E+00
5	6	1	1.80E+08	0	2.40E-06	1.85E+05	1.29E+00	11.6337951
6	6	2	2.50E+07	0	2.40E-06	1.85E+05	1.62E+00	14.6074005
7	7	1	1.03E+08	0	2.40E-06	1.85E+05	6.12E-01	5.50E+00
8	7	2	1.16E+08	0	2.40E-06	1.85E+05	5.27E-01	4.74169376
9	8	1	1.85E+08	0	2.40E-06	1.85E+05	0.75	6.75E+00
10								
		Config	GFM_IBRs	GFL_IBRs	Network	Zc	Initial	V_range

**Apx Figure D. 3: Sample of “GFM\_IBRs” sheet**

### Step 3: GFL\_IBRs Sheet

In this sheet, enter the following parameters for each GFL IBR (refer to [Apx Figure D. 4](#) as an example):

- Current components: I\_d, I\_q
- Impedance: Z\_real, Z\_imag

	A	B	C	D	E	F	G	H
1	Cluster_ID	GFL_ID	I_d	I_q	Z_real	Z_imag		
2	1	1	334.02	-109.79	0.9155	8.2372308		
3	2	1	300.62	-98.81	0.5425	4.88115534		
4	2	2	630.93	-207.38	0.6225	5.60095705		
5	3	1	1484.54	-487.94	0.2775	2.49681218		
6	4	1	326.6	-107.35	2.5375	22.8312105		
7	4	2	326.6	-107.35	0.767	6.90109888		
8	5	1	742.27	-243.97	0.7445	6.69865465		
9	5	2	556.7	-182.98	0.886	7.97180392		
10	6	1	185.57	-60.99	1.546	13.910168		
11	7	1	200.41	-65.87	0.438	3.94091436		
12	7	2	111.34	-36.6	1.213	10.9139934		
13	7	3	1002.06	-329.36	1.789	16.0965657		
14								
		Config	GFM_IBRs	GFL_IBRs	Network	Zc	Initial	V_range

**Apx Figure D. 4: Sample of “GFL\_IBRs” sheet**

### Step 4: Network Sheet

In this sheet, the admittance between clusters are defined. For inserting the admittance value from cluster  $i$  to cluster  $j$ , enter Y\_real and Y\_imag in the corresponding row (refer to [Apx Figure D. 5](#) as an example). Note that the code automatically mirrors this value from  $j$  to  $i$ , so you do not need to input it twice.

	A	B	C	D	E	F	G
1	From_cluster	To_cluster	Y_real	Y_imag			
2	1	2	0.01389326	-0.1250049			
3	1	3	0	0			
4	1	4	0.00463109	-0.0416683			
5	1	5	0	0			
6	1	6	0	0			
7	1	7	0	0			
8	1	8	0	0			
9	2	3	0.01040514	-0.0936205			
10	2	4	0	0			
11	2	5	0	0			
12	2	6	0	0			
13	2	7	0	0			
14	2	8	0	0			
<div> <span>&lt;</span> <span>&gt;</span> Config GFM_IBRs GFL_IBRs <b>Network</b> Zc Initial V_range </div>							

**Apx Figure D. 5: Sample of “Network” sheet**

### Step 5: Zc Sheet

In this sheet, enter the impedance between each cluster and the global common bus (refer to [Apx Figure D. 6](#) as an example):

- Impedance: Z\_real, Z\_imag

	A	B	C	D	E	F	G	H
1	Cluster_ID	Z_real	Z_imag					
2	1	1.57E+01	1.41E+02					
3	2	1.66E+01	1.49E+02					
4	3	1.54E+01	1.39E+02					
5	4	1.31E+01	1.18E+02					
6	5	1.46E+01	1.31E+02					
7	6	7.04E+00	6.33E+01					
8	7	5.93E+00	5.34E+01					
9	8	9.81E+00	8.82E+01					
10								
<div> <span>&lt;</span> <span>&gt;</span> Config GFM_IBRs GFL_IBRs Network <b>Zc</b> Initial V_range </div>								

**Apx Figure D. 6: Sample of “Zc” sheet**

### Step 6: Initial Sheet

The proposed method requires initial guesses for voltage values  $V_h \cos \delta$  and  $V_h \sin \delta$  for each cluster  $h$  based on its angle. These values are initially treated as symbolic variables in the formulation and are later computed numerically using the Newton-Raphson algorithm. Therefore, the initial values are required to initialise the iterative solver.

In this sheet, enter initial guesses for both of the following cases (refer to [Apx Figure D. 7](#) for an example):

- Stable Equilibrium Point: under the V\_SEP column
- Unstable Equilibrium Point: under the V\_UEP column

	A	B	C	D	E	F	G	H
1	<b>Var</b>	<b>V_SEP</b>	<b>V_UEP</b>					
2	vhcos_1	1.19E+05	-1.26E+05					
3	vhsin_1	1.39E+05	9.78E+04					
4	vhcos_2	1.12E+05	-1.31E+05					
5	vhsin_2	1.44E+05	8.75E+04					
6	vhcos_3	1.04E+05	-1.48E+05					
7	vhsin_3	1.53E+05	8.56E+04					
8	vhcos_4	1.28E+05	8.56E+04					
	Config	GFM_IBRs	GFL_IBRs	Network	Zc	Initial	V_range	

**Apx Figure D. 7: Sample of "Initial" sheet**

### Step 7: V\_range Sheet

This sheet specifies two sets of parameters: one related to the grid, and the other to the voltage ranges used by the Newton-Raphson algorithm implemented in the code to identify Stable Equilibrium Points and Unstable Equilibrium Points.

The first part includes grid impedance  $Z_g$  in terms of ( $Z_{g\_real}$ ,  $Z_{g\_imag}$ ), along with the line-to-line RMS grid voltage  $V_g$ . The second part defines the voltage search ranges and step sizes used by the Newton-Raphson algorithm. These ranges are defined as "[V\_SEP\_m : step\_SEP : V\_SEP\_M]" for the SEP, and "[V\_UEP\_m : step\_UEP : V\_UEP\_M]" for the UEP. Based on the grid voltage  $V_g$ , it is recommended to select the ranges as 0.7 $V_g$  to 1.1 $V_g$  for the SEP, and 0 to 0.7 $V_g$  for the UEP.

Note that choosing tighter bounds can improve convergence speed and reduce computational time, as demonstrated in [Apx Figure D. 8](#).

	A	B	C	D	E	F	G	H	I
1	<b>Zg_real</b>	<b>Zg_imag</b>	<b>Vg</b>	<b>V_SEP_m</b>	<b>V_SEP_M</b>	<b>step_SEP</b>	<b>V_UEP_m</b>	<b>V_UEP_M</b>	<b>step_UEP</b>
2	0	3.14159265	220000	151000	188000	1000	115000	130000	1000
3									
	Config	GFM_IBRs	GFL_IBRs	Network	Zc	Initial	V_range		

**Apx Figure D. 8: Sample of "V\_ranges" sheet**

## Running the Code

Follow these steps to execute the MATLAB tool:

1. Ensure all required data has been filled in and saved in the Excel file, as instructed.
2. Open MATLAB and navigate to the project folder containing the code.
3. Run the script by executing main.m.

## Interpreting the Results

Here are the intended outputs from the code. The outputs are listed as

- The voltage and angle of the clusters in the SEP and UEP cases
- The angles of IBRs for SEP and UEP cases
- The DEP values of clusters, where the final  $DEP = \min(DEP\_h)$

*Apx Table D. 1: Resulting SEP and UEP voltage and angle values from the developed tool*

<p>==== SEP ====</p> <p><b>Vc_SEP</b> = 167.000 kV</p> <p><b>V_SEP</b> = [180.942, 181.2857, 183.6237, 176.7618, 183.0022, 181.0494, 182.9268, 180.5359] kV</p> <p><b>Δ_SEP</b> = [48.4837, 51.2388, 54.7651, 43.3618, 54.3673, 36.7591, 37.8878, 40.703] rad</p> <p>Theta_1_1_SEP = 0.83944 delta_1_1_SEP = 0.26468</p> <p>Theta_2_1_SEP = 0.44683 Theta_2_2_SEP = 1.0761</p> <p>Theta_3_1_SEP = 1.1144 delta_3_1_SEP = 0.85333</p> <p>Theta_4_1_SEP = 2.3294 Theta_4_2_SEP = 0.70391</p> <p>Theta_5_1_SEP = 1.5 Theta_5_2_SEP = 1.3388 delta_5_1_SEP = 1.3911</p> <p>Theta_6_1_SEP = 0.78708 delta_6_1_SEP = 2.2819 delta_6_2_SEP = 0.2882</p> <p>Theta_7_1_SEP = 0.23834 Theta_7_2_SEP = 0.36671 Theta_7_3_SEP = 4.8734 delta_7_1_SEP = 0.58209 delta_7_2_SEP = 0.56416</p> <p>delta_8_1_SEP = 1.3012</p>	<p>==== UEP ====</p> <p><b>Vc_UEP</b> = 120.000 kV</p> <p><b>V_UEP</b> = [160.7092, 159.1844, 171.9927, 130.8486, 168.9066, 164.5693, 172.2894, 165.1102] kV</p> <p><b>Δ_UEP</b> = [139.5404, 143.6521, 147.2776, 128.9257, 145.2726, 105.4243, 106.442, 116.3464] rad</p> <p>Theta_1_1_UEP = 0.94513 delta_1_1_UEP = -0.42937</p> <p>Theta_2_1_UEP = 0.50887 Theta_2_2_UEP = 1.2256</p> <p>Theta_3_1_UEP = 1.1898 delta_3_1_UEP = 0.55108</p> <p>Theta_4_1_UEP = 3.1474 Theta_4_2_UEP = 0.95092</p> <p>Theta_5_1_UEP = 1.6253 Theta_5_2_UEP = 1.4506 delta_5_1_UEP = 1.0235</p> <p>Theta_6_1_UEP = 0.8659 delta_6_1_UEP = 1.9213 delta_6_2_UEP = -0.29085</p> <p>Theta_7_1_UEP = 0.25306 Theta_7_2_UEP = 0.38935 Theta_7_3_UEP = 5.1751 delta_7_1_UEP = 0.27142 delta_7_2_UEP = 0.25869</p> <p>delta_8_1_UEP = 0.89321</p>
--	---

*Apx Table D. 2: Computed DEP values from the developed tool*

<p>DEP_1=1.8781</p> <p>DEP_2=1.8036</p> <p>DEP_3=1.6893</p> <p>DEP_4=1.9733</p> <p>DEP_5=1.6721</p> <p>DEP_6=1.868</p> <p>DEP_7=1.8094</p> <p>DEP_8=1.8584</p> <p><b>DEP=1.6721</b></p>
---

## Final Notes Regarding Modifications

The developed code is structured with a highly modular design, enabling seamless interaction with an external Excel-based data input file. This design provides flexibility for 1) adding, removing, or updating inverter-based resources and 2) modifying the network configuration between clusters without altering the underlying code structure.

### Modifying IBR Configuration

To adjust the IBR configuration, we need to update both the “Config” sheet and the corresponding IBR sheet (e.g., “GFL\_IBR”, “GFM\_IBR”) within the Excel file. As a reminder, always save the Excel file after making any modifications. The code reads the saved state and reflects the changes accordingly during execution.

#### To Remove an IBR:

- Update the relevant parameter (e.g., Num\_GFM) in the “Config” sheet to reflect the new number of devices in the cluster.
- Remove the corresponding data row in the associated IBR sheet (e.g., “GFM\_IBR” or “GFL\_IBR”).

#### To Add a New IBR:

- Append the new IBR data to the related IBR sheet.
- Increment the “Num\_GFM” or “Num\_GFL” value in the “Config” sheet accordingly.

For example, to remove the second GFM unit from Cluster 7, set the Num\_GFM to 1 in the “Config” sheet and simply delete the second GFM row for Cluster 7 from the “GFM\_IBR” sheet

In this case, the code gives us the new DEP values as

**Apx Table D. 3: Computed DEP values after removing GFM2 from cluster 7**

DEP_1=2.2392
DEP_2=2.1463
DEP_3=2.0028
DEP_4=2.3412
DEP_5=1.9767
DEP_6=2.1308
DEP_7=2.093
DEP_8=2.1484
<b>DEP=1.9767</b>

Now, to add a new GFM unit, add the new data entry to the “GFM\_IBR” sheet and update “Num\_GFM” in the Config sheet to match the new count. While it is preferable to insert the new IBR entry alongside related data (for better organisation), the code will still function correctly even if the entry is appended to the end of the sheet as below

## Supporting Multiple Networks

The framework supports different network topologies between clusters as well as other line impedance configurations. To modify the setup, navigate to the “Network” sheet and update the admittance values between clusters and any other intended impedances in the designated sheet (e.g., “GFM\_IBR”, “GFL\_IBR”, “Zc”, and “V\_range” sheet). Be sure to save the Excel file after making any changes, as the code reads from

the most recently saved version. The spreadsheet is already structured to accommodate such updates, and the code will adjust its calculations accordingly.

# Appendix E

## Voltage Controller Tuning Methodology

This appendix outlines the recommended tuning methodology for the voltage control loop of grid-forming inverters, with particular attention to the dynamic behaviour of the inner current control loop. The approach ensures that tuning accounts for system stability and performance under realistic operating conditions.

For the grid-forming control scheme shown in [Figure 38](#), the open-loop voltage-current controller can be written as:

$$\eta_v \Delta \vec{v}_c = C_i(s) C_v(s) [\Delta \vec{v}_{ref} - \Delta \vec{v}_c] - [sL_f + \eta_i C_i(s)] \Delta \vec{i}_g, \quad (\text{A.E1})$$

where,

- $\eta_v = 1 - \beta_v$ :  $\beta_v$  is the voltage feedforward gain within current control,
- $\eta_i = 1 - \beta_i$ :  $\beta_i$  is the current feedforward gain within the voltage control,
- $C_v(s) = k_{pv} + k_{iv}/s$ : Voltage PI controller,
- $C_i(s) = k_{pi} + k_{ii}/s$ : Current PI controller,
- $\Delta \vec{v}_c$ : Small perturbation in voltage,
- $\Delta \vec{v}_{ref}$ : Reference voltage perturbation,
- $L_f$ : Inductance of the LC filter,
- $\Delta \vec{i}_g$ : Small perturbation in grid current, and
- $s$ : Laplace operator.

The VC loop model subsystem is therefore implicitly described by the above equation with

$\{\Delta \vec{v}_{ref}, \Delta \vec{i}_g\}$  as the inputs and  $\Delta \vec{v}_c$  as the output. The grid dynamics are modelled by applying KCL over the grid impedance, where:

$$\frac{\Delta \vec{i}_g}{\Delta \vec{v}_c - \Delta \vec{v}_n} = \vec{Z}_g^{-1} = \frac{1}{sL_g + R_g + j\omega_1 L_g}, \quad (\text{A.E2})$$

where,

- $\Delta \vec{v}_n$ : Small perturbation in network voltage,
- $\vec{Z}_g^{-1}$ : Inverse of the grid impedance,
- $L_g$ : Inductance of the grid,
- $R_g$ : Resistance of the grid,
- $\omega_1 = 2\pi \times 50$ : Electrical angular frequency base, and
- $j$ : Imaginary unit.

Therefore, the grid model subsystem is described by the above equation with  $\{\Delta \vec{v}_{ref}, \Delta \vec{i}_g\}$  as the inputs, and  $\Delta \vec{i}_g$  as the output.

As a result, the open-loop voltage-current controller can be written as



$$\vec{G}_{v,ol}(s) = \frac{C_i(s)C_v(s)\vec{Z}_g}{sL_f + \eta_i C_i(s) + \eta_v \vec{Z}_g}, \quad (\text{A.E3})$$

where  $\vec{G}_{v,ol}(s)$  is the open-loop voltage-current transfer function. This can be expanded to:

$$\vec{G}_{v,ol}(s) = \frac{1}{s} \frac{(sk_{pv} + k_{iv})(k_{pi} + k_{ii}/s)(R_g + sL_g + jX_g)}{sL_f + \eta_i(k_{pi} + k_{ii}/s) + \eta_v(R_g + sL_g + jX_g)}, \quad (\text{A.E4})$$

where,

- $k_{pv}$ : Proportional gain of the voltage controller,
- $k_{iv}$ : Integral gain of the voltage controller,
- $k_{pi}$ : Proportional gain of the current controller,
- $k_{ii}$ : Integral gain of the current controller, and
- $X_g = \omega_1 L_g$ : Reactance of the grid.

Since the negative frequency response determines the stability margin of the voltage loop, it is obtained by inserting  $s = -j\omega$  in the above equation for  $\vec{G}_{v,ol}$  as:

$$G_{v,ol}^-(\omega) = \frac{1}{\omega} \frac{(\omega k_{pv} + jk_{iv})(k_{pi} + jk_{ii}/\omega)(R_g - j\omega L_g + jX_g)}{\eta_i k_{pi} + \eta_v R_g + j[\eta_i k_{ii}/\omega - (\eta_v L_g + L_f)\omega + \eta_v X_g]}. \quad (\text{A.E5})$$

The crossover frequency  $\omega_{v,ol}^-$  is solved by fitting the gain and phase requirements, i.e.,

$$|G_{v,ol}^-(\omega_{v,ol}^-)| = 1, \arg[G_{v,ol}^-(\omega_{v,ol}^-)] \approx \pi - \phi_{PM}. \quad (\text{A.E6})$$

The closed-loop voltage rise time is required to be less than 20ms, or within one electrical cycle. The time-domain simulation shows that  $G_{v,ol}^- \approx 15\text{Hz}$  satisfies this requirement. By defining  $\omega_i$  as the per-unitised current control loop bandwidth and  $\omega_v^-$  as the per-unitised  $\omega_{v,ol}^-$  on the base of  $\omega_1$ , and with two assumptions of  $R_g \approx 0$  and  $i_i \approx 0$ , (A.E5) is simplified to

$$G_{v,ol}^-(\omega) \approx (1 - \omega_v^-)X_g \frac{k_{pv} + jk_{iv}/\omega}{\vec{d}} \quad (\text{A.E7})$$

with

$$\vec{d} = \eta_i + j \frac{1}{\omega_i} \left[ \frac{\eta_v X_g}{\omega_1 L_f} (1 - \omega_v^-) - \omega_v^- \right]. \quad (\text{A.E8})$$

By defining the residual phase as  $\phi_r = \tan^{-1} \left( \frac{\omega k_{pv}}{k_{iv}} \right)$ ,

$$\phi_r \approx \frac{\omega k_{pv}}{k_{iv}} \text{ for } \frac{\omega k_{pv}}{k_{iv}} \rightarrow 0 \quad (\text{A.E9})$$

and the phase margin is then given by:

$$\phi_{PM} = \phi_r + \angle \vec{d}. \quad (\text{A.E10})$$

Note that  $\phi_r \in (10^\circ, 15^\circ)$  is resultant of the cooperation of the voltage PI controller gains and its open-loop bandwidth. Substituting for  $k_{iv}/\omega$  for  $k_{pv}/\phi_r$  from (A.E9) into (A.E7), the magnitude of  $G_{v,ol}^-$  is obtained as:

$$|G_{v,ol}^-(\omega)| = k_{pv} \left| 1 + \frac{j}{\phi_r} \right| \frac{(1 - \omega_v^-)X_g}{|\vec{d}|}. \quad (\text{A.E11})$$

Since  $\frac{1}{\phi_r} \gg 1$ ,

$$|G_{v,ol}^-(\omega)| \approx \frac{k_{pv}(1-\omega_v^-)X_g}{\phi_r |\vec{d}|}. \quad (\text{A.E12})$$

The crossover frequency, then, is determined from  $|G_{v,ol}^-(\omega)| = 1$ , leading to:

$$|\vec{d}| = (1 - \omega_v^-)X_g k_{pv} / \phi_r. \quad (\text{A.E13})$$

Substituting (A.E13) into (A.E9), the PI gains of  $C_v$  are given by:

$$k_{pv} = \frac{\phi_r k_{iv}}{\omega_{v,ol}^-}, \quad (\text{A.E14})$$

$$k_{iv} = \frac{\omega_{v,ol}^- |\vec{d}|}{(\omega_1 - \omega_{v,ol}^-)X_g}. \quad (\text{A.E15})$$

# Appendix F

## PSCAD Simulation File for Implementation of Tuning Guidelines

This appendix provides a comprehensive overview of the battery energy storage system simulation model, developed in PSCAD and referenced in [Section 2.4.6](#).

### Simulation Setup

To open the simulation file, the PSCAD case file named “**BESS\_PSCAD~~~\_###.psc**” should be loaded, where “~~~” indicates the PSCAD software version the file was created in and “###” represents the date of the latest update.

### General Description of The Model

The developed BESS simulation model incorporates a range of features designed to support flexible and scalable system implementation. The entire system is built using per-unit values, enabling straightforward adaptation to different system sizes and specifications.

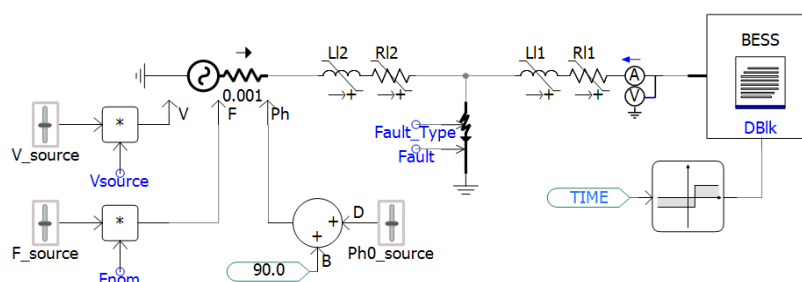
Operational control of the BESS is managed via an input signal that activates or deactivates the model. When activated, the system executes a smooth startup sequence, ensuring a stable transition into operation. The model supports three reactive power command modes: (i) automatic voltage regulation (AVR), (ii) direct reactive power (Q) reference, and (iii) direct power factor reference. For active power control in grid-forming operation, three strategies are available: droop-based control, VSG, and CGVSG.

In addition, three reactive power control methods are included: droop-based control, a rotor flux model, and a PI controller. These options provide flexibility to simulate and evaluate a wide range of control configurations.

The inner reticulation system of the BESS is implemented in a modular format, facilitating easy customisation and reuse across different simulation scenarios. The Unit Controller (UC) consists of multiple sub-blocks corresponding to distinct control levels and internal loops, which are designed for clarity, extensibility, and diagnostics. Furthermore, the model includes automatic tuning capabilities aligned with the guidelines presented in [Section 2.4.5](#). These features allow users to conveniently retune various control loops by specifying desired performance parameters.

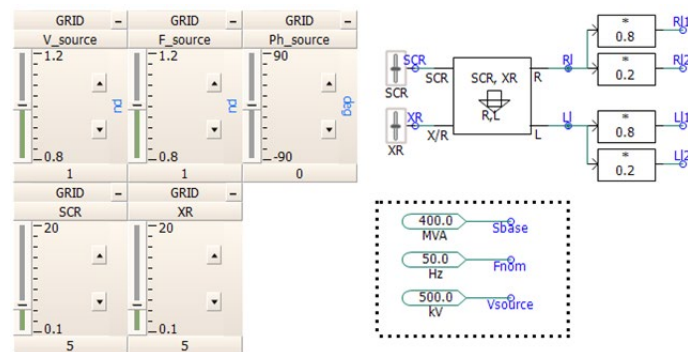
### Model at Its Highest Level

The model is a Grid-Forming Battery Energy Storage System connected to a three-phase voltage source through an RL impedance, illustrating a single-machine infinite bus system.



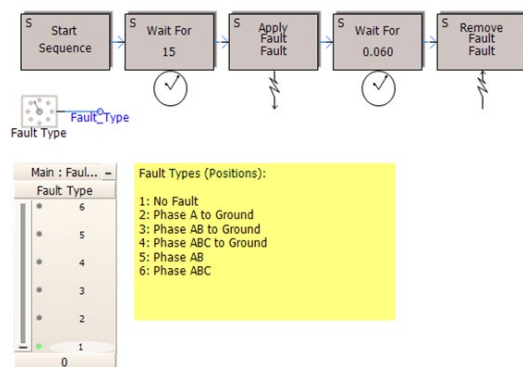
**Apx Figure F. 1: SMIB system featuring a BESS connected to the grid through an RL transmission line**

Definition “Grid RL Calc” is used at the highest level of the case to calculate the R and L values corresponding directly to the grid's SCR and X/R ratio.



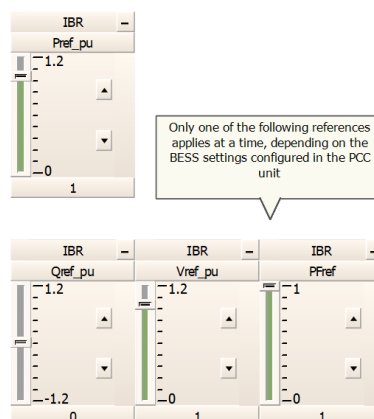
**Apx Figure F. 2:** The grid SCR and X/R ratio can be adjusted using the corresponding sliders. Additionally, the grid voltage, frequency, and phase angle can be modified in real time during the simulation using their respective sliders

Several faults and step changes are provided at the highest level, which can be activated based on the user's desires.



**Apx Figure F. 3:** Various faults can be applied using the corresponding slider, and the fault initiation and clearing times can also be set here

The P, Q, V, and PF references of the BESS can be easily set and adjusted using the provided sliders. Note that only one of Q, V, or PF can be selected as the reference at a time, as determined by the PPC implemented within the BESS control system.



**Apx Figure F. 4:** The user can set BESS commands using these sliders

The BESS parameters can be set through Right Click/Edit Parameters.

[GFM-BESS\_PSCAD502\_20250508:BESS] id='595316645'

References  
Configuration  
Grid Estimation

**General**

Active Power Reference (pu)	Pref_pu
Reactive Power Reference (pu)	Qref_pu
Voltage Reference (pu)	Vref_pu
Power Factor Reference	PFref

**Local Load**

Local Load Active Power (MW)	0.5
Local Load Reactive Power (MVar)	0.05

**General**

Ok Cancel Help...

(a)

[GFM-BESS\_PSCAD502\_20250508:BESS] id='595316645'

References  
Configuration  
Grid Estimation

**1-General**

Nominal System Frequency (Hz)	Fnom
MV/HV Transformer Rated Power (MVA)	Sbase
Grid Rated Voltage (kV)	Vsource
Reticulation Rated Voltage (kV)	33

**2-Units**

No. units	100
Rated Output Power of One Unit (MVA)	2
Units Rated Voltage (kV)	0.69
DC Link Nominal Voltage (kV)	1.2

**3-Filters**

GSC Inductance (pu)	0.1
GSC Resistance (pu)	0.002
GSC Capacitance (pu)	0.04
GSC Capacitor Resistance (pu)	0.01

**4-PWM**

GSC PWM Carrier Frequency (Hz)	5000
--------------------------------	------

**1-General**

Ok Cancel Help...

(b)

[GFM-BESS\_PSCAD502\_20250508:BESS] id='595316645'

References  
Configuration  
Grid Estimation

**General**

Maximum Grid SCR	10
------------------	----

**General**

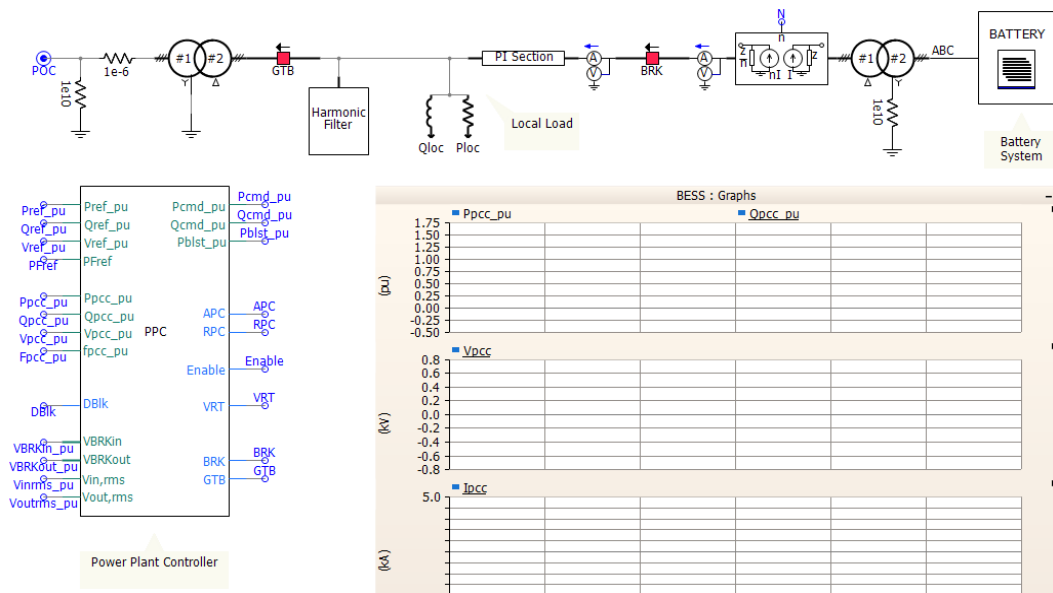
Ok Cancel Help...

(c)

Apx Figure F. 5: Dialogue boxes for BESS parameter settings

## Inside the BATTERY Model

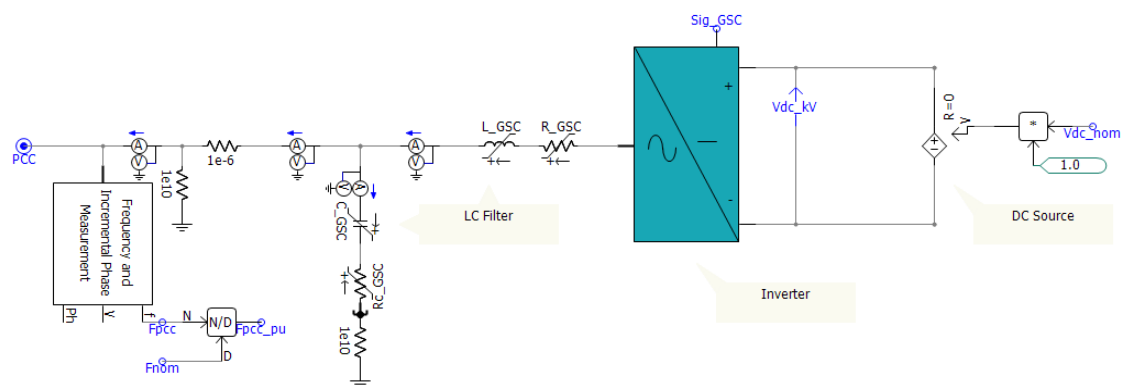
Double-clicking on the BESS block shows its internal circuit. The 'BATTERY' block includes the battery voltage source, the voltage source converter, and the electrical filters, while the 'PPC' block represents the power plant controller.



Apx Figure F. 6: Inside the BESS block

## Electrical Components

Apx Figure F. 7 illustrates the internal circuit of the BATTERY block.



Apx Figure F. 7: Internal circuit of the BATTERY block

## Control Systems

There are two distinct control systems in this model:

### PPC (Power Plant Controller):

The PPC, , shown in [Apx Figure F. 8](#), is responsible for providing the active and reactive power commands to the battery unit. Within this block, the user can choose from various reactive command methods:

- Incorporating an AVR to regulate the voltage at the point of connection
- Fixed Qref
- Fixed power factor reference

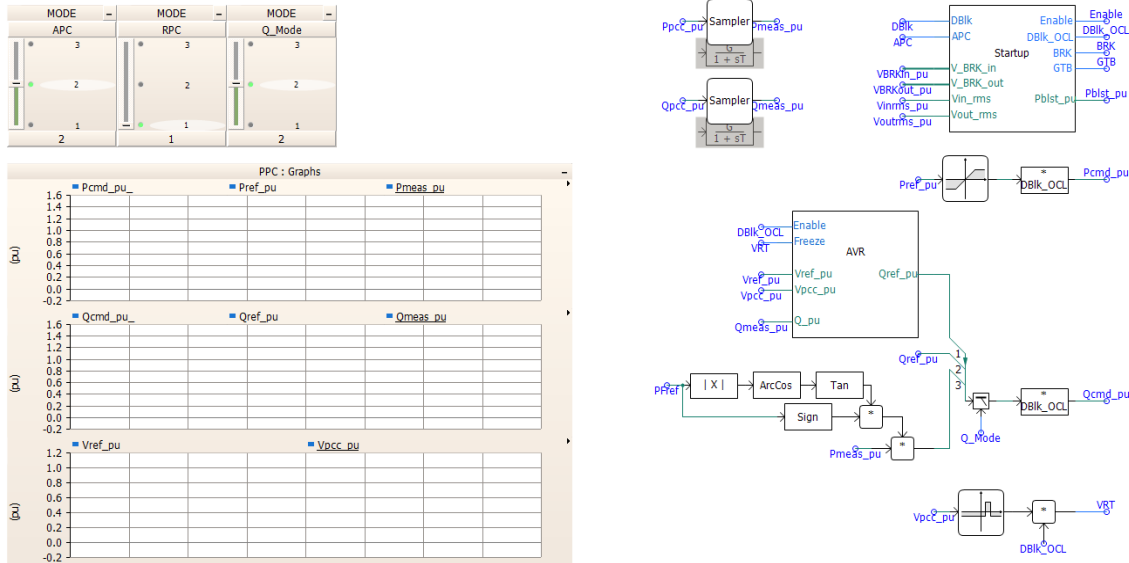
The user can also select from several APC methods:

- Droop-based
- VSG
- CGVSG

For RPC, the following methods are available:

- Droop-based
- Rotor flux model
- PI

Furthermore, the system's starting procedure is configured here by the 'Startup' block, along with the PPC delays and simple voltage-ride-through functions.

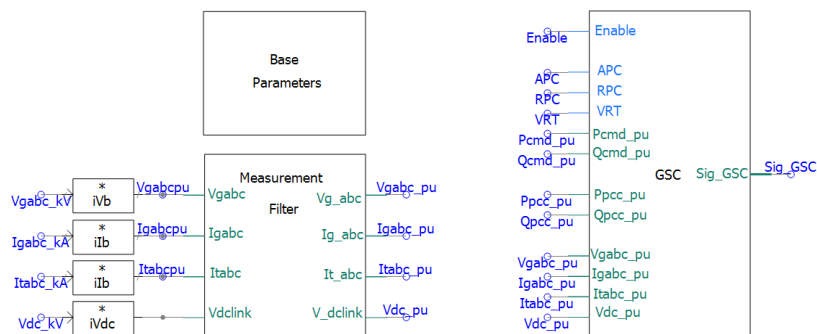


Apx Figure F. 8: Internal architecture of the Power Plant Controller

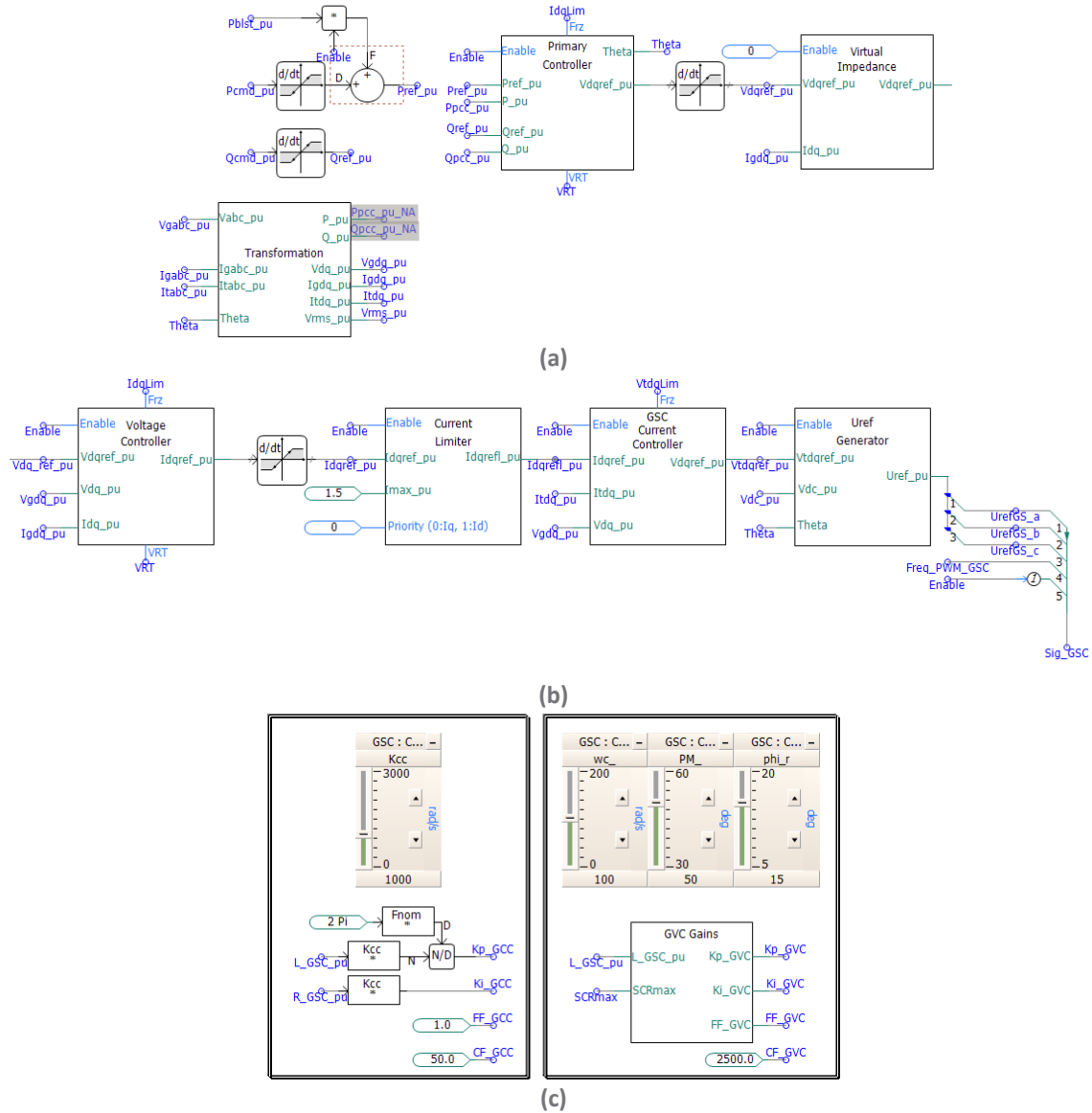
### Unit Controller (UC):

The UC, shown in [Apx Figure F. 9](#), is responsible for generating appropriate gating signals for the voltage source converter, considering the functionalities required by the battery system. The measured signals are first levelled and filtered (right-click on the Measurement Filter to set the filter bandwidth) before being fed into the GSC block, with its sub-block shown in [Apx Figure F. 10](#). Several blocks within the GSC block are used for different features required for the grid-forming operation mode.

The user can set the design values for the current controller and the voltage controller using the sliders shown in [Apx Figure F. 10\(c\)](#). To adjust the parameters of blocks like the Primary Controller and Virtual Impedance, the user can easily right-click on the block to set the desired values.



Apx Figure F. 9: Internal architecture of the Unit Controller



Apx Figure F. 10: Internal architecture of the GSC block



# Shortened Forms


AEMO	Australian Energy Market Operator
AI	Artificial Intelligence
AR-PST	Australian Research in Power Systems Renewable Transition
APC	Active Power Control
AVSG	Adaptive Virtual Synchronous Generator
BESS	Battery Energy Storage System
CC	Current Control
CCA	Critical Clearing Angle
CGVSG	Compensated Generalized Virtual Synchronous Generator
CCT	Critical Clearing Time
CLM	Current-Limiting Mode
d-PCL	Direct-Prioritised Current Limiter
DER	Distributed Energy Resource
DOA	Domain of Attraction
EMT	Electromagnetic Transient
EP	Equilibrium Point
GFL	Grid-Following
GFLI	Grid-Following Inverter
GFM	Grid-Forming
GFMI	Grid-Forming Inverter
IBR	Inverter Based Resource
NEM	National Electricity Market
NER	National Electricity Rules
NM	Normal Mode
NR	Newton-Raphson
PCC	Point of Common Coupling
PCL	Prioritised Current Limiter
PI	Proportional Integral
PLL	Phase-Locked Loop
POC	Point of Common Coupling

PPM	Parts Per Million
PSCAD	Power Systems Computer Aided Design
PWM	Pulse Width Modulation
q-PCL	Quadrature-Prioritised Current Limiter
REZ	Renewable Energy Zone
RPC	Reactive Power Control
SCR	Short Circuit Ratio
SEP	Stable Equilibrium Point
SG	Synchronous Generator
SMIB	Single Machine Infinite Bus
SVM	Space-Vector Modulation
THD	Total Harmonic Distortion
TNSP	Transmission Network Service Provider
TOH	Third-Order Harmonic
TS	Transient Stability
TSI	Transient Stability Index
UEP	Unstable Equilibrium Point
VC	Voltage Control
VSC	Voltage Source Converter
VSG	Virtual Synchronous Generator
WMZ	West Murray Zone

# References

1. H. Udawatte *et al.*, *Transient Stability Enhancement of IBR-dominated Grids in the Presence of Grid-forming Inverters*, CSIRO, Final Report, GPST Topic 1 – Inverter Design – Stage 3, Apr. 2024. [Online]. Available: <https://www.csiro.au/-/media/EF/Files/GPST-Roadmap/Stage3-Final/Topic-1Advanced-inverter-applications.pdf>.
2. F. Andrade *et al.*, “Study of large-signal stability of an inverter-based generator using a Lyapunov function,” in *Proceedings of the 2014 40th Annual Conference of the IEEE Industrial Electronics Society (IECON)*, 2014, pp. 1840–1846.
3. AEMO, “NEM generation maps,” Jan. 2024. [Online], Available: <https://aemo.com.au/en/energy-systems/electricity/national-electricity-market-nem/participate-in-the-market/network-connections/nem-generation-maps>.
4. AEMO, “NEM interactive map,” Jan. 2024. [Online], Available: <https://www.aemo.com.au/aemo/apps/visualisations/map.html>.
5. AEMO, “NEM generation maps,” Jan. 2025. [Online], Available: <https://aemo.com.au/en/energy-systems/electricity/national-electricity-market-nem/participate-in-the-market/network-connections/nem-generation-maps>.
6. S. P. Me *et al.*, “Transient stability of paralleled virtual synchronous generator and grid-following inverter,” *IEEE Transactions on Smart Grid*, vol. 14, no. 6, pp. 4451–4466, Nov. 2023.
7. J. Machowsk *et al.*, *Power System Dynamics: Stability and Control*, John Wiley & Sons, 2020.
8. P. Ge *et al.*, “Design-oriented analysis and transient stability enhancement control for a virtual synchronous generator,” *IEEE Transactions on Industrial Electronics*, vol. 70, no. 3, pp. 2675–2684, Mar. 2023.
9. D. Pan *et al.*, “Transient stability of voltage-source converters with grid-forming control: A design-oriented study,” *IEEE Journal of Emerging and Selected Topics in Power Electronics*, vol. 8, no. 2, pp. 1019–1033, Jun. 2020.
10. H. Hosseinpour *et al.*, “Large-signal stability analysis of inverter-based AC microgrids: A critical and analytical review,” *IEEE Access*, vol. 11, pp. 111466–111491, 2023.
11. R. Debnath, G. S. Gupta, and D. Kumar, “Lyapunov-Krasovskii passivity based stability analysis of grid-tied inverters,” *International Journal of Electrical Power & Energy Systems*, vol. 143, p. 108460, Dec. 2022.
12. H. Hosseinpour *et al.*, “Lyapunov-based large-signal stability analysis of inverter-based microgrids,” in *Proceedings of the 2022 North American Power Symposium (NAPS)*, 2022.
13. D. G. Schultz and U. J. Gibson, “The variable gradient method for generating Lyapunov functions,” *Transactions of the American Institute of Electrical Engineers, Part II: Applications and Industry*, vol. 81, no. 4, pp. 203–210, 1962.
14. P. Hart and B. Lesieutre, “Energy function for a grid-tied, droop-controlled inverter,” in *Proceedings of the 2014 North American Power Symposium (NAPS)*, 2014.
15. H. Xin *et al.*, “Synchronous instability mechanism of Pf droop-controlled voltage source converter caused by current saturation,” *IEEE Transactions on Power Systems*, vol. 31, no. 6, pp. 5206–5207, Nov. 2016.
16. Z. Shuai *et al.*, “Transient angle stability of virtual synchronous generators using Lyapunov’s direct method,” *IEEE Transactions on Smart Grid*, vol. 10, no. 4, pp. 4648–4661, Jul. 2019.
17. N. Hatziaargyriou *et al.*, “Definition and classification of power system stability—revisited & extended,” *IEEE Transactions on Power Systems*, vol. 36, no. 4, pp. 3271–3281, Dec. 2020.

18. Y.-H. Moon, B.-K. Choi, and T.-H. Roh, "Estimating the domain of attraction for power systems via a group of damping-reflected energy functions," *Automatica*, vol. 36, no. 3, pp. 419–425, Mar. 2000.
19. E. Muljadi, M. A. Pai, and T. B. Nguyen, "Transient stability of the grid with a wind power plant," in *Proceedings of the 2009 IEEE/PES Power Systems Conference and Exposition (PSCE)*, 2009.
20. M. A. Chowdhury *et al.*, "Comparative study on fault responses of synchronous generators and wind turbine generators using transient stability index based on transient energy function," *International Journal of Electrical Power & Energy Systems*, vol. 51, pp. 145–152, Oct. 2013.
21. D. B. Rathnayake, R. Razzaghi, and B. Bahrani, "Generalized virtual synchronous generator control design for renewable power systems," *IEEE Transactions on Sustainable Energy*, vol. 13, no. 2, pp. 1021–1036, Apr. 2022.
22. H. Wijayalath, N. Mohammed, and B. Bahrani, "Comparative analysis of grid-forming inverters: Influence of control parameters and grid conditions on transient stability," in *Proceedings of the 2024 IEEE Energy Conversion Congress and Exposition (ECCE)*, 2024.
23. D. B. Rathnayake *et al.*, "Grid forming inverter modeling, control, and applications," *IEEE Access*, vol. 9, pp. 114781–114807, 2021.
24. S. Y. Caliskan and P. Tabuada, "Towards Kron reduction of generalized electrical networks," *Automatica*, vol. 50, no. 10, pp. 2586–2590, Oct. 2014.



**As Australia's national science agency and innovation catalyst, CSIRO is solving the greatest challenges through innovative science and technology.**

CSIRO. Unlocking a better future for everyone.

**Contact us**

1300 363 400  
+61 3 9545 2176  
[csiro.au/contact](https://csiro.au/contact)  
[csiro.au](https://csiro.au)